


7-2015

A Computational Study of the Potential for LNG Tanker Polystyrene Foam Insulation Failure under Fire Exposure

Jeffrey David Martinez
University of Arkansas, Fayetteville

Follow this and additional works at: <http://scholarworks.uark.edu/etd>

 Part of the [Complex Fluids Commons](#), and the [Transport Phenomena Commons](#)

Recommended Citation

Martinez, Jeffrey David, "A Computational Study of the Potential for LNG Tanker Polystyrene Foam Insulation Failure under Fire Exposure" (2015). *Theses and Dissertations*. 1224.
<http://scholarworks.uark.edu/etd/1224>

This Dissertation is brought to you for free and open access by ScholarWorks@UARK. It has been accepted for inclusion in Theses and Dissertations by an authorized administrator of ScholarWorks@UARK. For more information, please contact scholar@uark.edu, ccmiddle@uark.edu.

A Computational Study of the Potential for LNG Tanker
Polystyrene Foam Insulation Failure under Fire Exposure

A Computational Study of the Potential for LNG Tanker
Polystyrene Foam Insulation Failure under Fire Exposure

A dissertation submitted in partial fulfillment
of the requirements for the degree of
Doctor of Philosophy in Chemical Engineering

By

Jeffrey Martinez
University of Arkansas
Bachelor of Science in Chemical Engineering, 2010

July 2015
University of Arkansas

This dissertation is approved for recommendation to the Graduate Council.

Dr. Jerry A. Havens
Dissertation Director

Dr. Mark E. Arnold
Committee Member

Dr. Greg Thoma
Committee Member

Abstract

Liquefied natural gas is shipped across the oceans in large marine carriers. The carriers house the LNG using several different insulation systems. One of these systems involves large aluminum spheres insulated with polystyrene foam. Polystyrene foam is very susceptible to heat degradation. This raised issues as to the extent of possible insulation failure caused by a large ship fire. Experiments were done investigating the nature of polystyrene's thermal degradation, notably by Brauman, Chen, and Matzinger and Butler. A large scale investigation was also performed by Sandia National Laboratory. However, computational modeling of the degradation was lacking. This work set out to build comprehensive models of the experiments performed by BCM, Butler, and Sandia. The models were created using COMSOL Multiphysics, a complex finite element method computational software. The thermal degradation of polystyrene is a complex process involving moving boundaries, phase transitions, and temperature dependent physical properties. The BCM and Butler experiments provided the most amount of detail and were used to test the accuracy of the models and methods used within them. The value of principal interest was the overall regression rate of the material, a variable that could be calculated by the models and compared directly with experimentally measured values. Modeling started with an extensive literature review of the physical properties of dense and foam polystyrene. The BCM experiments were first considered as they were the least complex. Both a transient and a steady-state model of the BCM experiments were built. Although detail of the transient heat up phase was lost, the steady-state model provided a better fit with experiment. With a good fit of the BCM experiments, the techniques were carried forward and adapted to the more complex Butler foam polystyrene experiments. Again, regression rates for the model were reasonably close to those measured by experiment. Next, the Sandia experiment was investigated. Here, the values of interest were no longer regression rates but insulation failure times and cargo tank heat fluxes. The Sandia experiment presented a new complication in the form of necessary information not being available, notably the surface emissivity of the aluminum scrim used. With the model, it was found that a very low surface emissivity, one near the lowest commercially available, was required to match the experimental results.

Table of Contents

Abstract	
Table of Contents	
List of Figures	
List of Variables	
Introduction	1
Literature Review	5
BCM Polystyrene Degradation Study	6
Butler Polystyrene Degradation Study	10
Sandia Large Scale LNG Testing	13
Computational Fluid Dynamics	17
Finite Element Method	17
Arbitrary Lagrangian-Eulerian Methods (ALE)	24
Material Properties	31
Computer Modeling	41
COMSOL Transient Model of BCM Experiments	43
COMSOL Steady State Model of BCM Experiments	48
COMSOL Model of Butler Foam Experiments	50
COMSOL Model of Sandia Experiment	54
Results and Discussion	58
BCM Models	58
Butler Model	63
Sandia Model	68
Conclusions	87
Bibliography	88

List of Figures

Figure 1: Cross Section of Moss Sphere	3
Figure 2: Effects of Temperature on Bead Structure	5
Figure 3: Schematic Diagram of Polymer Rod with Light Shield	6
Figure 4: Steady-State System Illustration	8
Figure 5: Regression Results for BCM and Butler Solid Samples	10
Figure 6: Butler Experimental Apparatus	11
Figure 7: Regression Results for Butler Foam Samples	12
Figure 8: Sandia Laboratories Large Scale LNG Fire Tests	13
Figure 9: Sandia Laboratories LNG Insulation System Apparatus	14
Figure 10: Sandia Laboratories Moss Sphere PS Insulation System	15
Figure 11: Global-Local Correspondence of Nodes for Assembly	21
Figure 12: One-Dimensional Example of Lagrangian, Eulerian, and ALE Mesh and Particle Motion	25
Figure 13: Relation Between ALE Three Frames of Reference	26
Figure 14: NETZSCH Heat Capacity Data	32
Figure 15: NETZSCH Foam Polystyrene DSC Data	34
Figure 16: NETZSCH Solid Polystyrene DSC Data	35
Figure 17: Approximate DSC Curve	36
Figure 18: NETZSCH Solid Polystyrene TGA and DTGA Data	37
Figure 19: Temperature Dependent H	38
Figure 20: NETZSCH Foam Polystyrene TGA and DTGA Data	39
Figure 21: Transient BCM Model Diagram	44
Figure 22: Dense Polystyrene Mass Percent Loss (<i>mpl</i>)	47
Figure 23: Steady-State BCM Model Diagram	48
Figure 24: Butler Model Diagram	50
Figure 25: Sandia Model Diagram	54
Figure 26: BCM Models Example Temperature Profiles	58
Figure 27: Transient vs Steady-State BCM Models Comparison	59

Figure 28: Transient BCM Model vs BCM Data Over Full Flux Range	60
Figure 29: Transient BCM Model Results	61
Figure 30: Butler Model Example Temperature Profiles	63
Figure 31: Butler Model Example Regression	64
Figure 32: Butler Model Example Regression Rate	65
Figure 33: Butler Model Results	66
Figure 34: Sandia Model Step One Temperature Profile	69
Figure 35: Sandia Model Step Two Temperature Profiles	70
Figure 36: Sandia Model Step Three Temperature Profiles	71
Figure 37: Sandia Model Regression Rate	72
Figure 38: Sandia Model Boundary Movement	73
Figure 39: Sandia Model Step 4 Temperature Profiles with Heat Lamps Off	75
Figure 40: Sandia Model Step 4 LN2 Tank Heat Flux with Heat Lamps Off	76
Figure 41: Sandia Model Step 4 Temperature Profiles with Heat Lamps On	77
Figure 42: Sandia Model Step 4 LN2 Tank Heat Flux with Heat Lamps On	78
Figure 43: Sandia Model Step 4 LN2 Tank Heat Flux with Heat Lamps On and Foil Emissivity of 0.8	79
Figure 44: Sandia Model Step 4 Temperature Profiles with Heat Lamps On and Foil Emissivity of 0.8	80
Figure 45: Sandia Model Step 4 LN2 Tank Heat Flux with Heat Lamps On and Film Boiling	81
Figure 46: Sandia Model Step 4 LN2 Wall Temperature with Heat Lamps On and Film Boiling	82
Figure 47: Sandia Model Step 4 LN2 Tank Heat Flux with Heat Lamps Off and Film Boiling	83
Figure 48: Sandia Model Step 4 LN2 Wall Temperature with Heat Lamps Off and Film Boiling	84

List of Variables

\hat{H} : enthalpy of stream k, J/g

\hat{H}_{in} : enthalpy of flow into a system or boundary, J/g

\hat{H}_{out} : enthalpy of flow out of a system or boundary, J/g

H_{rvum} : heat required to vaporize a unit mass, J/g

\dot{m}_{in} : mass flow into a system or boundary, kg/m²s

\dot{m}_k : mass flux of stream k, kg/m²s

\dot{m}_{out} : mass flow out of a system or boundary, kg/m²s

mpl : mass loss percent

\dot{q} : heat flux, W/m²

\dot{q}_{cond} : conductive heat flux, W/m²

\dot{q}_{conv} : convective heat flux, W/m²

\dot{q}_{in} : heat flux into a system or boundary, W/m²

\dot{q}_{lamp} : radiation heat flux from lamp, W/m²

\dot{q}_{out} : heat flux out of a system or boundary, W/m²

\dot{q}_{rad} : radiation heat flux, W/m²

T_{amb} : ambient temperature, K

T_{lamp} : lamp temperature, K

T_{melt} : polystyrene melting temperature, K

T_{source} : temperature of radiation source, K

$T_{surface}$: surface temperature, K

T_{vap} : maximum vaporization temperature, K

v : velocity, m/s

v_{liquid} : velocity of liquid material, m/s

v_{ram} : ram velocity, m/s

$v_{regression}$: regression velocity, m/s

\dot{w} : work flux of the system, W/m²

Ψ : potential energy of stream k, J/g

ε : emissivity

σ : Stefan-Boltzmann constant, $5.67 \cdot 10^{-8} \text{ W/m}^2/\text{K}^4$

ρ_{liquid} : density of the liquid or solid polystyrene, kg/m^3

ρ_{foam} : density of the foam polystyrene, kg/m^3

Introduction

Society of International Gas Tanker and Terminal Operators Ltd. (SIGTTO) Working Group

In 2004, SIGTTO was approached by Professor Jerry Havens with concerns about the sizing of the pressure relief valves on liquefied natural gas (LNG) shipping vessels with non-fire-resistant cargo insulation. The increased boil off due to a partial or complete loss of the insulation is not taken into account in the current regulations for the sizing of pressure relief valves (IMO IGC Code 8.5). As the polystyrene used in Moss sphere type LNG containers could be exposed to damaging heat fluxes in the event of a fire on deck or near the ship, concerns were raised pertaining to its effectiveness under extreme heating conditions. In response, SIGTTO organized a working group consisting of industry partners and shipping classification societies to consider possible oversights in the regulations. The working group was specifically tasked with determining the response of LNG vessel insulation systems to enveloping pool fires following spillage of LNG. The working group made two recommendations, among others, the following:

1. "If large scale LNG fire tests are carried out by Sandia, or others, that show significant conflict with existing values of heat flux used in the IGC Code and other industry codes and standards, the question of the current equations for determining fire-case pressure relief loads merit re-examination by the whole LNG industry and not just the shipping element."
2. "Although the working group has determined that the current polystyrene foam insulated Moss sphere LNG carriers are equipped with pressure relief valves that provide additional capacity to prevent failure by over-pressure of intact cargo tanks, a better understanding of the foam plastic insulation vulnerability to heating is required to adequately assess the hazards that could result from loss of insulation effectiveness with fire exposure. Given the comparatively short duration of LNG fires as estimated by previous fire scenario studies, a much better understanding of the temporal response of the foam plastic insulation materials is necessary to determine the worst case circumstances as referred to in the conclusions above. Further research, which should include physical insulation testing as well as a determination of the potential for

additional damage due to combustion of the foam degradation products, is recommended.” [1]

While a consensus was reached on most of the topics investigated, significant concerns remained about the response of the polymeric foam to fire conditions. Some members of the working group were dissatisfied with the mathematical predictions and conclusions reached, and Professors Jerry Havens and James Venart of the working group published a paper prior to the completion of the SIGTTO report where they independently outlined their own conclusions [2]. Contrary to the SIGTTO report findings, Havens and Venart predicted total foam insulation failure in as few as 10 minutes and LNG boil off rates an order of magnitude higher than provided by current pressure relief valve requirements.

Liquefied Natural Gas

LNG is the condensed form of natural gas that has been cooled at atmospheric pressure to approximately -161°C . It is made up primarily of methane with small amounts of ethane, propane, butane, nitrogen, and sometimes trace amounts of other light end hydrocarbons. In its liquid form, it has a density that is approximately 45% that of water and as a result pools on top of water when spilled. Natural gas at low concentrations in air is colorless, odorless, non-toxic, and non-carcinogenic. Its main component, methane, has a positive buoyancy under normal atmospheric conditions. Methane has flammability limits between about 4 and 16 percent in air [3].

Moss Spheres

Currently there are more than 300 LNG carriers in service utilizing two major types of cargo containment systems: Moss spheres and membrane systems. The Moss sphere design makes up almost half of the current fleet.

A typical Moss sphere vessel consists of four to six aluminum alloy spheres with a capacity of $125,000\text{ m}^3$, though vessels with capacities as low as $20,000\text{ m}^3$ and as large as $150,000\text{ m}^3$ are in service. The aluminum spheres are mounted to the vessel by an equatorial skirt of steel. The spheres, which protrude above deck, are protected from heat gain by a layer

of insulation with a thin foil covering on its exterior, an air or inert gas gap, and an outer steel weather cover (Figure 1).

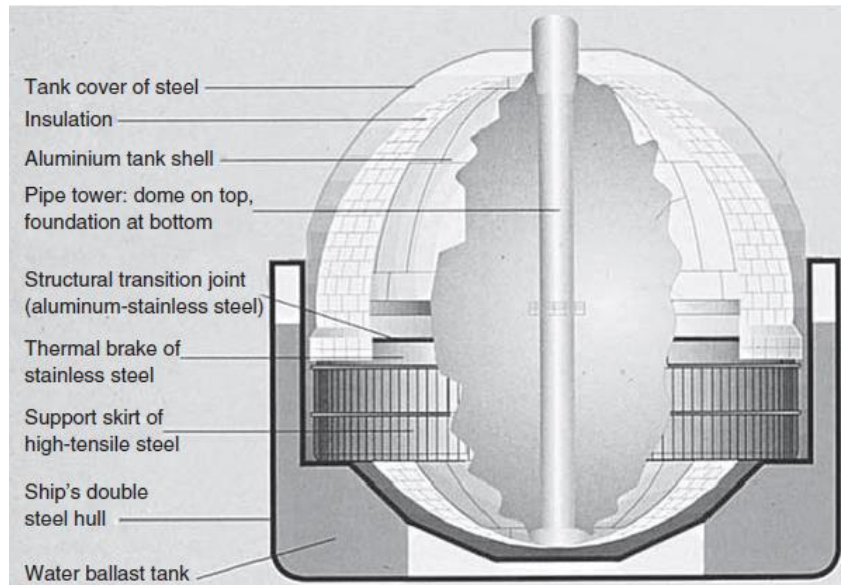


Figure 1: Cross Section of a Moss Sphere (Gaztransport & Technigaz)

The insulation layer on a Moss sphere is made of polymeric foam; in general polyurethane, polystyrene or phenol resins are used. While these foams provide excellent thermal resistivity, they degrade at relatively low temperatures. This dissertation focuses on polystyrene (PS) foam insulation.

Polystyrene Insulation

Polystyrene is non-polar, chemically inert, non-reactive with water, and solid below its glass transition point of approximately 100 °C. Polystyrene has many uses from coffee cups and commercial insulation to lost foam metal casting.

There are two categories of foam PS: expanded polystyrene (EPS) and extruded polystyrene (XPS). XPS is formed by combining polystyrene granules with chemical additives in an extruder. The PS is then injected with a blowing agent after which the molding process creates the finished XPS product. Examples of this process include the blue and pink insulation products commonly used for building insulation. In the production of EPS, PS is polymerized in suspension along with blowing agents forming small beads. The beads are then expanded into a

mold [4]. This creates the “glued beads” look that is often seen in items such as packaging and coffee cups.

In an attempt to address the second recommendation of the SIGTTO work group, James Butler did a series of polystyrene heat flux regression experiments as part of his MS degree [5]. He measured the regression of both solid polystyrene and XPS as a function of applied heat flux and concluded that the difference in regression rates was relatively proportional to the difference in densities. His results were in general agreement with the predicted failure times of Havens and Venart. This dissertation study further addressed the second SIGTTO recommendation by providing a computational (CFD) model comparison of the experimental data on the decomposition rates of XPS as a function of applied heat flux. As explained subsequently, the CFD modeling will utilize the COMSOL Multiphysics platform.

Literature Review

Current IGC code assumes an emissive heat flux from the fire of 108 kW/m^2 to determine pressure valve sizing. However, research on LNG pool fires indicates that the flux from a LNG pool fire may reach 350 kW/m^2 . This led the SIGTTO working group to model the response of the LNG containment system for conditions ranging from the IGC standard to 300 kW/m^2 and to consider the times to failure [1].

A qualitative understanding of the foam degradation process is gained by studying the stages of thermal degradation undergone by PS foam beads. Expanded polystyrene (EPS) beads thermally decompose through three major stages: bead collapse, melting, and vaporization. The effects of temperature on the bead formation and overall polymer condition were observed by dipping 1.5 cm^3 samples of EPS into water and wax (Figure 2).

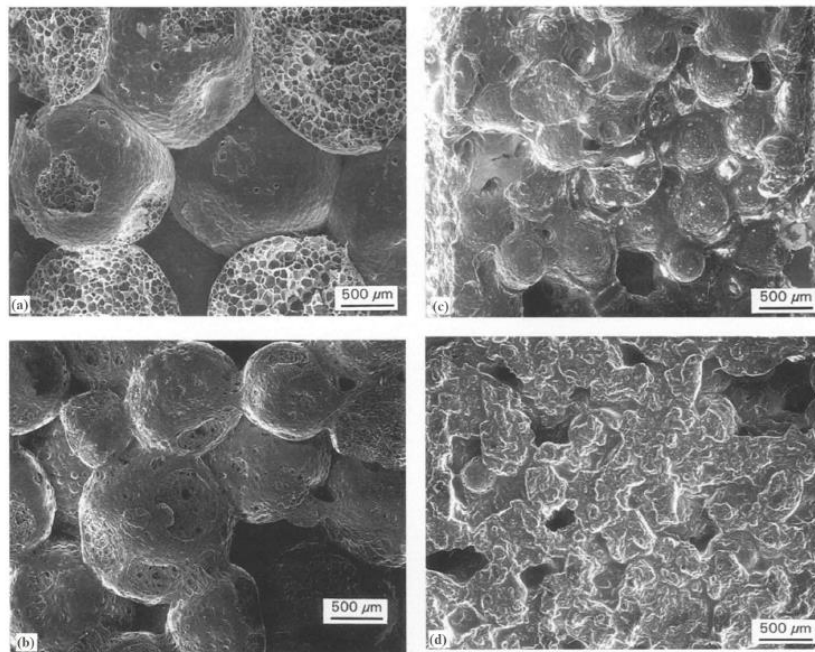


Figure 2: Effects of Temperature on Bead Structure
(EPS initial density = 0.024 g/cm^3) (a) $80 \text{ }^\circ\text{C}$, (b) $110 \text{ }^\circ\text{C}$, (c) $120 \text{ }^\circ\text{C}$, (d) $160 \text{ }^\circ\text{C}$

At $160 \text{ }^\circ\text{C}$ the beads have completely melted forming a viscous residue [6]. As the temperature increases past $170 \text{ }^\circ\text{C}$ the viscosity decreases until the vaporization point is reached. The differential scanning calorimetry and thermal gravimetric analysis from Mehta et al [6]

indicated that vaporization begins around 275 °C and most all of the sample is vaporized by 460 °C.

BCM Polystyrene Degradation Study

The work of Brauman, Chen, and Matzinger (BCM) gives a useful quantitative understanding of polystyrene thermal degradation by determining its combustion characteristics and pyrolysis rates [7]. BCM created a “novel rod driven apparatus” to measure the combustion rates of polystyrene. A quartz sleeve mounted in a 15 cm diameter chimney was used to house 6 and 10 cm lengths of 1.2 cm diameter Dow Styron 666U polystyrene rods. Carbon black was added at 0.05% by weight to prevent incident radiation from being absorbed in the polymer bulk. The rods were ignited from the top and as the surface burned away the rods were advanced by syringe pump. The drive rate of the syringe pump was adjusted to match the burning rate so that the surface of the molten polystyrene stayed level with the top of the quartz sleeve. This velocity of advance divided by the surface area gave the mass loss rate per surface area during combustion. The same procedure was then carried out using infrared lamps as the heat source instead of combustion. A water cooled shield was added around the quartz sleeve to prevent the sample from heating at the sides (Figure 3).

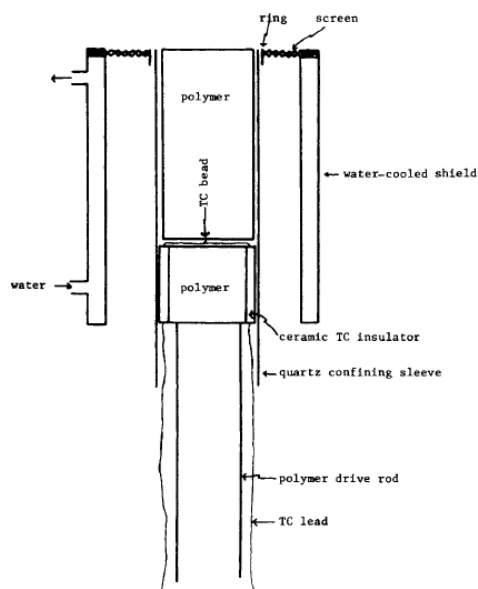


Figure 3: Schematic Diagram of Polymer Rod with Light Shield

The samples were replaced by a radiometer to independently measure the flux emitted by the spot heaters. A heating rate of 56.5 kW/m^2 was found to match the burning rate of 0.059 cm/min [7].

Along with measuring regression rates, BCM conducted extensive temperature measurements with thermocouples placed in the rods. The thermocouple junction was placed horizontally across the rod radius while the thermocouple leads were then run vertically through insulated grooves out of the bottom of the rod. This allowed time dependent temperature data to be collected at specific radii. When combined with the recorded regression rates, BCM was able to create depth dependent temperature plots at specific radii. These plots showed that after an initial heat up phase, the temperature as a function of depth becomes independent of time. The temperature data also indicated that a maximum surface temperature of 719 K was achieved.

After the initial heating up phase of the experiment, BCM found that the temperature profiles and regression rates became independent of time. This lead BCM to a steady-state analysis of the system; a technique previously used by Tewarson in his combustion/pyrolysis analysis of polymeric materials [8]. As illustrated in Figure 4, the system can be considered a steady-state, open flow system with axial symmetry. The system has a constant mass flow rate from bottom to top, with a constant heat flow in at the top and a constant heat flow out of the side.

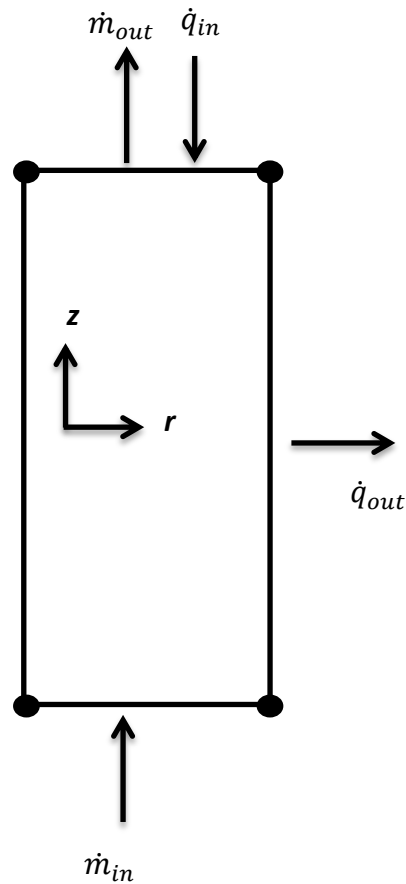


Figure 4: Steady-State System Illustration

If the energy balance for a steady-state open system is considered:

$$0 = \sum_{k=1}^i \dot{m}_k \left(\hat{H} + \frac{v^2}{2} + \Psi \right)_k + \dot{q} + \dot{w}$$

\dot{m}_k : mass flux of stream k, kg/m² s

\hat{H} : enthalpy of stream k, J/g

v : velocity of stream k, m/s

Ψ : potential energy of stream k, J/g

\dot{q} : heat flux absorbed by the system, W/m²

\dot{w} : work flux of the system, W/m²

The change in kinetic and potential energy terms can be considered negligible. The work term can also be neglected. The system has no mass accumulation, so the mass flow in must be equal to the mass flow out,

$$\dot{m}_{in} = \dot{m}_{out} = \dot{m}$$

and the energy balance reduces to:

$$0 = \dot{m}(\hat{H}_{out} - \hat{H}_{in}) + (\dot{q}_{out} - \dot{q}_{in})$$

The system is defined as only solid and liquid phase, where the liquid is heated up to the point of vaporization. This sets the change in enthalpy to the sum of the energy required to heat the incoming material from inflow or ambient temperature to outflow or final temperature and the energy required to vaporize the material. Calling this change in enthalpy term H_{rvum} , and rearranging the reduced energy balance, the following equation results:

$$\dot{m} = (\dot{q}_{in} - \dot{q}_{out})/H_{rvum}$$

H_{rvum} : heat required to vaporize a unit mass, J/g

The mass loss rate can then be related to ram velocity, v_{ram} , through a simple mass balance:

$$\dot{m} = \rho_{in} * v_{ram}$$

BCM then assumed a constant value of \dot{q}_{out} , and plotted \dot{m} versus \dot{q}_{in} , with a straight line yielding an intercept of \dot{q}_{out}/H_{rvum} and a slope of $1/H_{rvum}$ [8]. Using this method BCM calculated the total heat required to vaporize a unit mass of PS to be 1980 J/g and the heat loss to the surrounding for their apparatus to be 41.6 kW/m². Figure 5 shows BCM's plotted data.

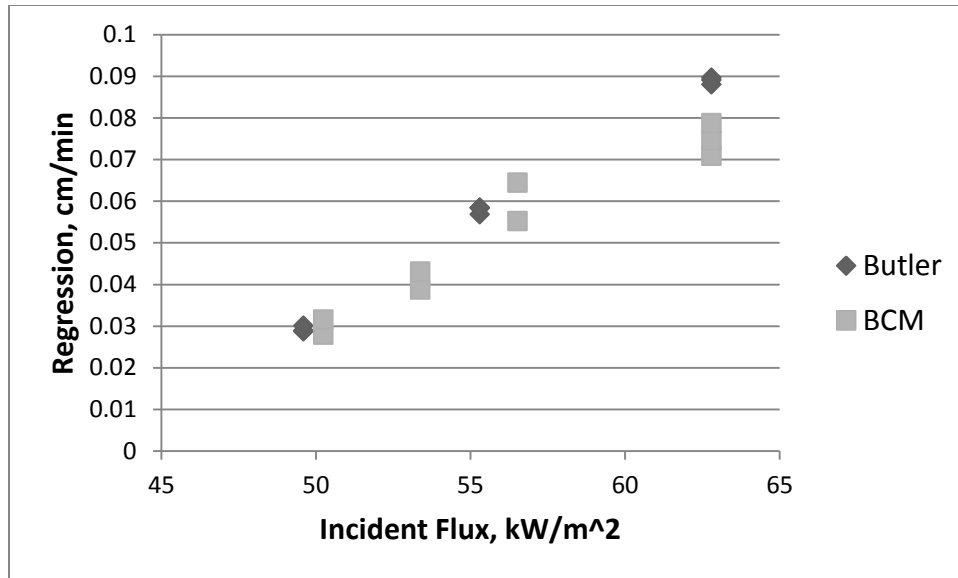


Figure 5: Regression Results for BCM and Butler Solid Samples

Butler Polystyrene Degradation Study

In his master's thesis work, James Butler set out to recreate the radiant heat flux experiments of BCM as closely as possible before extending the experiments to polystyrene foam [5]. Butler managed to assemble equivalent pieces of equipment used in the BCM's experiments. However, three changes were made from the original work. Butler did not plan to recreate the combustion experiments and therefore did not need the chimney and separate cooling jacket used by BCM. This reduced the overall size of Butler's apparatus and required lowering of the nitrogen purge to maintain laminar flow. Lastly, the original polystyrene material used by BCM could not be obtained. A very similar material, Dow Styron 666d, was used with the same 0.05 weight percent carbon black added. His samples were milled to 1.08 cm in diameter and 10 cm in length.

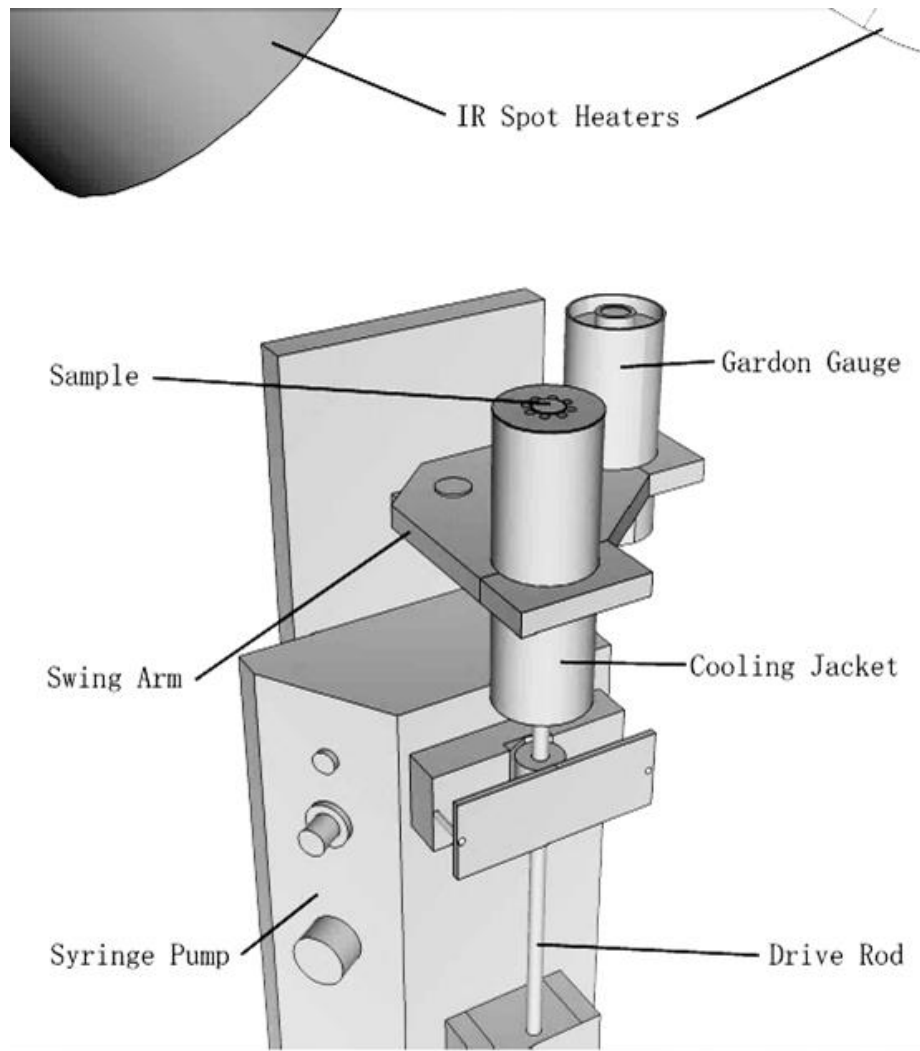


Figure 6: Butler Experimental Apparatus

Figure 6 illustrates Butler's apparatus. It used two Research Inc. Model 4085 halogen spot heaters as the radiant source. These were mounted 40 degrees off of vertical and focused onto the top sample surface. A Research Inc. Model 5420 SCR powerstat was used to regulate the incident heating flux. This powerstat did not allow for direct calibration of the heating lamps due to the coarseness of its controls. Instead, before each run the heat flux was measured using a Medtherm Model 64-15-20 Gardon gauge. This was done by mounting the Gardon gauge and the sample housing on a swing arm so the two could easily be switched into position beneath the lamp heaters.

He then repeated BCM's solid polystyrene pyrolysis experiments for three different incident fluxes over a range of 49.6 to 62.8 kW/m² (Figure 5). Using the same steady-state analysis described above, Butler calculated an H_{rvum} of 1731 J/g and a \dot{q}_{out} of 42.8 kW/m². He also reported a 0.058 cm/min regression rate at 55.3 kW/m² incident flux.

Butler decided his method and equipment produced sufficiently close results to BCM to proceed with extending the experiment to foam polystyrene material. The foam samples were cut with a hotwire apparatus from Dow Styrofoam board panels to a diameter of 1.12 cm. Due to the much more rapid regression of the foam samples, the experiments were run over a lower external heat flux range and with longer sample rods. 15 cm long samples were run at five incident flux values over a range of 27.4 to 45.1 kW/m² (Figure 7). Following the previously prescribed analysis, an H_{rvum} of 1592 J/g and a \dot{q}_{out} of 17.6 kW/m² were calculated for the foam material.

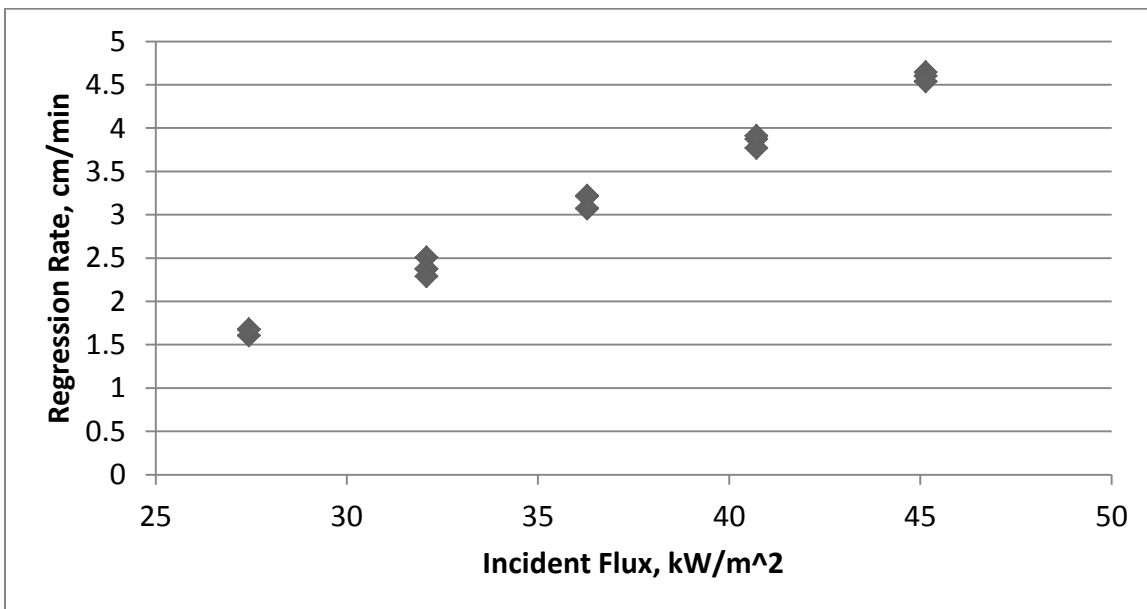


Figure 7: Regression Results for Butler Foam Samples

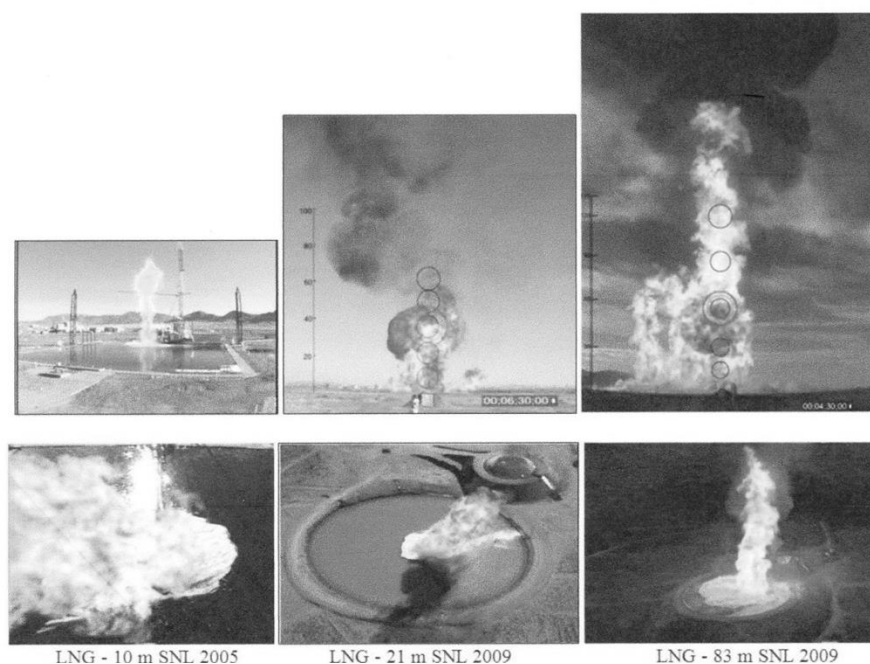
Unlike in the dense material, there is a large change in density between the foam and liquid phases. This difference causes a collapsing action which contributes importantly to the regression rate along with vaporization. A liquid layer of ever growing thickness develops due to the vaporization and collapsing occurring at different rates. This constantly growing liquid layer

brings into question the steady state assumption. Butler was unable to get any temperature measurements for the foam material, leaving the steady-state assumption to be judged solely on the regression rates. Butler found the regression rate to become time independent at all measured incident fluxes, providing some confidence in the steady-state assumption.

Sandia Large Scale LNG Testing

In an attempt to address the two recommendations of the SIGTTO working group, Sandia National Laboratories conducted a series of large scale LNG experiments [18]. Their experiments consisted of two phases. The first phase tested large scale LNG pool fires for emissive power, duration, and other fire conditions. The second phase tested the heat response of different insulation systems with heat boundary conditions determined by the results of phase one.

Phase one consisted of two experiments involving LNG pool fires on water. One was a pool fire of 21 m in diameter and the other was 87 m. Test one discharged 15340 gal of liquid methane onto water over 510 seconds at flow rates varying from 970 to 1960 gpm. Test two discharged 52500 gal over 144 seconds at an average flow rate of 30300 gpm (Figure 8).



LNG - 10 m SNL 2005 LNG - 21 m SNL 2009 LNG - 83 m SNL 2009

Figure 8: Sandia Laboratories Large Scale LNG Fire Tests

Analysis of the two experiments showed an average surface emissive power for the 21 m fire of around 277 kW/m^2 and 286 kW/m^2 for the 83 m fire. In both experiments it was found that the fire base area was smaller than the LNG pool area. This is contrary to the assumption used in all previous analysis that the pool and fire areas are equal. It was hypothesized that a surface emissive power of 286 kW/m^2 would be expected of a fire in the 100 m diameter range, and that it would be reasonable value to use in hazard calculations.

Phase two consisted of testing the heat exposure responses of four different LNG tanker insulation systems. The following description will be only for the test of the extruded polystyrene panel insulation system. The experimental set up used a one meter by one meter rectangular enclosure insulated on four sides by three inches of Pyrotherm I-series boards. At one end of the enclosure a steel plate 16 mm in thickness was attached to simulate the weather cover. Heating lamps simulated the fire by providing 270 kW/m^2 heat flux onto the outside surface of the steel plate. This heat flux was measured by a Medtherm Model 64-30sb-18K/sw-1c-120 radiometer. A tank of liquid nitrogen was placed at the other end of the enclosure to simulate the LNG tank. Attached to the outside surface of the LN2 tank was a RdF Model 27036-1 micro-foil heat flux sensor. Figure 9 illustrates the enclosure. The left panel is a photo of the heating lamp array. The middle panel is the outside of the enclosure. The steel weather cover is on the left end of the enclosure and the LN2 tank is on the right end. The right panel is a cross-section of the enclosure with the heating array in place.

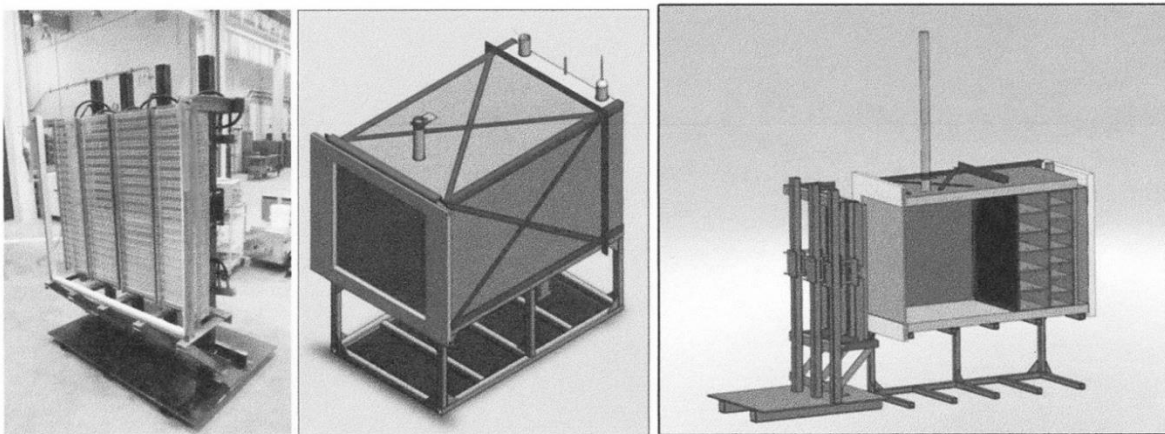


Figure 9: Sandia Laboratories LNG Insulation System Apparatus

The LN2 tank had a wall thickness of 38 mm. Liquid nitrogen has a temperature of 77 K versus the 113 K temperature of LNG. Placed inside the enclosure against the liquid nitrogen tank is the insulation system. The polystyrene insulation system was provided to Sandia by Moss Maritime AS and arrived directly from the manufacturer. It was composed of three layers of extruded polystyrene separated by thin layers of glass-fiber mesh with a total thickness of 300 mm. Glued to the end of the foam assembly facing the weather cover is a thin, highly emissive aluminum sheet. Both the exact emissivity and thickness of this sheet were unspecified. Thermocouples were placed throughout the polystyrene foam, on the aluminum scrim, on the backside of the weather cover, and on the outside of the LN2 tank.

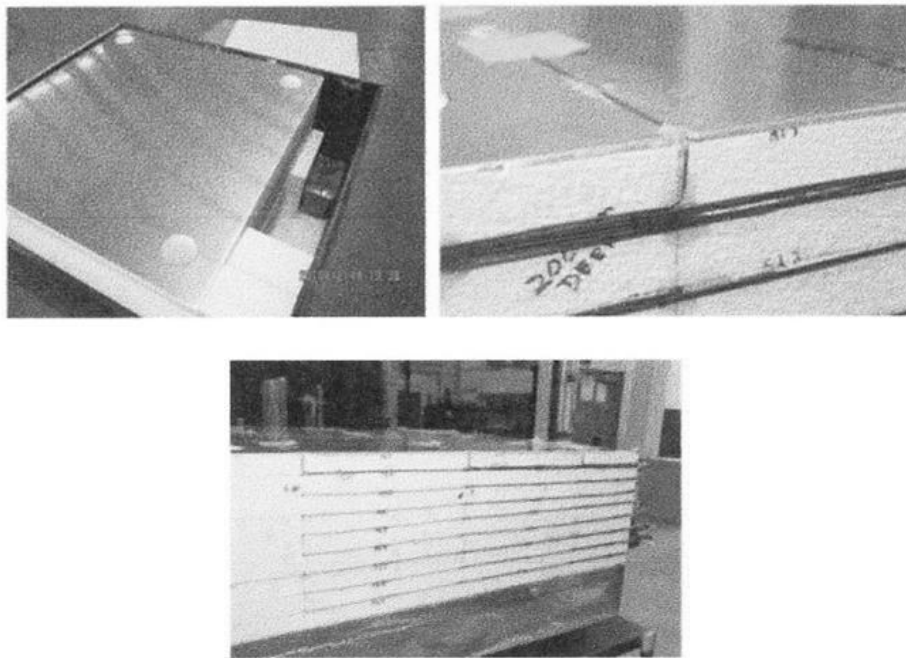


Figure 10: Sandia Laboratories Moss Sphere PS Insulation System

The upper left panel of Figure 10 is a close up photograph of the aluminum scrim. The upper right panel is a close-up photograph of the side and top of the insulation system. The lower panel is a wider photograph of the insulation system. The horizontal lines on the side of the foam are the thermocouple leads, and mark their depth within the foam. Bolted to the other

end of the foam assembly was a 19 mm thick aluminum plate. This aluminum plate was then rested against the liquid nitrogen tank wall. Completely assembled, a gap of 1382 mm was left between the weather cover and the insulation system.

The air gap was purged with nitrogen before, during, and after the experiment. The experimental system was allowed several hours before testing to come to steady-state with the liquid nitrogen tank. The experiment began when the heating lamps were turned on, and it ran for 40 minutes. After 40 minutes the lamps were turned off and the system was allowed to cool. Temperature and heat flux measurements were recorded throughout the 40 min experimental run and for an unspecified time before and after.

The exact results of the phase two testing are proprietary and not reported, but some generalized results were. The Moss Sphere polystyrene insulation system was found to completely ablate before the 40 minute mark. How long before 40 minutes was not specified. It was also found that after the foam failure a flux of less than 7 kW/m^2 into the tank was measured. This is contrary to the expected result of very high fluxes after insulation failure. Sandia expected fluxes of 170 to 190 kW/m^2 based on the LN2 tank surface having a sooted surface emissivity of 0.85-0.9. Smoke was observed leaking out of the enclosure during testing, and smoke obscuration was offered as a possible reason for the low heat flux into the LN2. Calculations by Sandia suggested a soot density of 100 ppm could account for the low flux. However, the smoke calculations did not match recorded temperature profiles. Convection created by the nitrogen purge was suggested to explain the difference in temperature profiles. Finally, Sandia concluded that heat fluxes ranging from 5 to 10 kW/m^2 would not over-pressurize the system, and that current pressure relief sizing is adequate.

Computational Fluid Dynamics

Finite Element Method

(The following section contains excerpts from [9])

The finite element method (FEM), a numerical scheme used for solving differential equations, is used by COMSOL. The method is a generalization of the variational and weighted residual methods, which are based upon the idea that the solution to a differential equation can be represented as a linear combination of unknown parameters and selected functions. Where the unknown parameters satisfy the differential equation, and the functions, called approximation functions, satisfy the boundary conditions. FEM applies these methods by dividing the problem domain into a number of simple geometric shapes, called finite elements. These elements allow for systematic generation of the approximation functions using concepts from interpolation theory. Therefore, the FEM can be viewed as the piecewise application of the variational and weighted residual methods. FEM consists of six major steps for a typical problem, the first four of which will be discussed in greater detail.

1. Discretization of the domain into a set of finite elements
2. Weak formulation of the differential equation
3. Development of finite element model using weak form
4. Assembly of elements to obtain global system of algebraic equations
5. Calculation of solution
6. Post-computational analysis

Discretization of domain

Let the problem domain be defined by Ω and the problem boundary by Γ . The domain of a single finite element will be defined by Ω^e and the non-overlapping sum of all the finite elements by Ω^h . Depending on the original complexity of the geometry of Ω , Ω^h may only be an approximation. Let the unknown variable T be approximated across a finite element by T^e where:

$$T(x, y) \approx T^e(x, y) = \sum_{j=1}^n T_j^e \psi_j^e(x, y).$$

T_j^e represents the values of $T^e(x,y)$ at n number of points across the element called nodes. The approximation functions at each node, ψ_j^e , are chosen to be polynomials of undetermined parameters T_j^e . Polynomials are used because they can be easily derived from interpolation theory and because they can be exactly evaluated by numerical integration. Using T_j^e as undetermined parameters imposes continuity across element boundaries.

Weak Formulation

The weak form of the differential equation is a weighted integral statement that is equivalent to the differential equation and its associated natural boundary conditions. The value behind such a formulation is that it allows some differentials to be moved to the weight function reducing the overall order of the equation and reducing continuity requirements. The reducing, or weakening, of the continuity requirements lends the formulation its name. A weighted integral statement of any differential equation can be constructed and a weak form exists for any second or higher order equation. Weak form generation consists of three steps and will now be illustrated on the basic time independent heat transfer equation over a single element:

$$-\left[\frac{\partial}{\partial x} \left(k_{xx} \frac{\partial T}{\partial x} \right) + \frac{\partial}{\partial y} \left(k_{yy} \frac{\partial T}{\partial y} \right) \right] = Q.$$

Step one is to move all nonzero terms to one side, multiply by a weight function, w , and integrate over Ω^e creating a weighted residual statement of the above equation:

$$0 = \int_{\Omega^e} w \left[-\frac{\partial}{\partial x} \left(k_{xx} \frac{\partial T}{\partial x} \right) - \frac{\partial}{\partial y} \left(k_{yy} \frac{\partial T}{\partial y} \right) - Q(x,y) \right] dx dy.$$

For n independent choices of w we obtain n linearly independent algebraic equations called the weighted residual finite element model. The second step is to equally distribute the differentiation among T and w by using the Green-Gauss Theorem on the first two terms in the above equation

$$0 = \int_{\Omega^e} \left(k_{xx} \frac{\partial w}{\partial x} \frac{\partial T}{\partial x} + k_{yy} \frac{\partial w}{\partial y} \frac{\partial T}{\partial y} - wQ \right) dx dy - \oint_{\Gamma^e} w \left(k_{xx} \frac{\partial T}{\partial x} n_x + k_{yy} \frac{\partial T}{\partial y} n_y \right) ds$$

where Γ^e is the element boundary, s is the arc length, and n_x, n_y are normal vectors. The third and final step is to notice that the term in the surface integral above is the natural boundary condition for heat transfer multiplied by the weight function and then simply rewrite the above equation:

$$0 = \int_{\Omega^e} \left(k_{xx} \frac{\partial w}{\partial x} \frac{\partial T}{\partial x} + k_{yy} \frac{\partial w}{\partial y} \frac{\partial T}{\partial y} - wQ \right) dx dy - \oint_{\Gamma^e} w q_n ds$$

where q_n is the heat flux normal to the element boundary. The second order nature of the original heat equation would require our polynomial approximation functions to be twice differentiable. This would require quadratic or higher ordered polynomials. With this weak formulation of the heat function, the approximation functions are only required to be once differentiable allowing for first order polynomials.

Development of Model

By taking the summation approximation of T^e and substituting it into the weak formulation yields:

$$0 = \int_{\Omega^e} \left[\frac{\partial w}{\partial x} \left(k_{xx} \sum_{j=1}^n T_j^e \frac{\partial \psi_j^e}{\partial x} \right) + \frac{\partial w}{\partial y} \left(k_{yy} \sum_{j=1}^n T_j^e \frac{\partial \psi_j^e}{\partial y} \right) - wQ \right] dx dy - \oint_{\Gamma^e} w q_n ds.$$

n linearly independent algebraic equations are required to solve for n unknowns, $T_1^e, T_2^e, \dots, T_n^e$. The solution is achieved by choosing n independent functions of w and setting them equal to ψ_j^e . Setting the weight functions equal to the approximation functions is called the Galerkin method. By substituting ψ_j^e in for w , the n linearly independent algebraic equations are generated:

$$\sum_{j=1}^n K_{ij}^e T_j^e = Q_i^e + q_i^e$$

where

$$K_{ij}^e = \int_{\Omega^e} \left(k_{xx} \frac{\partial \psi_i^e}{\partial x} \frac{\partial \psi_j^e}{\partial x} + k_{yy} \frac{\partial \psi_i^e}{\partial y} \frac{\partial \psi_j^e}{\partial y} \right) dx dy,$$

$$Q_i^e = \int_{\Omega^e} Q \psi_i^e dx dy,$$

and

$$q_i^e = \oint_{\Gamma^e} q_n \psi_i^e ds.$$

In matrix notation:

$$[K^e]\{T^e\} = \{Q^e\} + \{q^e\}$$

where the indexing i corresponds to the element number and j corresponds to the node number within element i . The matrix form of the equation is referred to as the finite element model of our starting heat equation. The bilinear form created by the weak form development makes the coefficient matrix, K^e , symmetric.

The polynomial equations to be used as the approximation functions will now be developed using interpolation theory. In approximating T^e , ψ^e must be continuous, complete, and have linearly independent terms. From the previous development, it is known that ψ^e must be at least linear in x and in y , giving the simplest possible polynomial below:

$$T^e(x,y) = c_1^e + c_2^e x + c_3^e y.$$

The number of independent terms required dictates the shape and degrees of freedom of the elements. The three constants must define three values of T^e at three unique points across Ω^e . Obviously the shape defined by three points is a triangle, which is the most popular finite element shape and the default shape used by COMSOL. Using the above polynomial, the approximation functions for a triangular element can now be written:

$$\psi_j^e(x,y) = 1/2A^e(a_j^e + b_j^e x + c_j^e y)$$

where A^e is the area of the element and a_j^e, b_j^e, c_j^e are defined by the node coordinates x_j, y_j :

$$a_j^e = x_i y_k - x_k y_i; \quad b_j^e = y_i - y_k; \quad c_j^e = x_k - x_i$$

where $j \neq i \neq k$, and j, i, k are permuted in a natural order. These approximation functions only interpolate T^e at the nodes and not its derivatives. These types of interpolation functions are called Lagrange interpolation functions and satisfy the following properties:

$$\psi_j^e(x_i, y_i) = \delta_{ji}; \quad \sum_{j=1}^3 \psi_j^e(x, y) = 1.$$

Assembly of Elements

All the finite elements must be assembled to obtain global equations across Ω^h , such that they maintain continuity of T^e and balance the heat flux across all element interfaces. To do this, local element node numbers must be related to the corresponding overall global node numbers. These correspondence relationships are unique to each problem's mesh geometry and node numbering scheme and can only be illustrated through example (Figure 11).

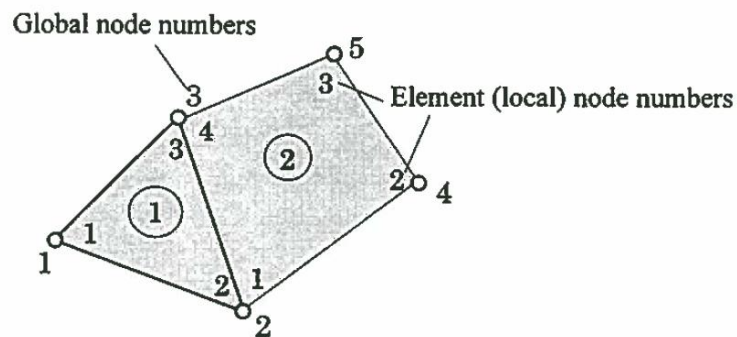


Figure 11: Global-Local Correspondence of Nodes for Assembly

The correspondence relations for Figure 11 are:

$$T_j^i = T_k, T_1^1 = T_1, T_2^1 = T_1^2 = T_2, T_3^1 = T_4^2 = T_3, T_2^2 = T_4, T_3^2 = T_5$$

where j is the local node number of element i , and k is the global node number. Correspondence from local to global nodes imposes the continuity of T . The algebraic equations for each element of the example can now be written using the finite element model developed earlier:

Element 1

$$K_{11}^1 T_1^1 + K_{12}^1 T_2^1 + K_{13}^1 T_3^1 = Q_1^1 + q_1^1$$

$$K_{21}^1 T_1^1 + K_{22}^1 T_2^1 + K_{23}^1 T_3^1 = Q_2^1 + q_2^1$$

$$K_{31}^1 T_1^1 + K_{32}^1 T_2^1 + K_{33}^1 T_3^1 = Q_3^1 + q_3^1$$

Element 2

$$K_{11}^2 T_1^2 + K_{12}^2 T_2^2 + K_{13}^2 T_3^2 + K_{14}^2 T_4^2 = Q_1^2 + q_1^2$$

$$K_{21}^2 T_1^2 + K_{22}^2 T_2^2 + K_{23}^2 T_3^2 + K_{24}^2 T_4^2 = Q_2^2 + q_2^2$$

$$K_{31}^2 T_1^2 + K_{32}^2 T_2^2 + K_{33}^2 T_3^2 + K_{34}^2 T_4^2 = Q_3^2 + q_3^2$$

$$K_{41}^2 T_1^2 + K_{42}^2 T_2^2 + K_{43}^2 T_3^2 + K_{44}^2 T_4^2 = Q_4^2 + q_4^2.$$

At the interface between the two elements, global node 2 to 3, the heat flux should be equal and opposite. To impose this condition, the second equation of element 1 must be added to the first equation of element 2, and the third equation of element 1 must be added to the fourth equation of element 2. In a more general sense, the assembly of elements is carried out by adding the local coefficient values, K_{ij}^e , Q_i^e , and q_i^e to the appropriate location of the global coefficient matrices.

Derivatives of $T^e(x,y)$ will not be continuous across element boundaries because continuity was only imposed for T^e . If other properties, such as derivative of T^e , are to be made continuous, they will need to be added as nodal variables increasing the degree of interpolation.

Time Dependent Problems

The discussion so far has been for a stationary differential equation. The FEM discussion will now be expanded to include time dependent problems. The numerical solution to an initial value problem requires two steps of approximation. The first step is the spatial approximation and involves a weak formulation and discretization of the domain following the procedure described earlier. The one difference is that the development results in a set of ordinary differential equations with time instead of a set of algebraic equations. The second step of approximation is the temporal approximation of the ordinary differential equations. This involves numerical integration using finite difference schemes. These two approximations will result in a set of algebraic equations of T_j^e and t_{n+1} in terms of known values from previous time steps.

Starting with the time dependent heat equation, the same weak formulation over Ω^e can be followed as before. By multiplying the differential equation by a weight function and integrating, distributing the differentiation using the Green-Gauss Theorem, and then replacing the boundary integral with a flux variable, the time dependent weak formulation is obtained:

$$0 = \int_{\Omega^e} \left[w \left(\rho C \frac{\partial T}{\partial t} - Q_s \right) + k_{xx} \frac{\partial w}{\partial x} \frac{\partial T}{\partial x} + k_{yy} \frac{\partial w}{\partial y} \frac{\partial T}{\partial y} \right] dx dy - \oint_{\Gamma^e} (q_n - q_c) w ds.$$

Using a weight function not dependent on time, and assuming separation of space and time dependence, the equation for T^e can be written:

$$T^e(x, y, t) = \sum_{j=1}^n T_j^e(t) \psi_j^e(x, y).$$

w can then be replaced with ψ_i^e , and substitute the T^e equation in for T as before, to obtain the finite element model:

$$[M^e] \{\dot{T}^e\} + [K^e] \{T^e\} = \{Q^e\} + \{q^e\}$$

where

$$\dot{T} = \frac{\partial T}{\partial t},$$

$$M_{ij}^e = \int_{\Omega^e} \rho C \psi_i \psi_j dx dy,$$

$$K_{ij}^e = \int_{\Omega^e} \left(k_{xx} \frac{\partial \psi_i}{\partial x} \frac{\partial \psi_j}{\partial x} + k_{yy} \frac{\partial \psi_i}{\partial y} \frac{\partial \psi_j}{\partial y} \right) dx dy,$$

$$Q_i^e = \int_{\Omega^e} \psi_i Q(x, y, t) dx dy,$$

and

$$q_i^e = \oint_{\Gamma^e} \psi_i (q_n - q_c) ds.$$

In general, the above equations cannot be integrated analytically and must be further approximated by discretization in time to obtain a set of algebraic equations. The most common temporal approximation methods are all part of the θ -family, which are one parameter approximation methods:

$$\{T\}_{n+1} = \{T\}_n + \Delta t [(1-\theta)\{\dot{T}\}_n + \theta\{\dot{T}\}_{n+1}], \quad 0 \leq \theta \leq 1.$$

By substituting this equation into the time derivative of our finite element mode, the fully discretized approximation of the time dependent heat equation is obtained as a system of algebraic equations. Four different values of θ are associated with four common approximation schemes:

$\theta = 0$, forward difference

$\theta = 0.5$, Crank-Nicolson

$\theta = 2/3$, Galerkin

$\theta = 1$, backward difference.

Arbitrary Lagrangian-Eulerian Methods (ALE)

(Following section contains excerpts from [10])

In numerical computations, the modeling of problems with moving boundaries or interfaces (Stefan Problem) requires development of an appropriate kinematical description of

the continuum. The two classical descriptions of motion most often utilized by computational algorithms are the Lagrangian and the Eulerian. In a Lagrangian description, each individual mesh node follows exactly with the motion of its associated material particle. This description is most often used in structural mechanics and is very good at exactly tracking the movement of free surfaces and phase interfaces. However, it does not handle large distortions well without frequent remeshing. In contrast, the Eulerian description fixes the mesh points and allows the continuum to move with respect to the mesh grid. Often used in fluid dynamics, this description easily handles large distortions but at the cost of precisely tracking free surfaces and phase interphases. The ALE method tries to combine the strengths of these two kinematical descriptions while minimizing their weaknesses. As the name suggests, this is achieved by arbitrarily moving the mesh points in some specified way that is neither quite Lagrangian nor Eulerian. Figure 12 illustrates this idea with a one dimensional example of the three descriptions.

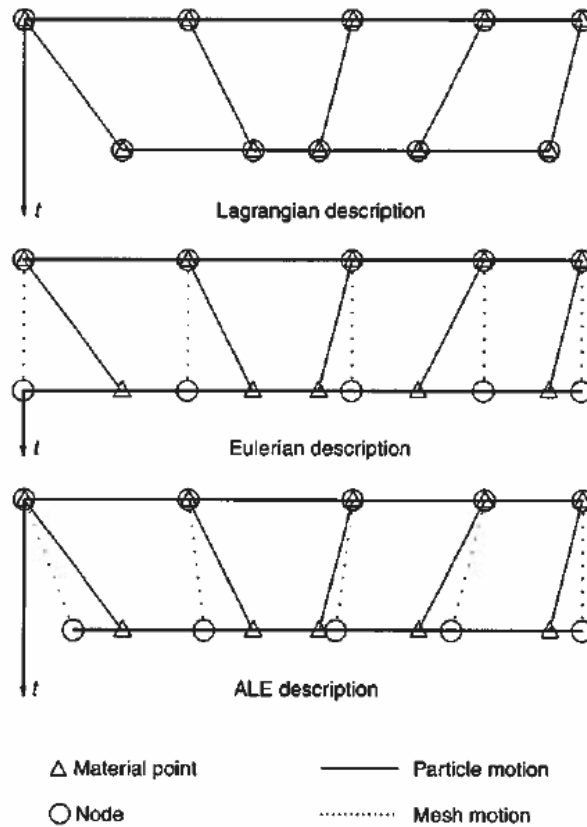


Figure 12: One-Dimensional Example of Lagrangian, Eulerian, and ALE Mesh and Particle Motion

In the ALE method, three frames of reference are used in the description of motion: material frame (coordinates x), spatial frame (coordinates X), and reference frame (coordinates χ). This in turn leads to three different mapping operators between the frames: reference to spatial Ψ , reference to material Φ , and spatial to material φ , as illustrated in Figure 13.

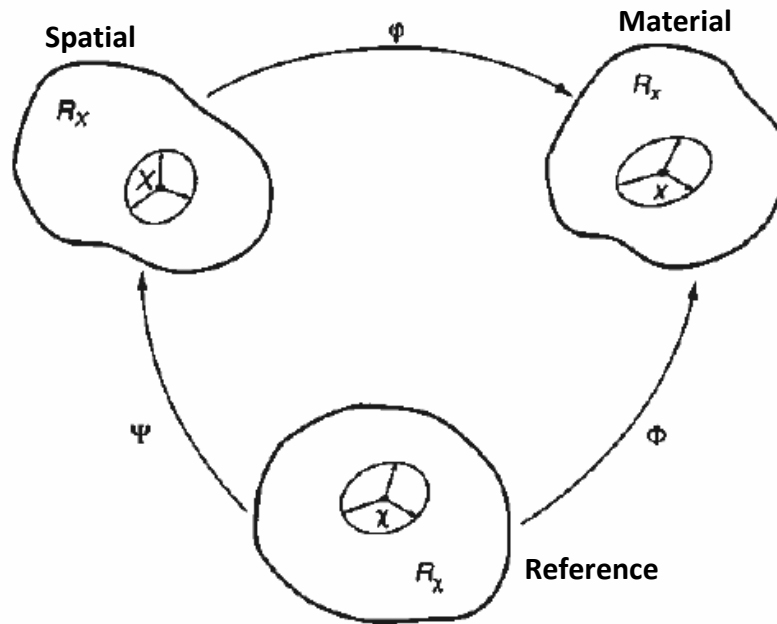


Figure 13: Relations Between ALE Three Frames of Reference

The mapping operator φ , which maps the spatial frame to the material frame or maps the mesh points to the material points:

$$(X, t) \rightarrow \varphi(X, t) = (x, t),$$

its gradient

$$\frac{\partial \varphi}{\partial (X, t)} = \begin{pmatrix} \frac{\partial x}{\partial X} & v \\ 0^T & 1 \end{pmatrix},$$

where 0^T is the null row vector and with velocity v , the velocity of material points with respect to the mesh point:

$$v(X, t) = \left. \frac{\partial x}{\partial t} \right|_X.$$

The mapping function Φ , which maps the reference frame to the material frame:

$$(\chi, t) \rightarrow \Phi(\chi, x) = (x, t),$$

its gradient

$$\frac{\partial \Phi}{\partial(\chi, t)} = \begin{pmatrix} \frac{\partial x}{\partial \chi} & \hat{v} \\ 0^T & 1 \end{pmatrix},$$

with velocity \hat{v} , the velocity of the material points with respect to the reference frame:

$$\hat{v}(\chi, t) = \left. \frac{\partial x}{\partial t} \right|_\chi.$$

The mapping function Ψ is best utilized by its inverse Ψ^{-1} , where Ψ^{-1} maps the spatial frame to the reference frame:

$$(X, t) \rightarrow \Psi^{-1}(X, t) = (\chi, t),$$

its gradient

$$\frac{\partial \Psi^{-1}}{\partial(X, t)} = \begin{pmatrix} \frac{\partial \chi}{\partial X} & w \\ 0^T & 1 \end{pmatrix},$$

with velocity w , velocity of the reference frame with respect to the mesh points:

$$w(X, t) = \left. \frac{\partial \chi}{\partial t} \right|_X.$$

A relationship between the three velocities can be obtained by differentiating:

$$\varphi = \Phi \circ \Psi^{-1}$$

which yields

$$\mathbf{v} = \hat{\mathbf{v}} + \frac{\partial \mathbf{x}}{\partial \boldsymbol{\chi}} \cdot \mathbf{w}.$$

This equation allows the definition of the convective velocity \mathbf{c} , the relative velocity between the material and mesh frames:

$$\mathbf{c} = \mathbf{v} - \hat{\mathbf{v}} = \frac{\partial \mathbf{x}}{\partial \boldsymbol{\chi}} \cdot \mathbf{w}.$$

In order to use the differential equations in the ALE reference frame, a relation must be developed between the material time derivative (used in the differential equations) to the reference time derivative. Let $f^M(\mathbf{x},t)$, $f^R(\boldsymbol{\chi},t)$, and $f^S(\mathbf{X},t)$ be defined as a scalar quantity in the material, reference, and spatial frames respectively. Then to transform the scalar quantity from the spatial frame to the material frame:

$$f^S(\mathbf{X},t) = f^M(\boldsymbol{\varphi}(\mathbf{X},t),t).$$

Taking the block multiplication of the matrix form of the above equations gradient gives an equation relating the material and spatial time derivatives:

$$\frac{\partial f^S}{\partial t} = \frac{\partial f^M}{\partial t} + \frac{\partial f^M}{\partial \mathbf{x}} \cdot \mathbf{v}.$$

Dropping the frame of reference superscripts gives:

$$\left. \frac{\partial f}{\partial t} \right|_{\mathbf{X}} = \left. \frac{\partial f}{\partial t} \right|_{\mathbf{x}} + \mathbf{v} \cdot \nabla f,$$

or

$$\frac{df}{dt} = \frac{\partial f}{\partial t} + \mathbf{v} \cdot \nabla f.$$

Using a similar procedure to transform from the special frame to the material frame:

$$f^S(\mathbf{X},t) = f^R(\boldsymbol{\Psi}^{-1}(\mathbf{X},t),t),$$

gives

$$\frac{\partial f^S}{\partial t} = \frac{\partial f^R}{\partial t} + \frac{\partial f^R}{\partial x} \cdot w.$$

Substitution into the equation for c into w and dropping frame of reference superscripts, gives the fundamental ALE relationship between material time derivative, reference time derivatives, and spatial gradient:

$$\left. \frac{\partial f}{\partial t} \right|_X = \left. \frac{\partial f}{\partial t} \right|_x + \frac{\partial f}{\partial x} \cdot c = \left. \frac{\partial f}{\partial t} \right|_x + c \cdot \nabla f.$$

Using the above equation for relating time derivatives, the conservation equations can now be translated from their standard Eulerian form into an ALE form:

$$\begin{aligned} \text{Mass: } \frac{d\rho}{dt} &= \left. \frac{\partial \rho}{\partial t} \right|_x + v \cdot \nabla \rho = -\rho \nabla \cdot v \\ \text{Momentum: } \rho \frac{dv}{dt} &= \rho \left(\left. \frac{\partial v}{\partial t} \right|_x + (v \cdot \nabla)v \right) = \nabla \cdot \sigma + \rho b \\ \text{Energy: } \rho \frac{dE}{dt} &= \rho \left(\left. \frac{\partial E}{\partial t} \right|_x + v \cdot \nabla E \right) = \nabla \cdot (\sigma \cdot v) + v \cdot \rho b \end{aligned}$$

where σ is the Cauchy stress tensor and b is the specific body force vector. All that needs to be done to transform these equations into ALE form is the replace the convective terms defined by the material frame velocity v with the convective velocity c :

$$\begin{aligned} \text{Mass: } \left. \frac{\partial \rho}{\partial t} \right|_x + c \cdot \nabla \rho &= -\rho \nabla \cdot v \\ \text{Momentum: } \rho \left(\left. \frac{\partial v}{\partial t} \right|_x + (c \cdot \nabla)v \right) &= \nabla \cdot \sigma + \rho b \\ \text{Energy: } \rho \left(\left. \frac{\partial E}{\partial t} \right|_x + c \cdot \nabla E \right) &= \nabla \cdot (\sigma \cdot v) + v \cdot \rho b. \end{aligned}$$

The last component of the ALE method is to prescribe the mesh updating procedures. Assigning the mesh node velocities or displacements at each time step of the problem is not an easy task.

It is often very problem specific and strongly connected with the convergence of the computational solution. There are however two general strategies often employed by computational solvers, mesh regulation and mesh adaptation. Mesh regulation updates the mesh nodes in such a way as to keep the mesh as geometrically regular as possible. This technique minimizes large distortions and helps prevent mesh inversion. The goal of mesh adaptation is to concentrate node elements in areas of large gradient. This allows for greater accuracy with a given number of nodes.

Material Properties

The COMSOL models developed in this work are highly dependent on the physical properties used to describe the domain. This has led to the study and evaluation of all the physical properties and their effects on the polystyrene regression rate. The four most important values required are: density, heat capacity, thermal conductivity, and change in enthalpy. Also of importance are the maximum vaporization temperature and the convection heat transfer coefficient.

Density

In the BCM model a density of 1060 kg/m^3 was used. This is the value reported by BCM. Butler reports a value of 1040 kg/m^3 and literature searches indicated similar values [8]. BCM's value was chosen because their experiment is the focus of the model, and there is no more than one to two percent variance in reported values. Density values are also considered temperature independent, as there is a negligible change above the melting temperature. The Butler model requires two densities to adequately represent the experiment due to the structural nature of the foam. Below the melting temperature, a value of 26.5 kg/m^3 is used. This value was measured and reported by Butler and is consistent with literature values [8]. Above the melting point the BCM density is used. Any differences between the liquid state of the foam and the liquid state of the dense polystyrene are insignificant. All the physical properties above the melting temperature are the same in all models. Density shows up directly in the regression equation, making its effect significant. Our density values are known within a few percent, making any uncertainty in these values affect the regression rate by no more than a few percent.

Heat Capacity

Heat capacity values for all models are temperature dependent functions derived from data measured by NETZSCH Instruments, Inc. Samples of both the solid and the foam polystyrene used in Butler's work was sent to NETZSCH for differential scanning calorimetry (DSC) and thermogravimetric analysis (TGA). This analysis yielded heat capacity data over the

temperature range of 298-593 degrees K. The data match very closely with a linear fit: $4.5 \cdot T - 180$ J/kg/K for the solid material, and $4.2 \cdot T - 18$ J/kg/K for the foam, where T is in units of K (Figure 14).

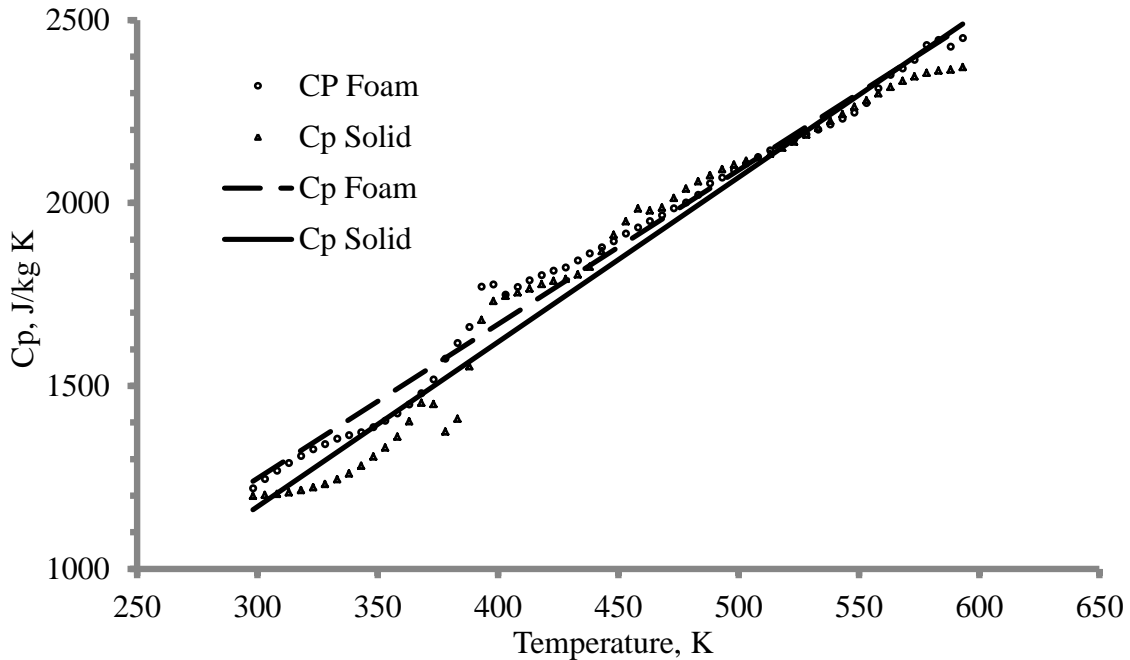


Figure 14: NETZSCH Heat Capacity Data

Several sets of data were found in the literature for similar types of solid polystyrene over similar temperature ranges [11]. The different literature data sets and the Netzsch data set all agreed within about ten percent. Heat capacity does not directly affect the regression equation and a ten percent uncertainty was considered not likely to be significant. This was checked by conducting a run of the transient BCM model using one of the literature heat capacity data sets. No significant change in the regression rate was observed. The NETZSCH data was chosen for use in the models because BCM did not report any heat capacity values, the data was for the specific materials used by Butler, and it allowed a single data source for both solid and foam materials. The only concern with the heat capacity values used is that the NETZSCH data stops at 593 K; the COMSOL model extends the linear relation up to 719 K. At around 593 K, vaporization of the material starts and Netzsch reports that their instruments cannot get good

measurements once this happens. Not much data above 593 K was found in the literature, but what data there was suggests that the temperature dependence remains linear [11].

Thermal Conductivity

Thermal conductivity data was not reported by BCM or Butler and was derived from literature. Consistent thermal conductivity data over the temperature range required for the models was hard to find, but good thermal diffusivity values were found [12]. It was reported that above the melting temperature, thermal diffusivity remains constant. If thermal diffusivity and density is known to be relatively constant while heat capacity is not, then thermal conductivity must also be temperature dependent. A thermal diffusivity value of $0.0008 \text{ cm}^2/\text{s}$ [13] was combined with the density and heat capacity values above to calculate a temperature dependent thermal conductivity of $0.00038146 \cdot T - 0.0152 \text{ W/m/K}$, where T is in units of K. Below the melting point, the literature shows a temperature dependent thermal diffusivity and suggests a constant value for thermal conductivity [13]. In the BCM models, a value of 0.127 W/m/K was used below the melting point. This value corresponds to the linear relation value at the melting temperature. For the foam material, a range of values was found depending on the blowing agent used during manufacture and the age of the material. Two values were explored, 0.034 W/m/K and 0.021 W/m/K , corresponding to the limits of the range [14]. The difference in the regression rates for the two values was noticeable and both values were used in the Butler model.

Change in Enthalpy

The change in enthalpy term is a temperature dependent term defined as the energy absorbed by the material as it moves from the initial ambient temperature to top surface temperature. Initially it is zero, and increases to a maximum at steady-state. It appears directly in the regression equation, and is the only place in the model it is used. The steady-state maximum value is analogous to the H_{rvum} term from the steady-state analysis done by BCM and Butler. It incorporates the energy required to heat the material through the temperature range, and any heat associated with melting, collapsing, vaporizing, or other physiochemical processes

that might occur. The maximum value used in the BCM model is simply the H_{rvum} value of 1980 J/g reported in their paper, and is associated with the maximum temperature of 719 K. This maximum is more important than the transition values because the solution is mostly in the steady-state region. In their paper, BCM try to confirm this value by calculating the heat required to depolymerize the styrene to a monomer, the heat required to vaporize liquid monomer, and the heating of the gaseous monomer to 719 K. They report this summation as 1833 J/g. The H_{rvum} value Butler reports for his dense polystyrene experiments was 1731 J/g. A value can be calculated from the NETZSCH data by integrating the heat capacity equation from 298 to 719 K and then adding to it the heat of vaporization. This value is 1618.1 J/g. For the foam material, the only values are the one from Butler and one calculated from the Netzsch data. These values are 1592 J/g and 1616.8 J/g respectively.

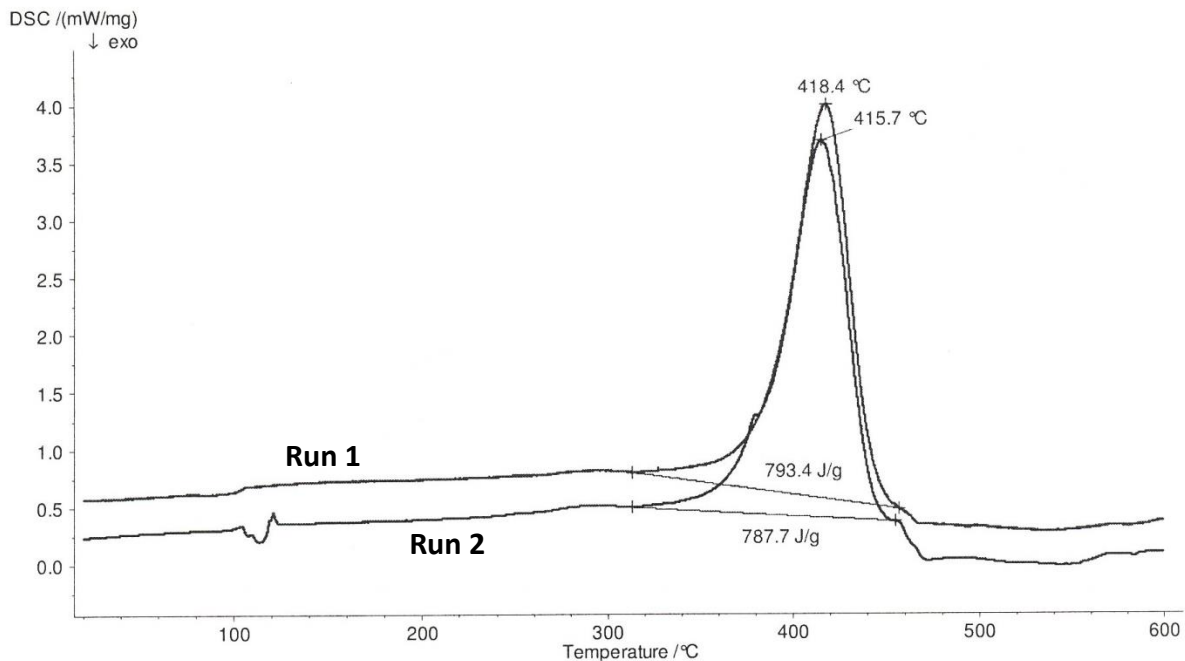


Figure 15: NETZSCH Foam Polystyrene DSC Data

For the solid material, the temperature dependence of H can be determined from DSC data. Through a simple unit conversion, DSC data can be replotted as the total energy capacity of the material versus temperature. This curve can then be integrated to give $H(T)$, where $H(T)$

is equal to the integration of the energy capacity curve from 298 K to any temperature T. When contacted, NETZSCH said that their DSC data could not be converted into energy capacity data through a simple unit conversion (Figure 16).

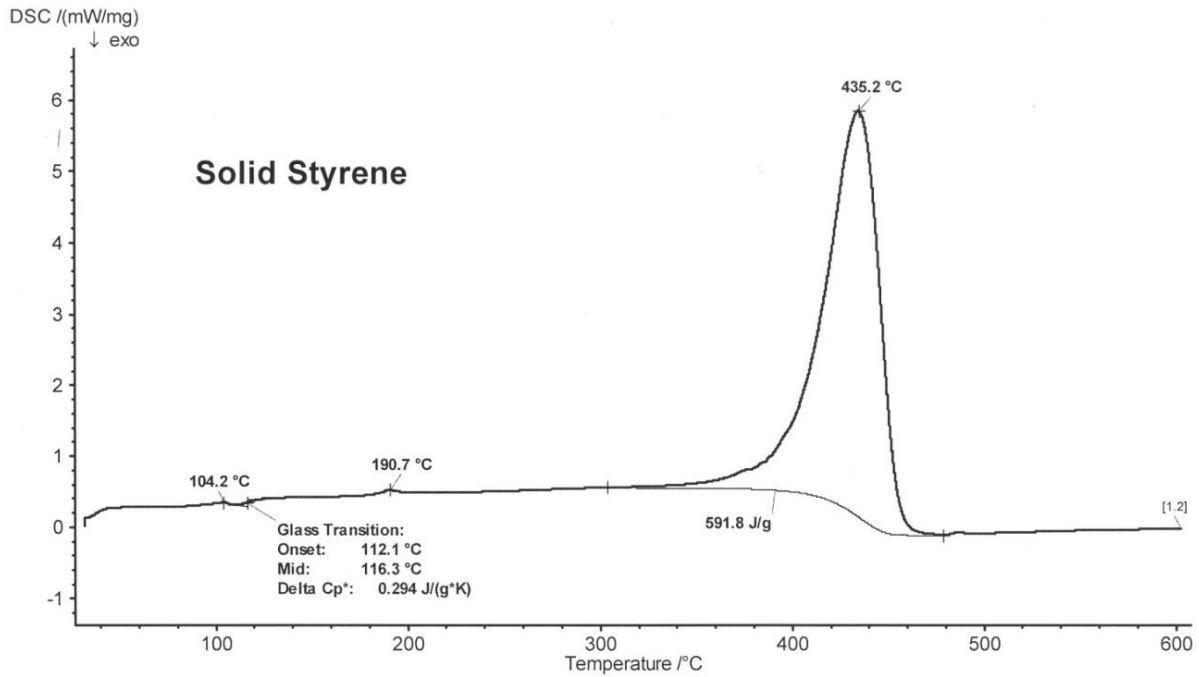


Figure 16: NETZSCH Dense Polystyrene DSC Data

This has led to the creation of an approximate DSC curve. The created DSC curve consists of three zones, each described by a linear fit (Figure 17).

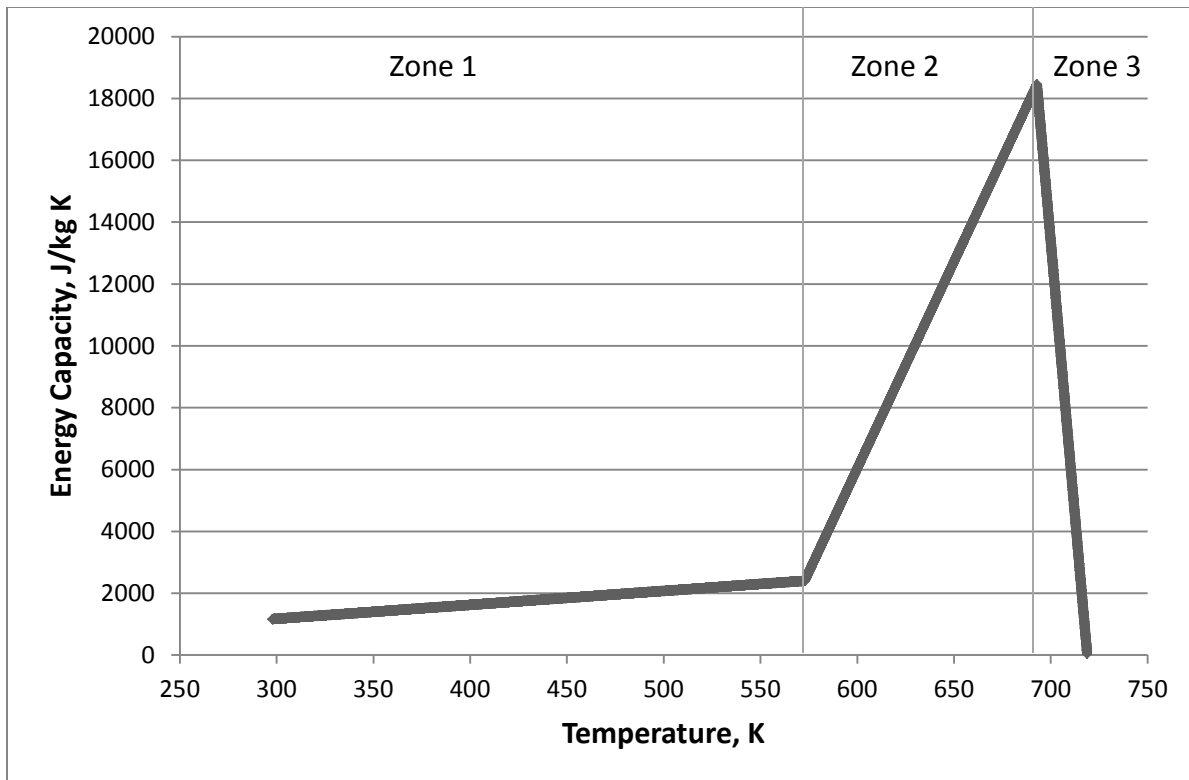


Figure 17: Approximate DSC Curve

The first zone is a pre-vaporization zone ranging from 298 to 573 K. The line in this zone is described identically by the heat capacity. The second zone is the first part of the vaporization, where the energy as a function of temperature is increasing. This zone ranges from 573 to 693 K. The third zone is the second part of vaporization, where the energy is decreasing with temperature. This zone ranges from 693 to 719 K. The vaporization onset temperature was taken from the NETZSCH TGA data (Figure 18) defined as the temperature where mass loss starts to occur. The final temperature was taken from BCM.

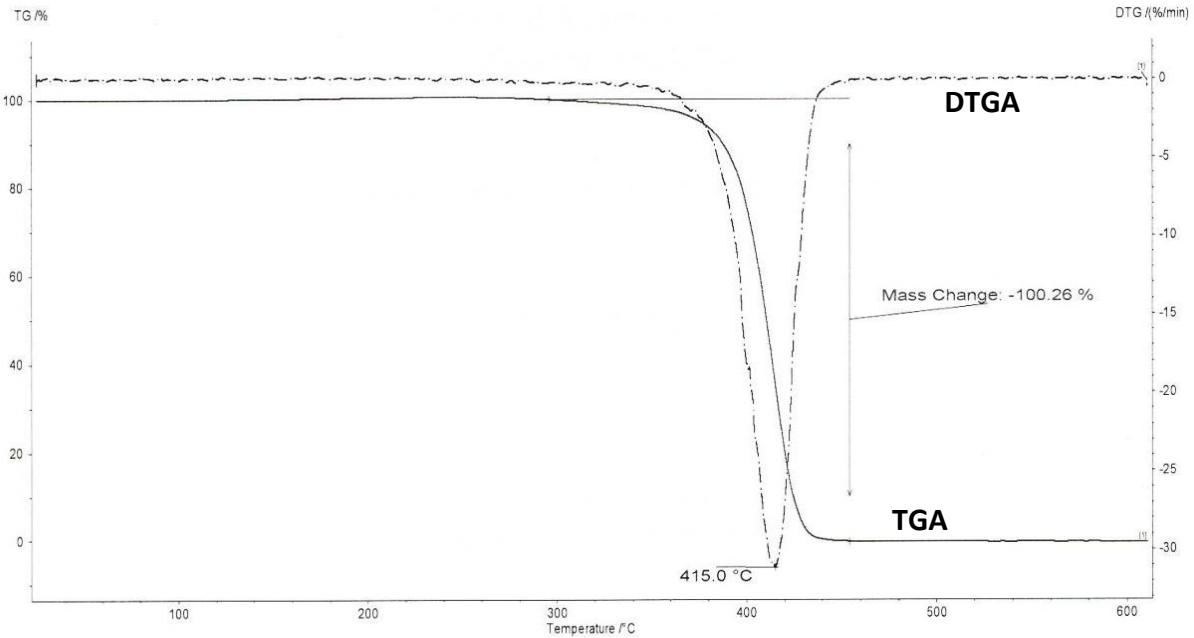


Figure 18: NETZSCH Dense Polystyrene TGA and DTGA Data

Both values are in agreement with the NETZSCH DSC and TGA data. The zone 2/zone 3 boundary temperature is taken from the NETZSCH DSC. The energy at the first two points is known from the heat capacity, and the energy of the last point is set to zero. The value at the third point is unknown, but the total area under the curve must be equal to the steady-state H_{rvum} term. Point three is then calculated based on the total area, and then an equation for all three lines can be determined. This created data set is then integrated from 298 K to each temperature value creating a temperature dependent H curve (Figure 19). A similar process could be used for the foam material based on either the Butler or NETZSCH data and the maximum temperature reached in the foam experiments.

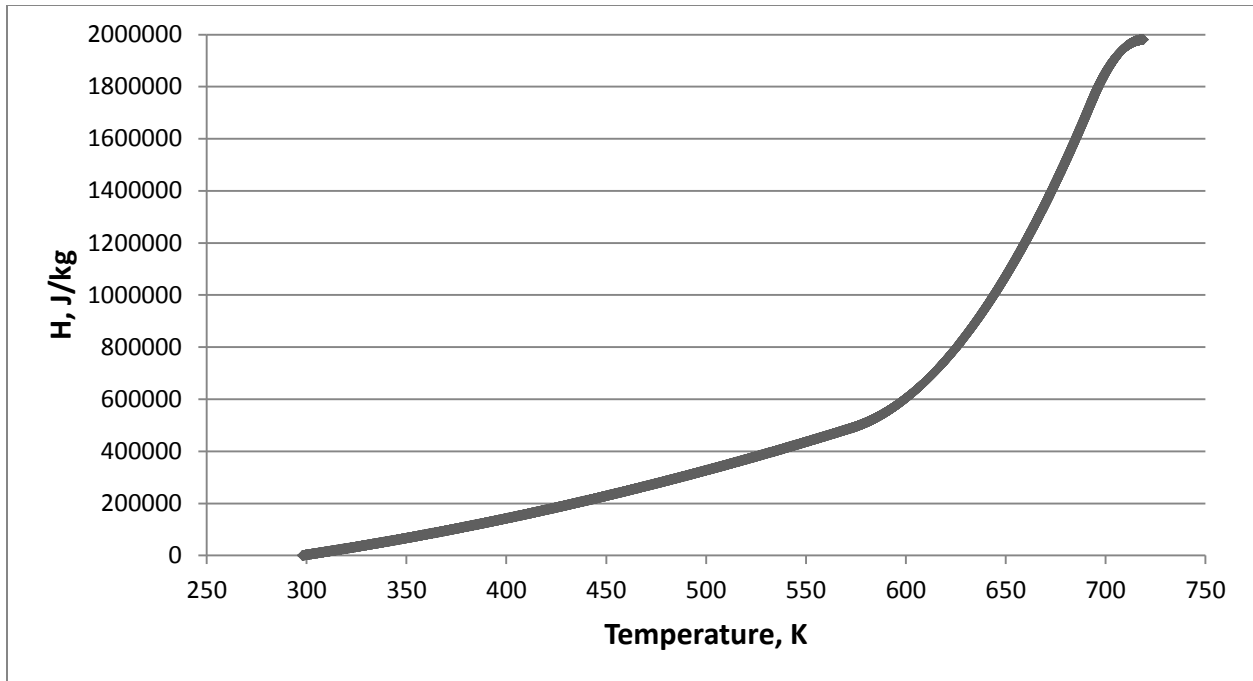


Figure 19: Temperature Dependent H

Any uncertainty in the change in enthalpy term is directly reflected in the regression rate. This term remains the largest uncertainty in the regression rate for all the models.

Vaporization Temperature

Vaporization temperature is another important value for the modeling. The vaporization of polystyrene occurs over a large range, but only the final or highest vaporization temperature is needed for the model. BCM's temperature measurements showed a maximum value of 719 K. NETZSCH performed two DSC and one TGA analysis for both the dense and the foam material.

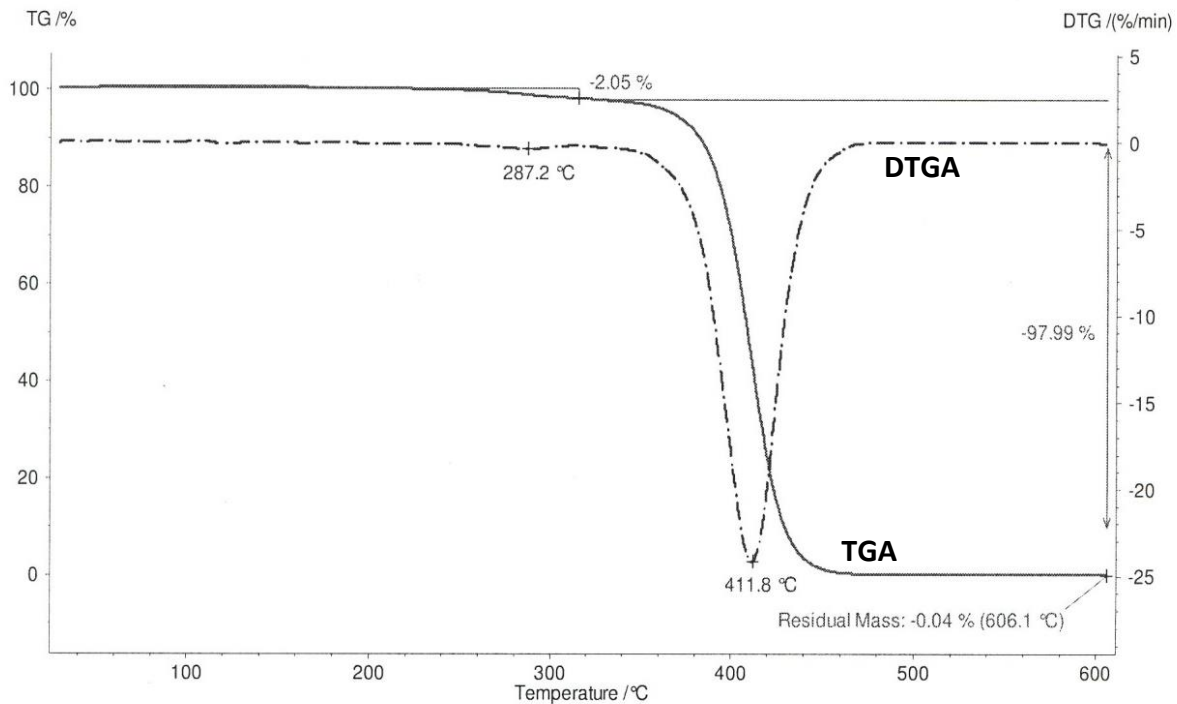


Figure 20: NETZSCH Foam Polystyrene TGA and DTGA Data

Depending on the data set used, the highest temperature where liquid polystyrene still exists ranges from around 710 to 730 K (Figure 20). The temperature reported by BCM was used in both the transient and steady-state BCM models. The vaporization temperature can affect the regression rate in three ways. Firstly, it changes the steady state heat into the material by changing the amount of re-radiation. Secondly, it changes the temperature profiles, which then changes the heat losses. Lastly, it changes the enthalpy term by changing the range over which heat capacity and the heat of vaporization must be summed. A lower temperature will decrease the enthalpy, increase the heat in, and decrease the heat losses. All three changes work in the same direction to increase the regression rate.

The 719 K maximum temperature used in the BCM models is of questionable applicability to the foam model. Due to the much faster regression of the foam through collapsing action, it is reasonable that the pseudo steady-state zone could occur at any temperature value between the melting and maximum vaporization temperatures. Unlike in the BCM experiments, Butler did not record any temperature information for his foam

experiments. If the foam experiments reached pseudo steady-state near the maximum vaporization temperature, mass loss rates for the foam experiments would be similar to those for the dense material experiments. Butler recorded the initial and final mass for two foam samples run through his experiments. Combined with the run times for these two experiments, an average mass loss rate was calculated for comparison to the solid material rates. Values of $3.2 \cdot 10^{-5}$ and $3 \cdot 10^{-5}$ g/cm²s were calculated at an incident heat flux of 32 kW/m². BCM and Butler both reported a value of $4.1 \cdot 10^{-4}$ g/cm²s at 50 kW/m² incident heat flux. Unfortunately, the two foam runs were at incident fluxes below the range of the solid material experiments preventing any direct comparison. The average mass loss rates calculated for the foam were over ten times smaller than the rates calculated for the solid material. This is a greater difference than expected to be caused by the difference in incident flux values. Polystyrene vaporization is slowest at its initial vaporization temperature and fastest at its highest temperature. The large difference in the regression rates calculated from the measured data suggests that the foam material was regressing at a lower temperature than was measured by BCM for the solid material. An estimate of what this temperature might be was achieved by combining experimental data and modeling. For all of the experimental foam runs, the approximate time to reach pseudo steady-state was calculated. COMSOL was then used to model this heat up phase. Each run of the model was stopped at one of the average time to pseudo steady-state values, and the top surface temperature was recorded. These temperatures values range between 640 K to 670 K. With only a 30 degree spread across multiple runs from a range of flux values, it is reasonable to assume that this range is a good approximation for the maximum temperature reached in the foam experiments. Looking at the DSC data, this range is in the middle of the vaporization zone and just before the peak of the energy capacity.

Computer Modeling

COMSOL

COMSOL, utilizing both FEM and ALE techniques, offers a very powerful tool for solving the complicated Stefan problem. In a paper by Carin, a simple temperature boundary condition phase change Stefan Problem is presented with a known analytical solution [15]. Carin solved the same problem with COMSOL and achieved good agreement with the analytical solution. Carin's work was repeated using COMSOL and also achieved good agreement. An example, presented by Carslaw and Jaeger as the analytic Neumann solution to the Stefan Problem, was then modeled and again good agreement was achieved between COMSOL and theory [16]. As one last check of COMSOL's capabilities, the Neumann solution for a change-of-density Stefan Problem was investigated. This being the most complex Stefan Problem with an analytical solution found, it provided a good test of COMSOL's capabilities before moving forward with the very complex polystyrene degradation problems. Once again, COMSOL provided good agreement with the analytical solution. These successes provided confidence that COMSOL is capable of modeling the degradation of polystyrene under severe heating conditions.

Models

Four different COMSOL models were built and used for investigation. A transient and a steady-state model were built to investigate the BCM experiments of the solid polystyrene. A transient model was used to investigate the Butler experiments of polystyrene foam. A transient model was built to investigate Sandia National Laboratory's large scale study of LNG insulation systems.

Modeling of the BCM experiments started with a transient model designed to physically represent the experiments as closely as possible. The model was run for sufficiently long times to approximate steady-state. As a check of the transient approximated steady-state a true steady-state model was created. A noticeable difference was discovered upon comparison of the two models. This difference is believed to be mostly explained by the different physics used in the steady-state model. This point is discussed further in the results and discussion section.

The physics of the steady-state model better represent the physics of the experiments, so a full investigation was done with the steady-state model instead of the transient.

The transient foam model uses the same physics as the transient solid model and includes the same deficiency. However, in the foam model this deficiency is minimized to the point of being negligible.

Radiation

Another important component of the models is how the incident radiation is handled. This consists of properly modeling the radiation heat flux in COMSOL and properly prescribing the surface emissivity. The experiments performed by BCM and Butler reported external heat fluxes in units of power over area using a Gardon gauge radiometer. The radiation boundary condition used in COMSOL requires the setting of an external temperature, and then calculates a flux using the boundary temperature and emissivity through the Stefan-Boltzmann law.

$$\dot{q}_{rad} = \varepsilon * \sigma * (T_{source}^4 - T_{surface}^4)$$

\dot{q}_{rad} : radiation heat flux, W/m²

ε : emissivity

σ : Stefan-Boltzmann constant, 5.67*10⁻⁸ W/m²/K⁴

T_{source} : temperature of radiation source, K

$T_{surface}$: temperature of incident surface, K

To translate the fluxes reported in experiment into an external temperature for COMSOL, the value was calculated as that of a black body radiating at a constant temperature. BCM and Butler tested the solid material over a range of approximately 50 to 63 kW/m². This corresponds to black body temperatures of 969 to 1026.7 K. Butler tested the foam material over a range of approximately 27 to 45 kW/m². This corresponds to temperatures of 830.7 to 943.9 K. The COMSOL radiation boundary condition also automatically calculates reradiation from the boundary and subtracts it from the flux. This means that as the boundary heats up to

its maximum temperature and becomes constant, the radiation flux starts at its maximum and decreases to a constant minimum value. This is consistent with Tewerson's work [17].

Surface Emissivity

The surface emissivity directly affects the boundary radiation flux, in turn affecting the heat-flux-in term in the regression equation. BCM reports an emissivity of 0.95 for the solid material. They offer no specifics as to how they got this value, but it is likely based on the fact that the samples contained carbon black. Literature values are unavailable as the carbon black was added specifically for BCM and Butler and is not normally in the product. In the BCM models, values over a range of 1 to 0.85 were investigated. The foam material is an opaque, matte light blue color when solid and an opaque, glossy dark blue color when melted. It was assumed that the foam would not be more emissive than the solid material, but likely within a similar range. A range of 1 to 0.8 was investigated in the Butler model. In the Sandia experiments and model, the polystyrene is protected from radiation by a thin aluminum scrim. The emissivity of this scrim was not reported and estimating its value was one objective of the modeling.

COMSOL Transient Model of BCM Experiments

Domain and Boundary Conditions

The transient COMSOL model of the BCM experiments uses 2D axial symmetry on a single domain 0.67 cm in radius by 10 cm in length. The value of the radius and the length are taken from BCM. The model uses the physical properties described in the material properties section, and assumes the same properties for the solid and the liquid phases. The model uses a heat transfer physics package, a moving mesh (ale) package, and a time dependent study step. The entire domain is set to an initial condition of 298 K.

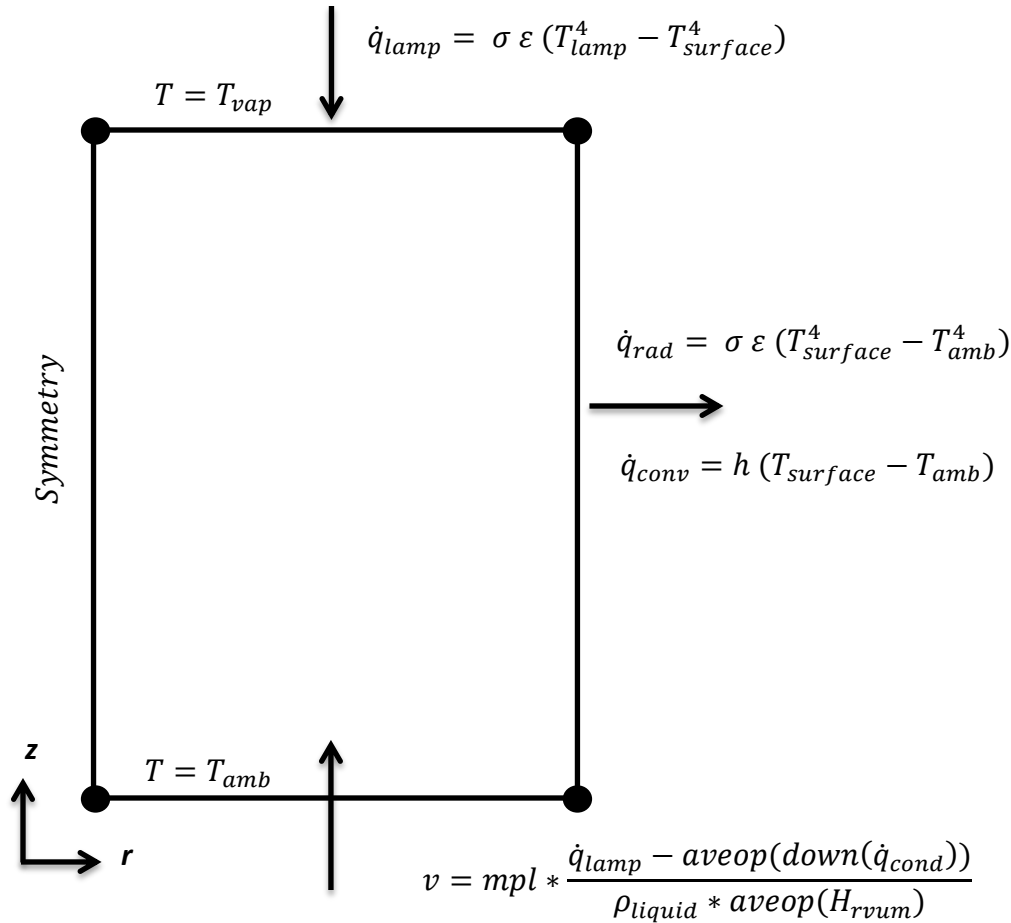


Figure 21: Transient BCM Model Diagram

The heat transfer package uses six separate boundary conditions (Figure 21). The left hand boundary, which is the center of the sample, uses an axial symmetry boundary condition. This means that the model mirrors the property and temperature values across the boundary, effectively acting as a zero flux boundary condition. The bottom boundary uses a temperature condition set to ambient, in this case 298 K. This requires that the boundary remains far enough away from the top boundary to not affect the heat transfer. Due to the material's low thermal conductivity, this requirement is easily met and must only be considered after very long run times. All runs were stopped well before this became an issue. The top boundary uses a combination of radiant heat flux and temperature conditions. The radiant flux condition is as described above. The temperature condition is set to freely increase as dictated by the heat transfer until a maximum temperature is reached. This temperature is the value at which 100

percent of the material has vaporized. The value used is 719 K for the reasons discussed in the material properties section. The right hand boundary, which is the outside surface of the sample, uses a combination of convection and radiation conditions. Both conditions require setting of an ambient temperature, used again is 298 K. The radiation condition uses the same emissivity as at the top, and the convection condition uses a heat transfer coefficient of 20 W/m²/K.

The moving mesh package uses four boundary conditions. At the top, it is specified that the boundary cannot move or deform in any way. At both the left and right sides, it is specified that the boundaries cannot move in the r direction but are free to move in the z direction. This means that all the boundaries can do is change their length. The top ends are set to not move because of the top boundary condition, so any changes in length can only occur through movement of the bottom ends. The bottom boundary is set to move at a specified velocity. This velocity is specified by the regression equation described below. Although the heat transfer occurs at the top of the domain, it was chosen to have the bottom boundary move so that the model more closely mirrored the experiments.

Regression Equation

The regression equation is a very important part of the model, and much thought and exploration was put into it. The equation is essentially the state-steady mass loss equation adapted to function within COMSOL.

$$v = mpl * \frac{\dot{q}_{lamp} - aveop(down)(\dot{q}_{cond})}{\rho_{liquid} * aveop(H_{rvum})}$$

The ρ_{Liquid} term is the density of the liquid polystyrene. The v term is simply the velocity of the regression boundary in m/s. The H_{rvum} term is the temperature dependent change in enthalpy term discussed in the material properties section. The other terms require more extensive explanation described below.

The numerator can be considered two terms, the heat into the boundary and the heat out of the boundary. The heat into the system is simply the radiant heat flux boundary

condition discussed above. Typically in a phase change problem the heat into and out of the transition boundary are defined as conduction flux terms. This model does not define or model the vapor/gaseous phase in any way, meaning the transition boundary is at the outside edge of the system. A boundary at the outside edge cannot have any conduction heat flux into it because there is nothing on that side of boundary to conduct. This leaves the radiation flux as the only alternative for defining the heat in term. A test was conducted to check validity of using the radiation flux. This test was performed by adding a thin highly conductive layer to the top of the existing domain. The radiation was then incident on the thin layer, and heat allowed to conduct into the transition boundary. No difference was found between the runs with or without the thin layer.

The heat out term is nothing but a conduction out term defined in a way that is useable in COMSOL. To get the correct conduction term, two prebuild COMSOL operators are needed. The first is the “down” operator. This operator takes the specified variable and calculates it at differential step down stream of the selected point. In the BCM model, this means that the “down” operator is going to a specific point on the top boundary, moving a differential step into the domain, and then calculating the conductive heat flux. If there was a domain on the other side of the transition boundary an “up” operator could be used to calculate the up stream conductive flux.

The other operator used in the regression equation is the “aveop” operator. This is an averaging operator that calculates the average value of a specified variable along a boundary or within a domain. With the “down” operator nested inside, the “aveop” operator is calculating the downstream conductive heat flux at every point along the top boundary and then averaging them into a single value. This averaged value then goes into calculating the regression rate. Use of the “aveop” operator solves two problems within the model. The first is that because the regression rate is calculated at the top boundary but applied to the bottom, some type of operator would be required for COMSOL to apply values from one point to another. The other problem it solves has to do with heat loss. Heat losses out of the right side of the domain cause radial dependent temperature profiles, which in turn means radial dependent conductive flux. Heat into the system is constant across the radius because of the radiant flux boundary

condition, but every point along the top boundary has a different value of down stream conductive flux. This would cause the boundary to regress at a different rate at every point, causing the boundary to bend or curve. This curving not only destroys the steady-state approximation of the system because it is constantly changing, it also does not accurately reflect the conditions of the experiments. In the experiments, the material becomes a liquid and the force of gravity keeps it more or less flat. Adding liquid and gravity dynamics to the model would greatly complicate it, and the averaging operation was considered a satisfactory approximation.

The *mpl*, mass percent loss, term is introduced to account for the vaporization occurring over a range of temperatures. The *mpl* is derived from the Netzsch TGA data. The data was flipped from mass percent remaining to mass percent loss. It was then set to be identically zero below the vaporization range and identically one above the vaporization range (Figure 22).

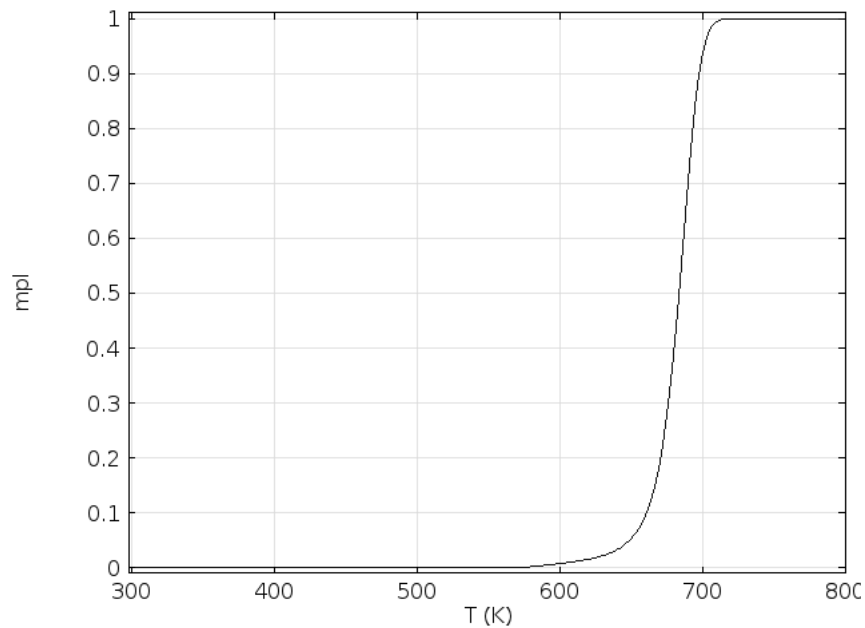


Figure 22: Dense Polystyrene Mass Percent Loss (*mpl*)

It is used to scale the regression rate by limiting the amount of mass that can vaporize at any given temperature. For example, at 650 K the *mpl* is 0.055 and the H is 1070 J/g. This means that only 5.5% of the mass vaporizes at a regression rate determined by an H of 1070. This

causes the regression rate to start at zero and build to its maximum value at the pseudo steady-state.

COMSOL Steady-State Model of BCM Experiments

Domain and Boundary Conditions

The steady-state COMSOL model of the BCM experiments uses 2D axial symmetry on a single domain 0.67 cm in radius by 10 cm in length. The value of radius is taken from BCM. The length of the domain is not important as long as the bottom boundary is far enough away from the top to not affect the heat transfer. Several lengths were tested and 10 cm is well beyond this limit. The model uses the physical properties described in the material properties section, and assumes no distinction between a solid and liquid phase. The model uses a heat transfer in fluids physics package and a stationary study step.

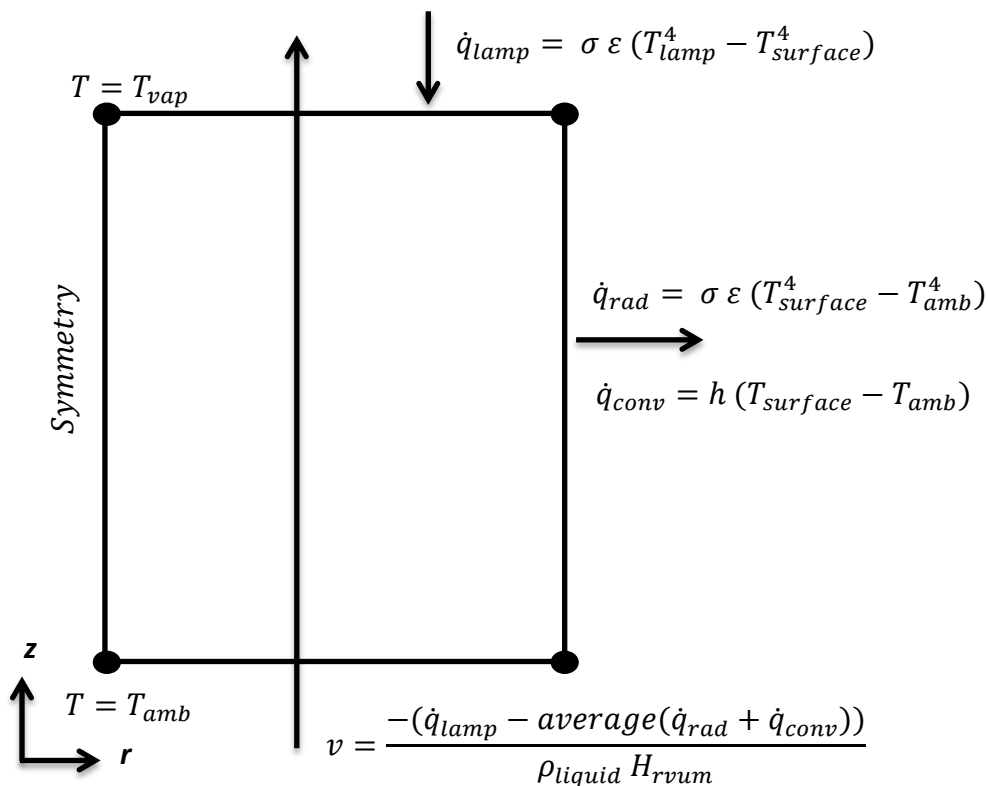


Figure 23: Steady-State BCM Model Diagram

The heat transfer package allows for the flow of material through the domain and across the boundaries. This flow represents the vaporization of the material. The model can be thought of as a stationary window on an infinitely long sample rod, where material leaves the window by vaporization and is carried in by a matching flow rate. Material flows into the bottom domain carrying energy in with it, and flows out the top taking energy with it. The fluid mechanics involved are simplified so that any velocity profile must be supplied. This model uses a single, flat velocity profile across the entire domain described by a single value. This matches the experiments well where a solid material is driven by a flat profile with negligible wall friction. The single velocity value used in the model is the regression velocity describe below.

The heat transfer package uses six separate boundary conditions along with the flow condition (Figure 23). The left hand boundary, which is the center of the sample, uses an axial symmetry boundary condition. This means that the model mirrors the property and temperature values across the boundary, effectively acting as a zero flux boundary condition. The bottom boundary uses a temperature condition set to ambient, in this case 298 K, which also sets the temperature of all inflowing material. The top boundary uses a combination of radiant heat flux and temperature conditions. The radiant flux condition is as described above. The temperature condition is set to the temperature at which 100 percent of the material has vaporized. The value used is 719 K for the reasons discussed in the material properties section. The right hand boundary, which is the outside surface of the sample, uses a combination of convection and radiation conditions. Both conditions require setting of an ambient temperature, used again is 298 degrees K. The radiation condition uses the same emissivity as at the top, and the convection condition uses a heat transfer coefficient varied from 5 to 20 W/m²/K.

Regression Equation

The regression equation for the steady-state BCM model is almost identical to the one used in the transient model described above with two small changes.

$$v = \frac{\dot{q}_{lamp} - aveop(down(\dot{q}_{cond}))}{\rho_{liquid} * H_{rvum}}$$

First, the mpl term is removed. Second, the H_{rvum} term is no longer temperature dependent. Both changes are because this model is entirely in the steady-state regime with no heat up phase. This means both the mpl and the H_{rvum} term are set to their 719 K values of 1 and 1980 J/g respectively.

COMSOL Model of Butler Foam Experiments

Domain and Boundary Conditions

The COMSOL model of the Butler experiments uses 2D axial symmetry with two domains. The first domain is initially 0.56 cm in radius and 14.9 cm in length. This domain uses the foam properties described in the material properties section and will be referred to as the foam domain. The second domain is initially 0.56 cm in radius, 0.1 cm in length, and located directly on top of the first domain (Figure 24).

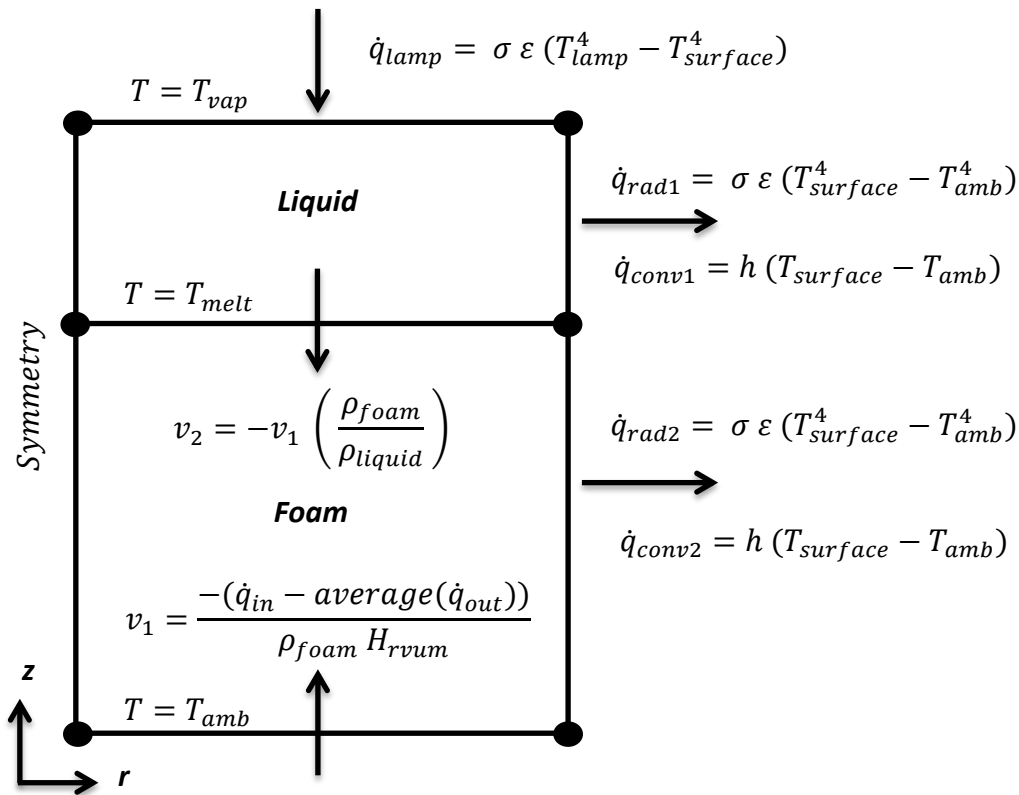


Figure 24: Butler Model Diagram

This thin domain uses the same solid material properties used in the BCM models, and will be referred to as the liquid domain. The overall system is 0.56 cm in radius by 15 cm in length, the dimensions of Butlers foam experimental samples. Unlike in the BCM model, this model makes a distinction between the solid and the liquid phases. It uses two heat transfer physics packages, a moving mesh package, and two time dependent study steps. The first step uses only the first heat transfer package and is used to model the heat up of the sample from ambient conditions before any regression occurs. The second study step uses the other heat transfer package and the moving mesh package and models the regression process. A different heat transfer package is needed for each study step because the boundary conditions change between the heat-up and regression phases. Specifics on the heat-up phase and why it is constructed the way it is will be discussed later, the following will describe only the regression phase.

The top boundary, which is the top of the liquid domain, uses the radiation boundary condition described above, along with a temperature boundary condition. The temperature condition uses the range of values discussed in the material properties section, 640 K to 670 K. The left hand side of the model uses the symmetry boundary condition in both domains. The right hand side uses convection and radiation conditions in both domains with an ambient temperature of 298 K. The bottom of the system uses a temperature condition of 298 K. The boundary between the foam and liquid phases uses another temperature condition, which reflects the temperature at which the foam melts/collapses. A value of 373 K is used, based on the Netzsch data and the literature.

The moving mesh physics uses two different boundary conditions, displacement and velocity. The top boundary is stationary. The sides are set to not displace in the r direction but allowed to freely displace in the z direction. The bottom boundary and the liquid/foam interface boundary are set to move with a prescribed velocity. Overall, this means that the top boundary remains completely stationary while the sides change length in accordance with the prescribed velocities. The velocity of the bottom boundary is specified by the regression

equation discussed later. The interface boundary velocity is coupled to the regression velocity through a mass balance across the boundary:

$$\dot{m}_{out} = v_{liquid} * \rho_{liquid} = v_{regression} * \rho_{foam} = \dot{m}_{in}$$

Solving for the liquid velocity:

$$v_{liquid} = v_{regression} * \frac{\rho_{foam}}{\rho_{liquid}}$$

The interface boundary simply moves at a scaled value of the regression boundary, where the scaling factor is the foam to liquid density ratio.

Regression Equation

The regression equation is the steady state mass loss equation adapted for use in COMSOL. The form of the equation for the Butler model is very similar to the one for the BCM models, but with a different heat-out term.

$$v = \frac{\dot{q}_{lamp} - [aveop(\dot{q}_{rad1}) + aveop(\dot{q}_{conv1}) + aveop(down(\dot{q}_{cond}))]}{\rho_{foam} H_{rvum}}$$

The heat-in term is subject to the same restrictions discussed in the BCM model, and once again the radiation flux is used. As with the transient BCM model, the Butler model was run with a thin conductive layer on top of the liquid domain to check the use of the radiation boundary flux. The change in enthalpy term corresponds to the H_{rvum} discussed in the material properties section. This model requires two densities and the appropriate one must be chosen for use in the regression equation. Looking back at the steady-state analysis, the foam material mass loss is:

$$\dot{m} = \rho_{in} * v_{in} = \rho_{out} * v_{out}$$

Two velocities are defined, one for each density, but only one is of interest for the model. As discussed in the review of the BCM and Butler experiments, the v_{in} term corresponds to the velocity of the syringe pump. This velocity is identical to the regression velocity, making it and its associated ρ_{in} the appropriate values. For this model the ρ_{in} is that of the foam material, 26.5 kg/m³.

Due to the added complexity of the foam model, the heat out term had to be changed from that used in the BCM models. The added temperature constraint at the liquid/foam interface sets the temperature profiles in the liquid domain. With a temperature constraint at each end of the domain, the profiles, and the downstream average heat conduction term, become independent of the applied radiant heat flux. This issue required the defining of a new heat out term. The bracketed term above is the heat-out term. It is the sum of three different heat loss values. The first two terms are the average convection and radiation fluxes out of the liquid layer. The third term is the average downstream conduction flux from the foam/liquid interface into the foam. Again, an averaging operator is required to tie the other boundaries to the bottom boundary where the regression equation is applied.

Model Initialization

As stated earlier, the model uses two time dependent study steps. The first step is used to set up initial conditions for the second study step which calculates the regression. Without approximate initial conditions, the moving mesh physics will not function in the desired way. If the second study step was started with a constant 298 K throughout, the boundary could move orders of magnitude too fast, in the wrong direction or both. This initial jump in the regression rate often causes the model to fail to converge or to converge on a solution other than the one trying to be described.

The first step starts with an initial condition of 298 K throughout. It uses the same boundary conditions at the bottom and left side as in the second study step. The top and liquid/foam interface boundaries no longer have a temperature condition. The top boundary still uses the same radiation condition. The right boundary conditions are changed to thermal insulation. Heat loss is eliminated from the right side boundary so that the temperature profiles

are flat and the liquid/foam interface boundary reaches 373 K at a single time. When this occurs, the study step is stopped. This stop time is achieved through a trial and error process. The boundary conditions in this step do not adequately model the heat up phase of the experiments. They are only used to create reasonable temperature profiles to initialize study step two.

Sandia Model

The Sandia model uses four heat transfer in solids physics packages and one moving mesh physics package on a one dimensional domain set by the dimensions of the Sandia experiments. It uses four different study steps, three time dependent and one stationary. Figure 25 illustrates the materials and dimensions of the model.

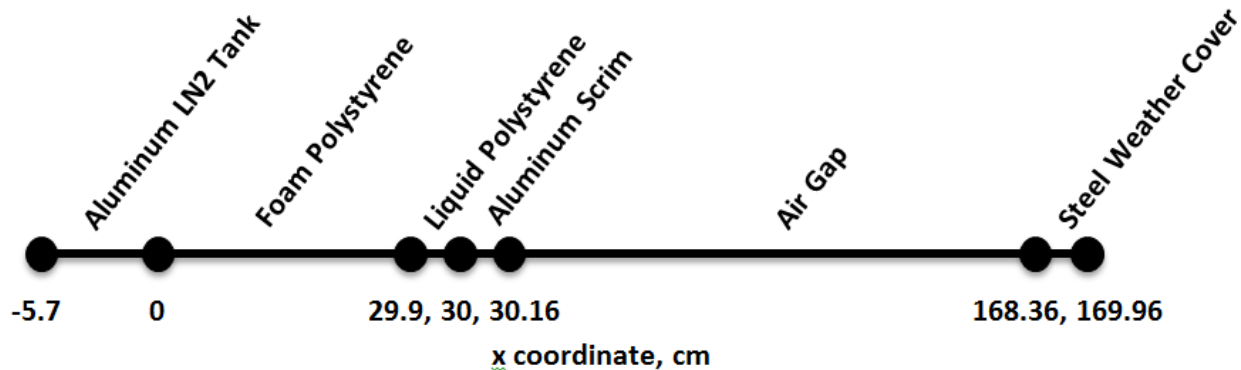


Figure 25: Sandia Model Diagram

The material properties of the aluminum, steel, and air are taken from COMSOL’s built in data. The polystyrene foam and liquid properties are the same values used in the Butler model. The emissivity of steel is set to 0.7 as specified in the Sandia report. The aluminum emissivity was investigated over a range of 0.02 to 0.2.

The model is split into four phases. The first phase uses one heat transfer package and the stationary study step. It models the initial steady-state conditions of the experiment where the LN2 tank is brought into contact with the system and allowed to reach equilibrium before

the radiative heating begins. This was modeled by simply setting the temperature boundary at each end of the system, one at LN2 and one at ambient.

The second phase models the heat up of the system after the heating lights are turned on and stops just before the polystyrene starts to regress. It uses the second heat transfer physics package and the first of the time dependent study steps. It is stopped when the boundary between the aluminum scrim and the polystyrene reaches the maximum vaporization temperature. A temperature value of 670 K was used from the range explored in the Butler model. The stop time must be determined by trial and error. It uses the temperature results from phase one as its initial conditions. It uses the same LN2 temperature boundary condition of the first phase, but it replaces the ambient temperature condition with a radiation one to model the heating lamps. Only one incident flux value was investigated for this model. Sandia's experiments were only run at an incident flux of 270 kW/m^2 . Phase two also adds two surface to surface radiation boundary conditions. These are located at each end of the air domain and allow radiation heat transfer from the steel weather cover to the aluminum scrim. This phase is only approximate in that it allows the polystyrene to reach its maximum temperature before regression occurs. In the experiment, regression begins when the foam reaches its melting temperature of 373 K. This approximation is necessary to smooth the transition from phase two into phase three.

The third phase models the regression. It uses the third heat transfer physics, the moving mesh physics, and the second time dependent study step. It uses all the boundary conditions from phase two and adds two temperature conditions. A temperature condition is added to the liquid/ aluminum scrim interface, set to a maximum vaporization temperature. The same range of 640 to 670 K used in the Butler model was also explored in this model. The other added condition sets the temperature at the foam/ liquid interface to the melting temperature, 373 K. It uses the final temperature profile from phase two as its initial condition. It is stopped when the boundary between the foam and the liquid polystyrene reaches the boundary between the aluminum LN2 and the foam. This is the point at which the foam domain has disappeared, meaning it has all melted and turned into liquid. As with phase two, this stop time must be determined by trial and error.

The regression in phase three involves three moving boundaries. The foam/liquid interface moves at a velocity prescribed by the regression rate equation.

$$v = \frac{(aveop(up(\dot{q}_{cond})) - aveop(down(\dot{q}_{cond})))}{\rho_{foam}H_{rvum}}$$

The overall regression equation is similar to equation from the Butler model but with the radiation and convection heat loss terms removed and a different heat-in term. As this is a one dimensional model, there are no lateral heat losses. The regression boundary is also no longer an outside boundary and a traditional conduction term can be used for the heat-in. This simplifies the numerator of the equation to the conduction into the liquid domain from the aluminum scrim minus the conduction out of the liquid domain into the foam.

The liquid/ aluminum scrim interface moves at a velocity determined by the overall regression rate and the mass balance between foam and solid. As in the Butler model, it simplifies to the overall regression rate scaled by the density ratio of foam the dense polystyrene.

$$v_{liquid} = v_{regression} * (1 - \frac{\rho_{foam}}{\rho_{liquid}})$$

The aluminum scrim/ air interface moves at the same velocity as the liquid/ aluminum scrim interface. This is to keep the aluminum scrim domain the same thickness at all times as it moves along with the regressing polystyrene.

Phase four models what happens to the system after the polystyrene is gone. It uses the last heat transfer physics package and the final time dependent study step. This step runs for ten minutes. It uses the final temperature profile and boundary positions from phase three as its initial conditions. The boundary conditions are very similar to those from phase two. There are two surface to surface radiation conditions to allow radiation transfer between the weather cover and the aluminum scrim. However, the scrim is now in direct contact with the LN2 tank. Added to the range of 0.02 to 0.2 for emissivity, a new value of 0.8 is explored. This value is

used to model what would happen if the aluminum scrim failed or became soot covered when the polystyrene disappears. The regression has finished and all of the boundaries are stationary during this step. The two internal temperature boundary conditions associated with the polystyrene are also removed for this step. The liquid and foam domains are gone leaving only the aluminum domain at one end, the steel domain at the other, and the air or N₂ in between.

The right end of the domain uses a radiation to ambient boundary condition. For this phase, two different temperature values were used. The first temperature used was the same value used in steps two and three which models the 270 kW/m² heat flux of the lamps. This simulates what would happen if the heating lamps were left on after the regression was completed. The other temperature value used was 298 K. This simulates what would happen if the heating lamps were turned off after the regression was completed and the system was allowed to cool.

The left end of the domain uses two different boundary conditions. The first condition is the temperature condition of LN₂ used in all the other steps. The second condition is a convective boundary condition. This condition requires the setting of a bulk fluid temperature and a heat transfer coefficient. The LN₂ temperature is used for the bulk temperature value. A heat transfer coefficient of 200 W/m²K is used. Heat transfer coefficients for film boiling in LN₂ vary over a large range and are dependent on many variables, such as geometry and system pressure. The 200 W/m²K value was chosen from literature as a representative value for film boiling in LN₂ under atmospheric pressure [19]. This condition is explored because the assumed constant temperature condition may not hold after the insulation is gone and the resulting thermal front contacts the tank wall. It is possible that the thermal front heats the wall enough to create a large amount of vapor. This large amount of vapor causes a persistent layer of vapor to develop between the wall and the bulk fluid. This persistent vapor layer is best modeled by convective heat transfer.

The different boundary conditions used on the left and right ends were combined with the range of emissivities in ways to explore their individual and cumulative effects.

Results and Discussion

BCM Models

The primary value of interest from the BCM models is the pseudo steady-state regression rate as a function of incident heat flux. This value can be directly compared to the regression rates and incident fluxes measured by BCM.

Figure 26 illustrates a typical temperature profile for both of the BCM models. The temperature contours start at 300 K around a z coordinate of 8cm, and then increase by steps of 20 K to 700 K located just below the top surface.

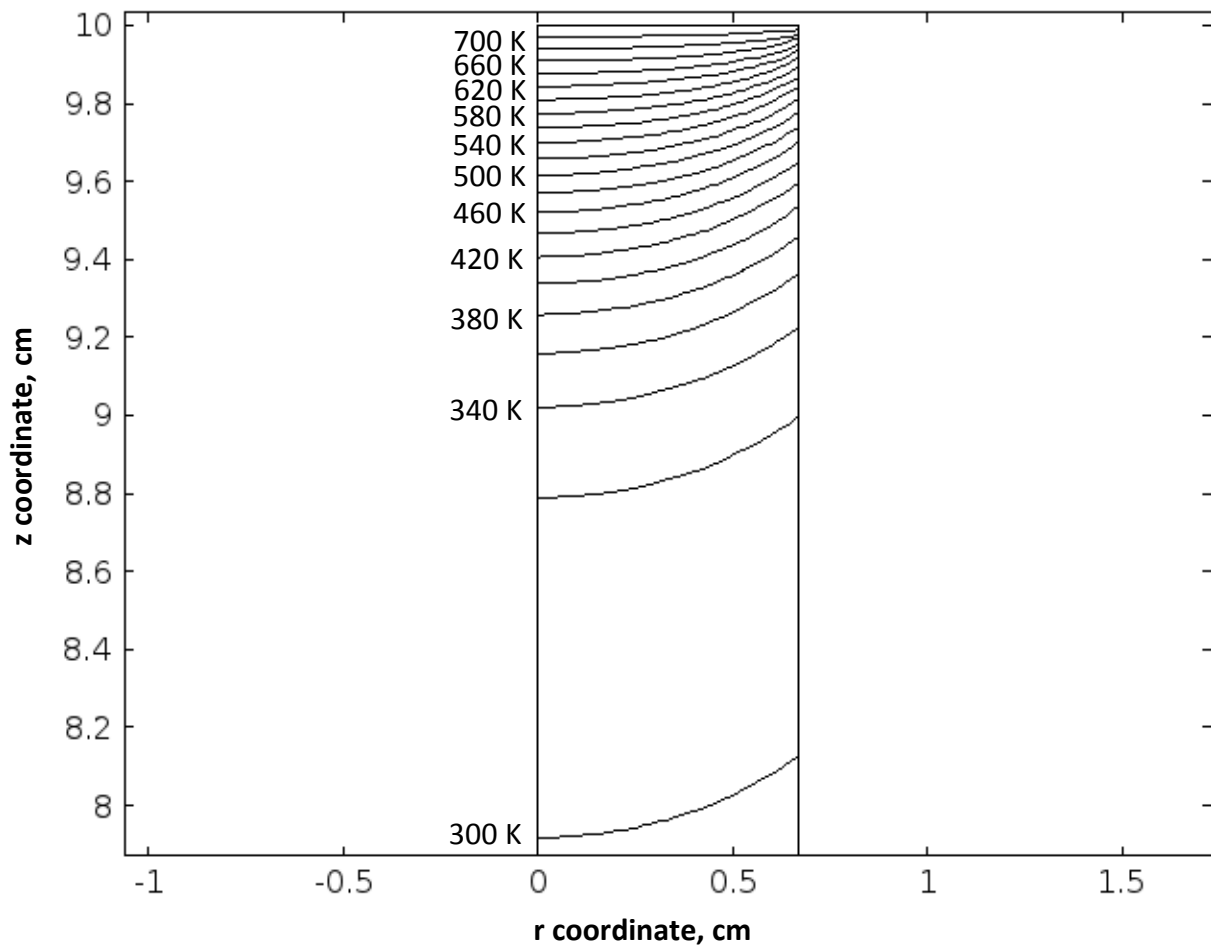


Figure 26: BCM Models Example Temperature Profiles

The effects of heat loss can be observed as the contours curve up on the right side of the plot, which is the outside edge of the material. The majority of the heat only penetrates into the material about one or two cm for all fluxes examined.

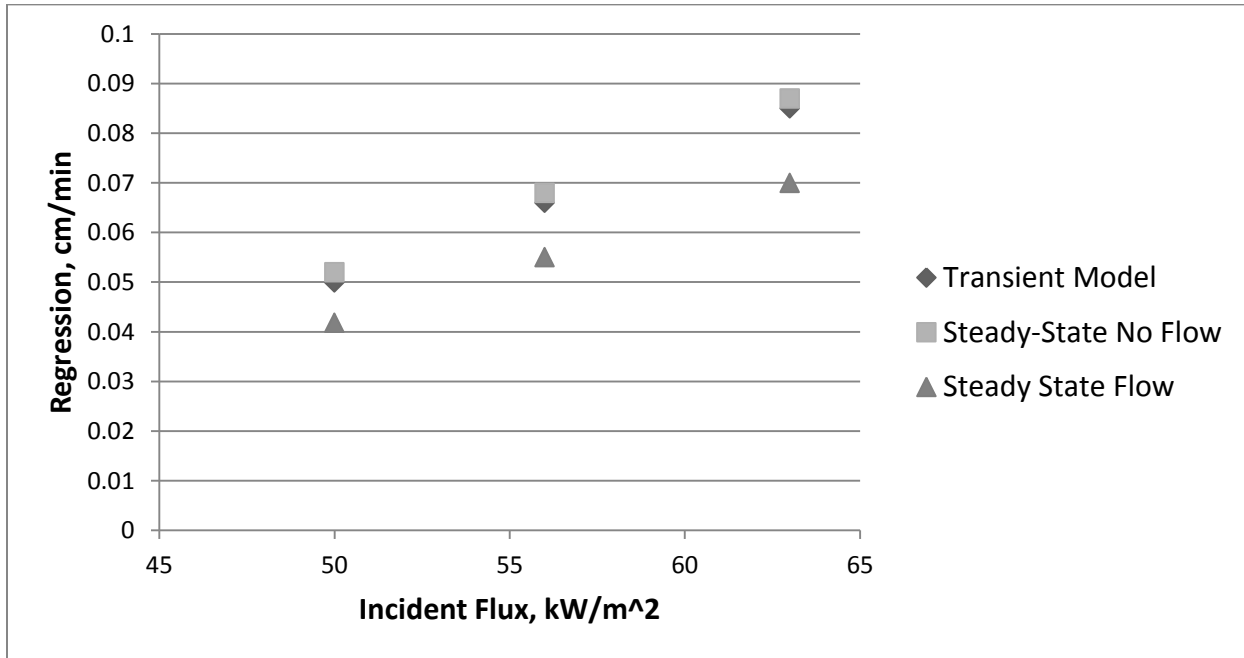


Figure 27: Transient vs Steady-State BCM Models Comparison

Figure 27 shows the comparison between the transient and steady-state models for a given set of material property values. The steady-state model has significantly lower regression rates than the transient model across all three fluxes investigated. It was found that the temperature profiles for the steady-state model did not penetrate as far into the material as in the transient model. This decreased penetration results in a larger heat-out term in the regression equation, and with all other values equal, results in a smaller regression rate. It is believed that this change in penetrated depth is due to the different physics used in the steady-state model, as mentioned in the model descriptions. The transient model uses the moving mesh physics to model regression. The moving mesh physics essentially chops off bits of the domain while the material itself is completely stationary. The steady-state model uses actual material flow through the domain to model the regression with the heat transfer in fluids physics package. The flowing material in the steady-state model carries heat with it. The

material flows upward, carrying heat upward, and decreases the penetration depth. To test this idea, the steady-state model was run with a velocity of zero or no flow. After the simulation was complete the regression rate equation was used to calculate what the rate would have been for the heat transfer described by the no flow solution. These values are plotted in figure 16, and it can be seen that removing the flow physics significantly change the results. The no flow results are also in close agreement with the transient model results. Although other effects that may contribute to differences between the two models include, the results show that the difference is mostly explained by the effect of material flow. An attempt was made to create a transient model with material flow, but the problem appeared to be too highly nonlinear for COMSOL to solve. It was then decided to proceed with a detailed variable analysis only with the steady-state model. Although all modeling of the heat up phase was lost, more accurate modeling of the pseudo steady-state regime was decided to be of more importance. The pseudo steady-state regime comprises most of the experimental run times and the pseudo steady-state regression rate is of the most interest.

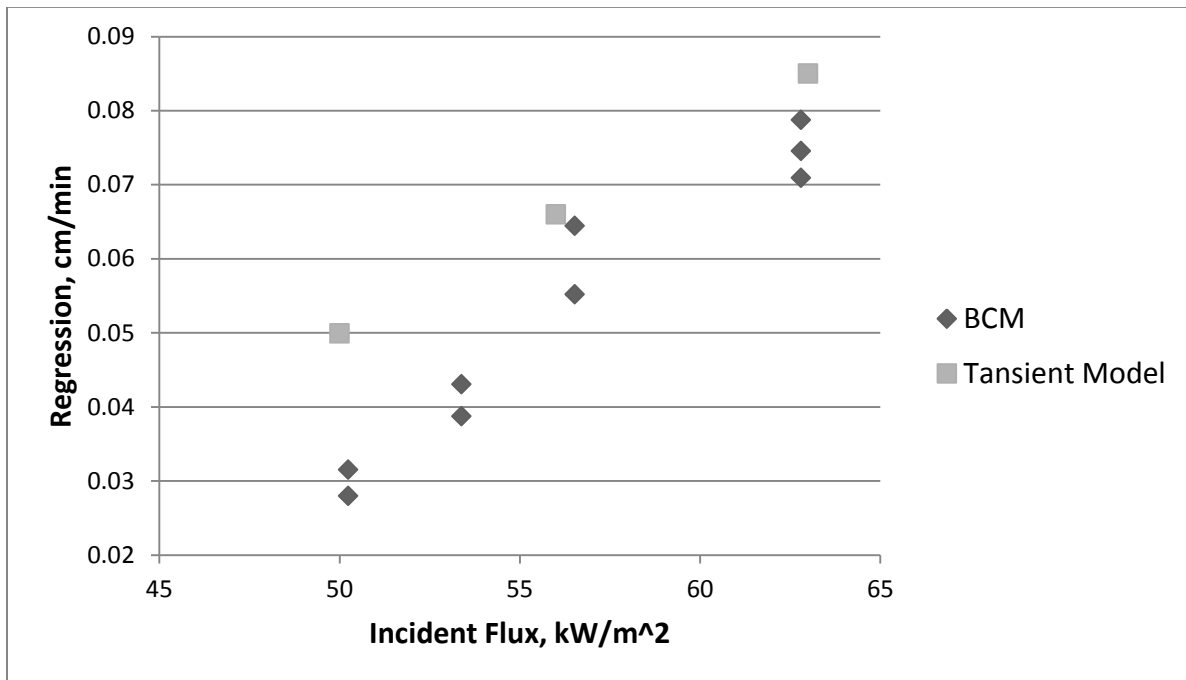


Figure 28: Transient BCM Model vs BCM Data Over Full Flux Range

Another point examined with the steady-state model before a detailed variable analysis was the range of incident fluxes to be evaluated. Looking at the BCM data (Figure 28), a good linear fit can be achieved. However, a good curved fit can also be obtained. The COMSOL model results are always almost perfectly linear and have always had much better agreement at 56 and 63 kW/m² than at 50 or 54 kW/m². Whether this is a problem with nonlinearity in the BCM data or a problem with the model at low fluxes is unclear. Whatever the cause, it was decided to only perform a detailed variable analysis across an incident flux range of 56 to 63 kW/m².

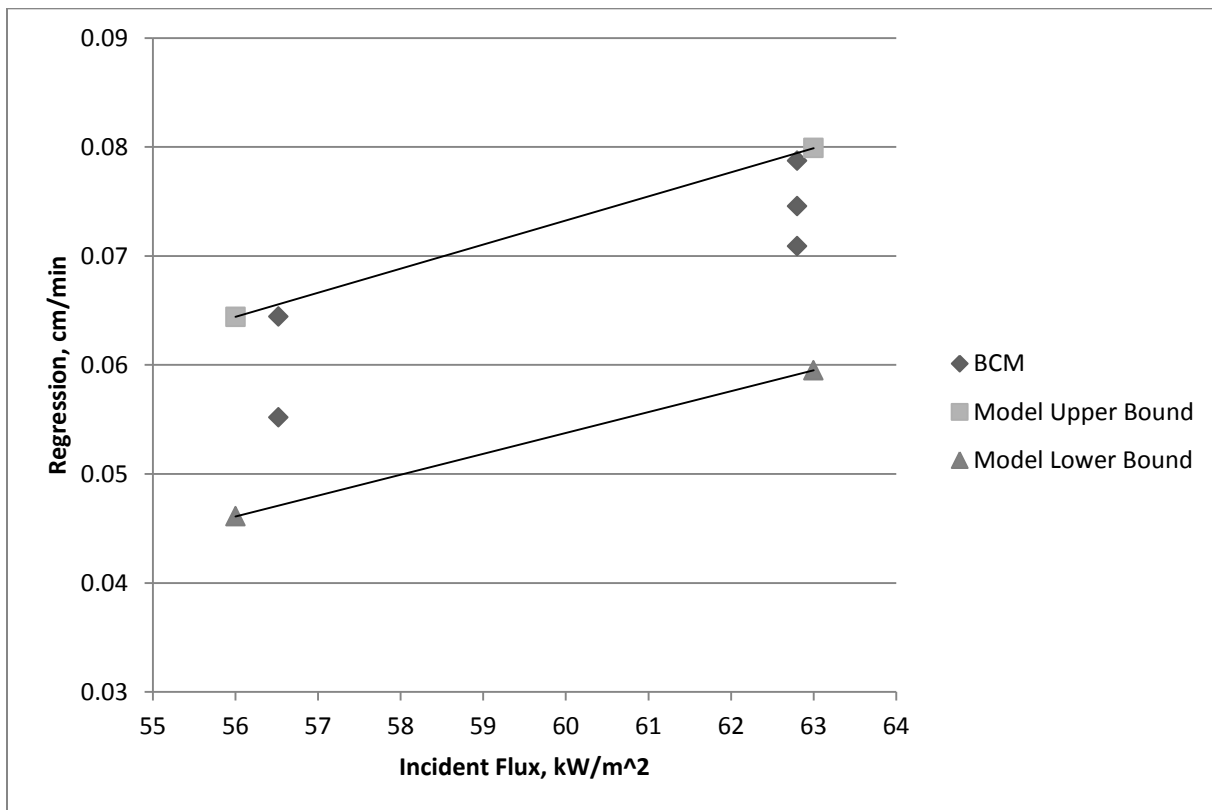


Figure 29: Steady-State BCM Model Results

Figure 29 shows the results of the detailed variable analysis done with the steady-state model investigation. As discussed in the previous sections, there is important uncertainty in the

values of emissivity and convective heat transfer coefficient. A range of 0.85 to 1 for emissivity, and 5 to 20 W/m²/K for transfer coefficient were tested. Increasing the emissivity increased the heat-in term and to a smaller degree the heat-out term. This netted a higher regression rate overall. Increasing the transfer coefficient increased the heat out term only, netting an overall lower regression rate. Pairing an emissivity of one and a transfer coefficient of 5, a model maximum regression rate was calculated for all fluxes. Similarly, an emissivity of 0.85 and a transfer coefficient of 20 created a model minimum regression rate. These results are plotted in Figure 29 as the bounds for all possible model solutions. It can be seen that all of the BCM experimental data falls within the bounds of the model. Table 1 shows the results for the complete list of runs performed with the Steady-State model.

Table 1: Steady-State BCM Model Results

Flux, kW/m ²	h, W/m ² /K	emissivity	Regression, cm/min
63	10	1	0.078
56	10	1	0.0624
63	10	0.85	0.063
56	10	0.85	0.0496
63	20	0.95	0.0697
56	20	0.95	0.0548
63	5	0.95	0.075
56	5	0.95	0.0602
63	5	1	0.0799
56	5	1	0.0644
63	20	0.85	0.0595
56	20	0.85	0.0461

Butler Model

As with the BCM model, the value of most interest from the Butler model is the regression rate as a function of incident heat flux. The value can be compared directly to values measured in the Butler experiments. All of the runs performed with the Butler model have a run time of 210 s. During the variable analysis, this run time was found to be long enough for all runs to reach the pseudo steady-state regime while also short enough to prevent the fast regression rate runs progressing too far. If the model progresses too far, the ambient temperature boundary condition applied at the bottom of the system will start to affect the heat transfer at the top of the system.

As mentioned in the model description, the effect of material flow that caused a noticeable difference between the BCM models is negligible in the Butler model. The regression in the solid material is driven entirely by vaporization, whereas the foam regression is a combination of vaporization and collapse. The effect of flowing material observed in the BCM models only affects the vaporization portion of the overall regression rate. The foam material can be accurately modeled as stationary because it does not flow out of the system but instead transforms into liquid. The foam collapses at a much greater rate than the liquid vaporizes, and any error in modeling the vaporization has a negligible effect on the overall regression rate.

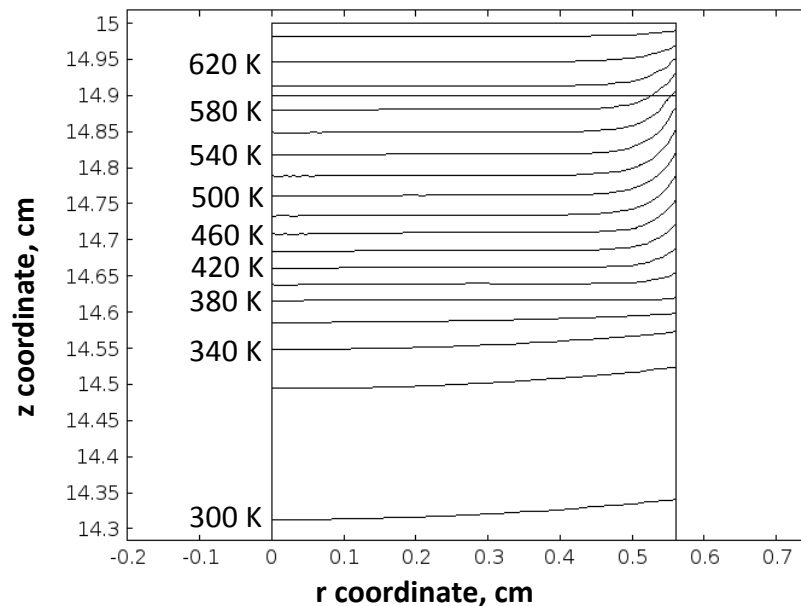


Figure 30: Butler Model Example Temperature Profiles

Figure 30 illustrates a typical temperature profile for the Butler model at a given time. The time used was taken from near the end of the model run to reflect the pseudo steady-state regime. The temperature contours start at 300 K around a z coordinate of 14.3 cm, and then increase by steps of 20 K to 640 K located just below the top surface. As with the BCM models, heat losses cause the profiles to curve up on the right or outside edge of the system. As described in the model description, the moving boundaries are forced to remain flat, this causes the temperature contours to flatten around the liquid/foam interface boundary set at 373 K. This can be seen by the two near flat contours around the z coordinate of 14.6 cm. A perfectly flat line can be seen at a z coordinate of 14.9 cm. This is not a temperature contour but the initial position of the foam/liquid interface boundary. It is an artifact from how COMSOL generates plots and can be ignored. Due to the lower thermal conductivity of the foam compared to the dense material, the temperature penetration depth is less in the Butler model. It is often less than one cm, compared to one to two cm in the dense material.

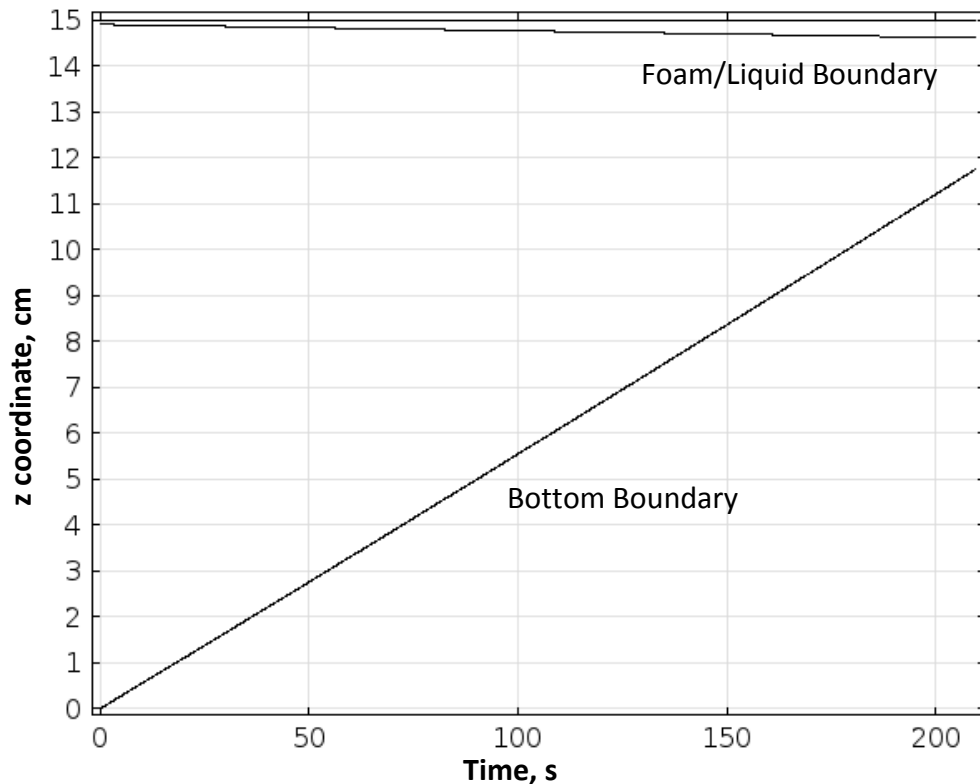


Figure 31: Butler Model Example Regression

Figure 31 is a typical example of the model boundary position as a function of time. The bottom boundary, which models the overall regression rate, can be seen moving upward at a relatively fast and constant rate. The middle boundary moves downward simulating the growing liquid layer. The top boundary remains stationary at 15 cm but was plotted to help illustrate the movement of the middle boundary.

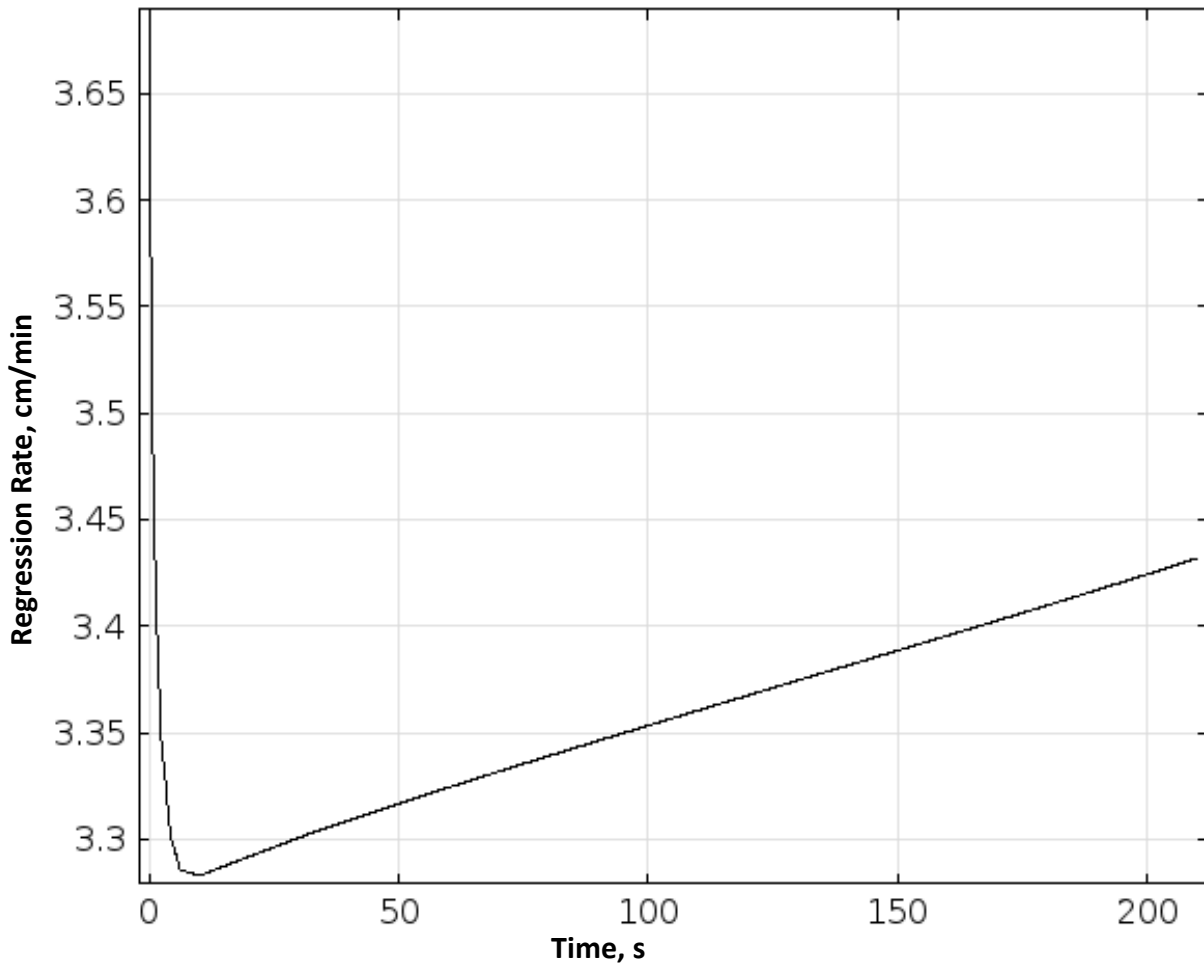


Figure 32: Butler Model Example Regression Rate

Figure 32 is a typical example of the regression rate as a function of time. The initially segment that starts high and rapidly falls can be ignored. It is a result of the approximate temperature profiles created in the heat-up phase of the first study step. The imperfect profiles

used as the initial values for the second study step cause a slight jump in the boundary velocity as the second study step settles into the correct profiles. It occurs over only a few seconds and has no significant effect on the final results. It affects the final position of the moving boundaries but not their velocities during the pseudo steady-state regime. The second section of the plot is of importance. It is the regression rate during the pseudo steady-state phase. As expected, the foam problem is less compatible with the pseudo steady-state assumption than the dense material. The added complexity of a growing liquid layer and the shorter run times cause the regression velocity to not be constant. The degree to which the regression velocity varies with time is dependent on the incident flux used. At higher fluxes the velocity changes at a slower rate. In all cases, the regression velocity does not change more than a few percent over the run time of the model. It is unknown if this slow rise in regression rate was present in Butler's experiments. It is likely that if the velocity did vary with time, it was too small to measure with his instruments. Due to the time varying regression rate, an average value was used in the flowing comparison to experiment.

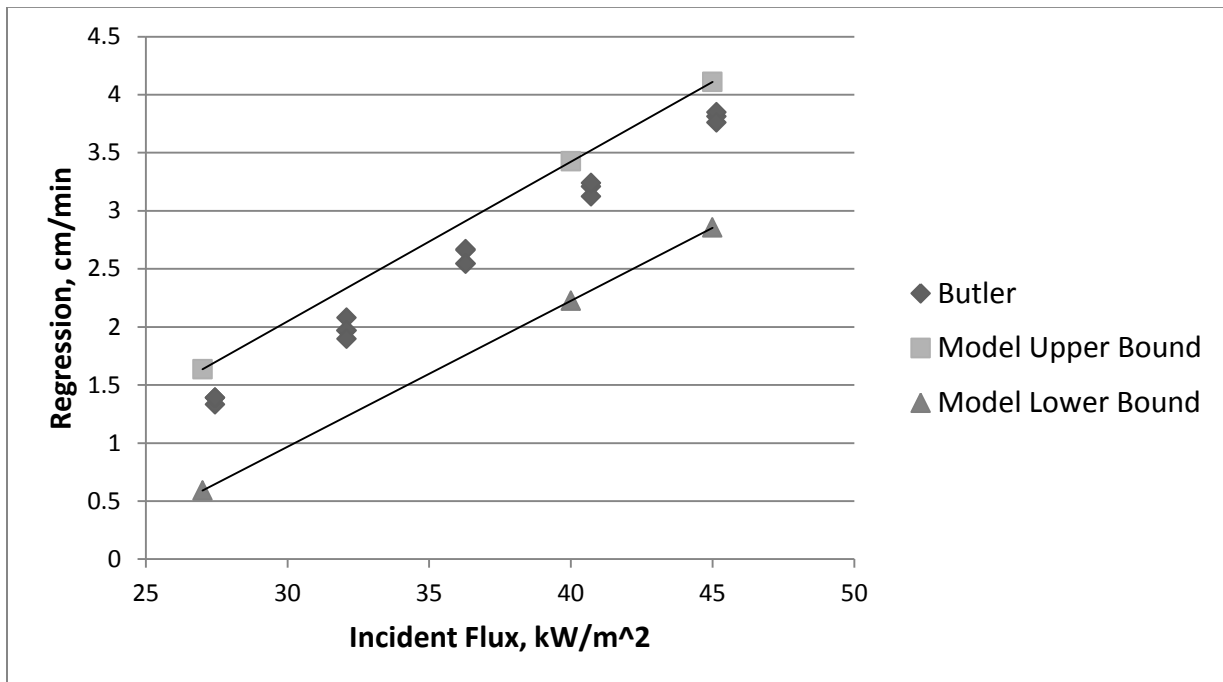


Figure 33: Butler Model Results

Figure 33 shows the final results of the Butler Model. Unlike with the BCM model, the Butler model was compared across the entire experimental range of incident heat flux values. As seen in Figure 33, Butler’s experimental data appears very linear across the entire flux range. As with the steady-state BCM model, the Butler model was run for a range of property values leading to an upper and lower bound. The upper bound was created using an emissivity of 0.95, a convection heat transfer coefficient of 5 W/m²/K, a foam thermal conductivity of 0.021 W/m/K, and a maximum vaporization temperature of 640 K. The lower bound used respectively 0.85, 20, 0.034, and 670. All of Butler’s data falls within these bounds. Table 2 shows the results for the full set of runs made with the Butler model.

Table 2: Butler Model Results

Flux, kW/m ²	h, W/m ² /K	e	T _{vap} , K	k, W/m/K	Regression, cm/min
27	10	1	650	0.021	1.465
40	10	1	650	0.021	3.355
45	10	1	650	0.021	4.09
27	10	0.8	650	0.021	1.08
40	10	0.8	650	0.021	2.59
45	10	0.8	650	0.021	3.17
27	20	0.9	650	0.021	0.98
40	20	0.9	650	0.021	2.7
45	20	0.9	650	0.021	3.36
27	5	0.9	650	0.021	1.425
40	5	0.9	650	0.021	3.12
45	5	0.9	650	0.021	3.77
27	10	0.9	670	0.021	1.025
40	10	0.9	670	0.021	2.73
45	10	0.9	670	0.021	3.385
27	10	0.9	640	0.021	1.39
40	10	0.9	640	0.021	3.09
45	10	0.9	640	0.021	3.74

Table 2: Butler Model Results (cont)

Flux, kW/m ²	h, W/m ² /K	e	T _{vap} , K	k, W/m/K	Regression, cm/min
27	10	0.9	650	0.021	1.275
40	10	0.9	650	0.021	2.97
45	10	0.9	650	0.021	3.63
27	10	0.9	650	0.034	1.25
40	10	0.9	650	0.034	2.945
45	10	0.9	650	0.034	3.61
27	10	0.95	650	0.021	1.34
40	10	0.95	650	0.021	3.14
45	10	0.95	650	0.021	3.84
27	5	0.95	640	0.021	1.635
40	5	0.95	640	0.021	3.425
45	5	0.95	640	0.021	4.11
27	20	0.85	670	0.034	0.59
40	20	0.85	670	0.034	2.225
45	20	0.85	670	0.034	2.855

Sandia Model

The values of interest in the Sandia model differ from those of the BCM and Butler models. The rate of the regression is of less importance, and the total time required to complete regression is of more importance. This value reflects the time required for the insulation system to fail. Also of great interest is the heat flux rate into the LN2 tank through the entire model run. This flux directly relates to the rate of LN2 that would boil off during experiment.

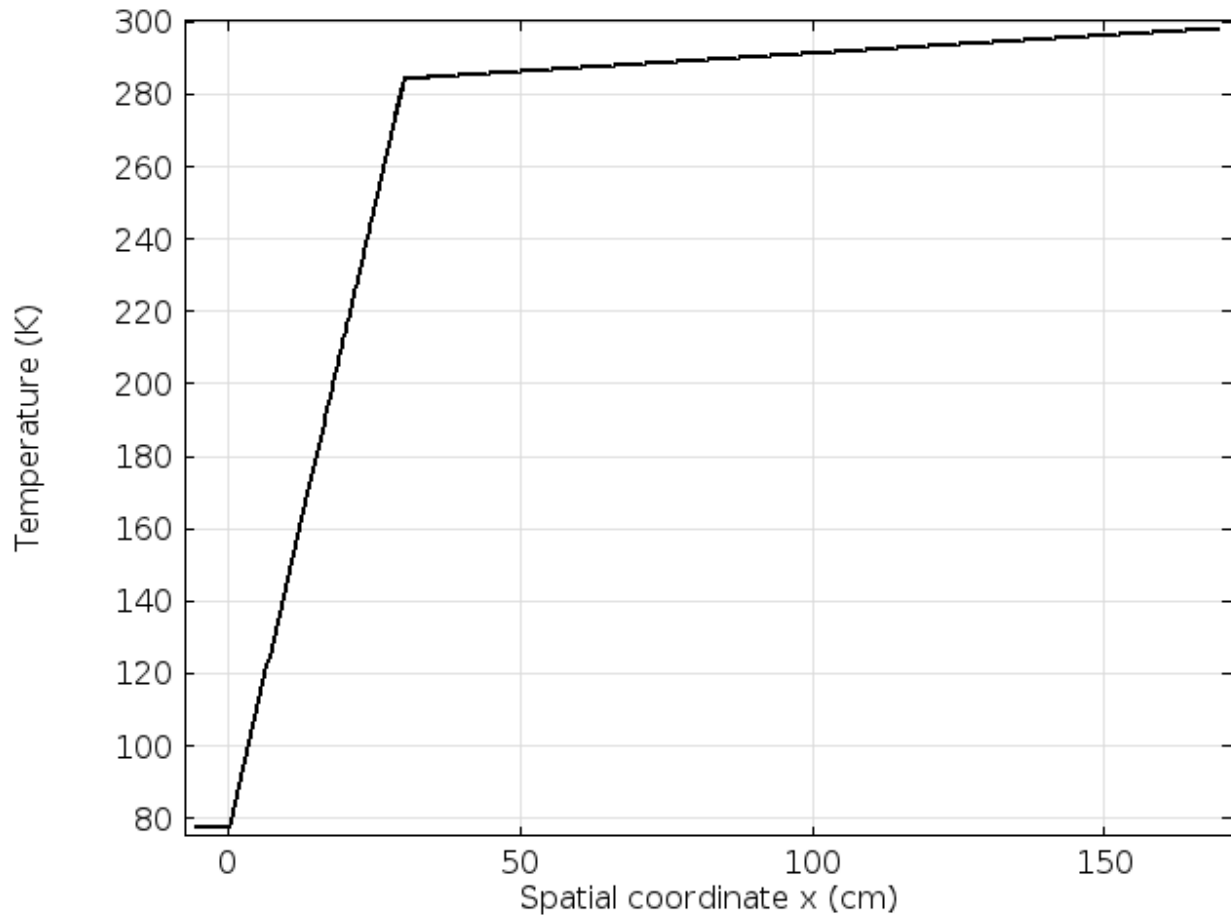


Figure 34: Sandia Model Step One Temperature Profile

Figure 34 illustrates the temperature profile for the first step of the Sandia model. This is the steady-state step that occurs before the heating lamps are turned on. The short flat section on the left is the aluminum LN2 tank wall. The steep profile in the middle is the foam section. The flatter section to the right is the air gap.

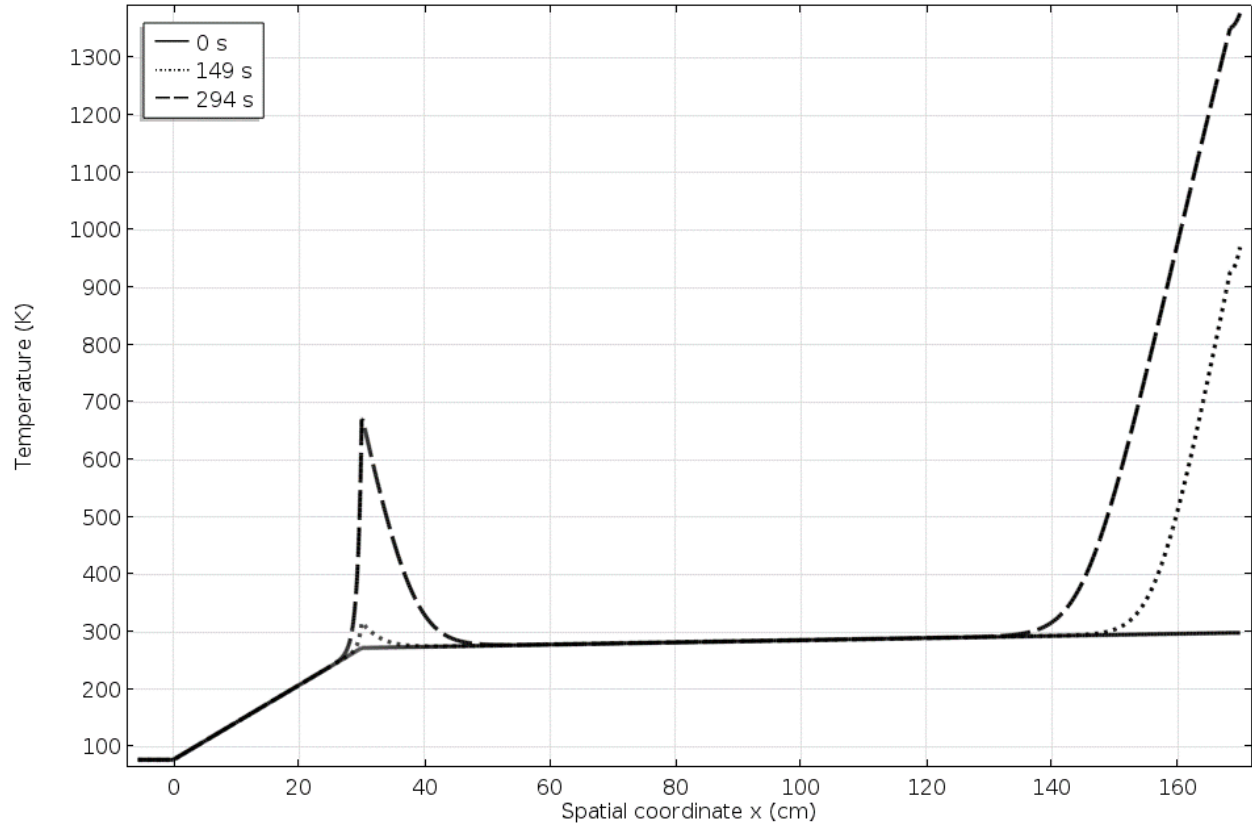


Figure 35: Sandia Model Step Two Temperature Profiles

Figure 35 illustrates typical temperature profiles through the second step of the model. This is the phase where the heating lamps are turned on but the regression has not yet started. The solid line is near the start time for the step, the dotted line is at a later time, and the dashed line is at an even later time. The effects of radiation between the steel weather cover and the aluminum scrim can be seen as the temperature spike grows with time at each boundary.

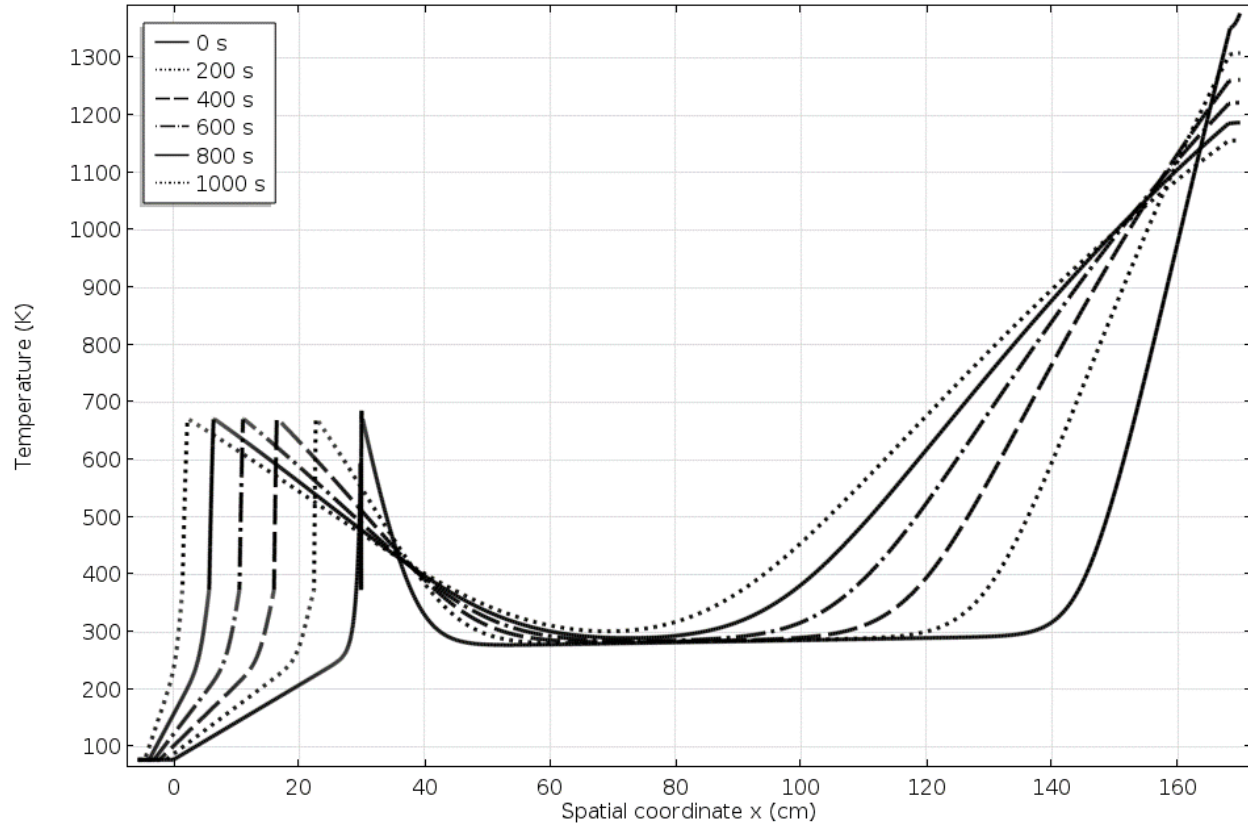


Figure 36: Sandia Model Step Three Temperature Profiles

Figure 36 illustrates typical temperature profiles through the third step of the model. This is the phase where regression is taking place. The solid line is near the beginning of the step, the dotted line is at a later time, the dash is at an even later time, and the dash dot line is at the final time. The left hand peaks represent the aluminum scrim and show the scrim and polystyrene regressing to the left.

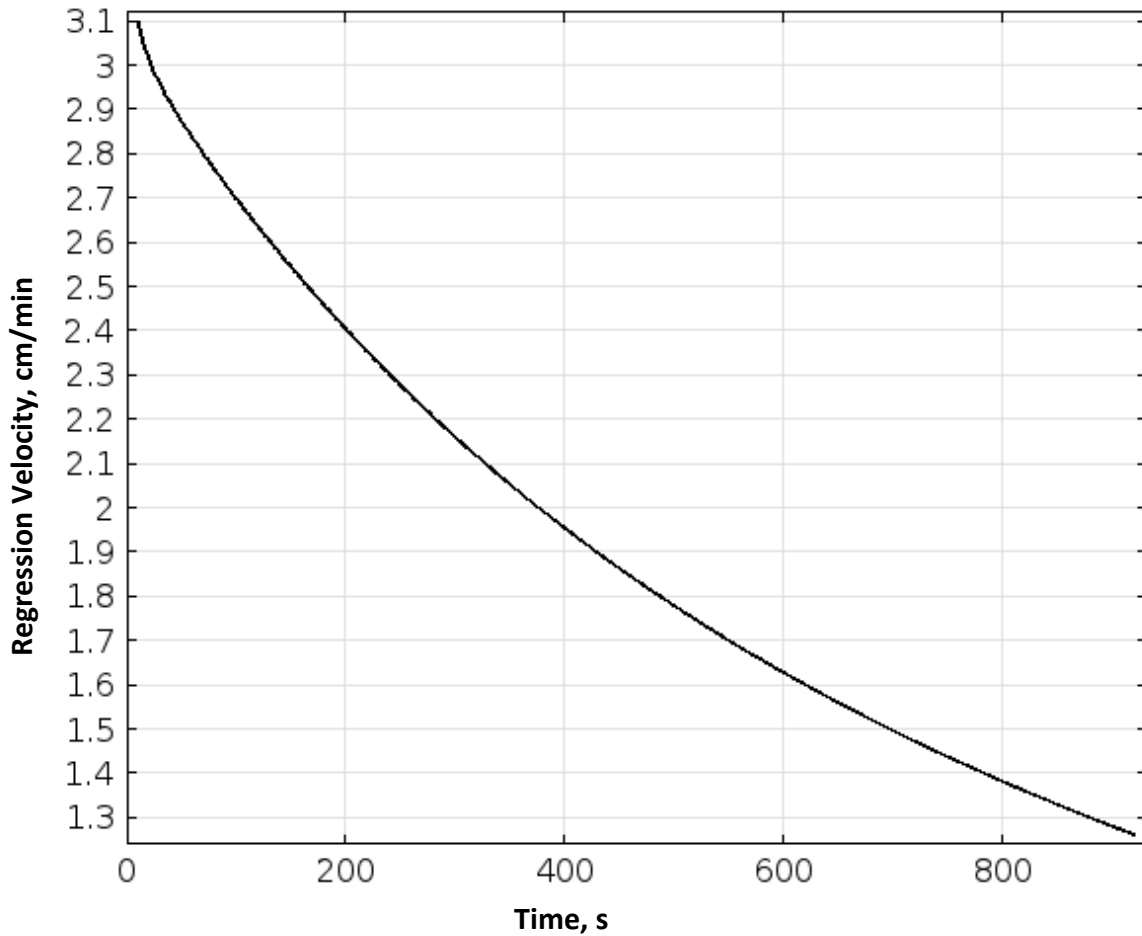


Figure 37: Sandia Model Regression Rate

Figure 37 shows a typical plot of regression rate versus time. In the Sandia model the regression rate is clearly changing with time. It starts high and decays exponentially. This is mostly due to the heat-out term in the regression equation. As the foam/ liquid interface gets closer to the LN2 temperature boundary condition, the heat-out term increases.

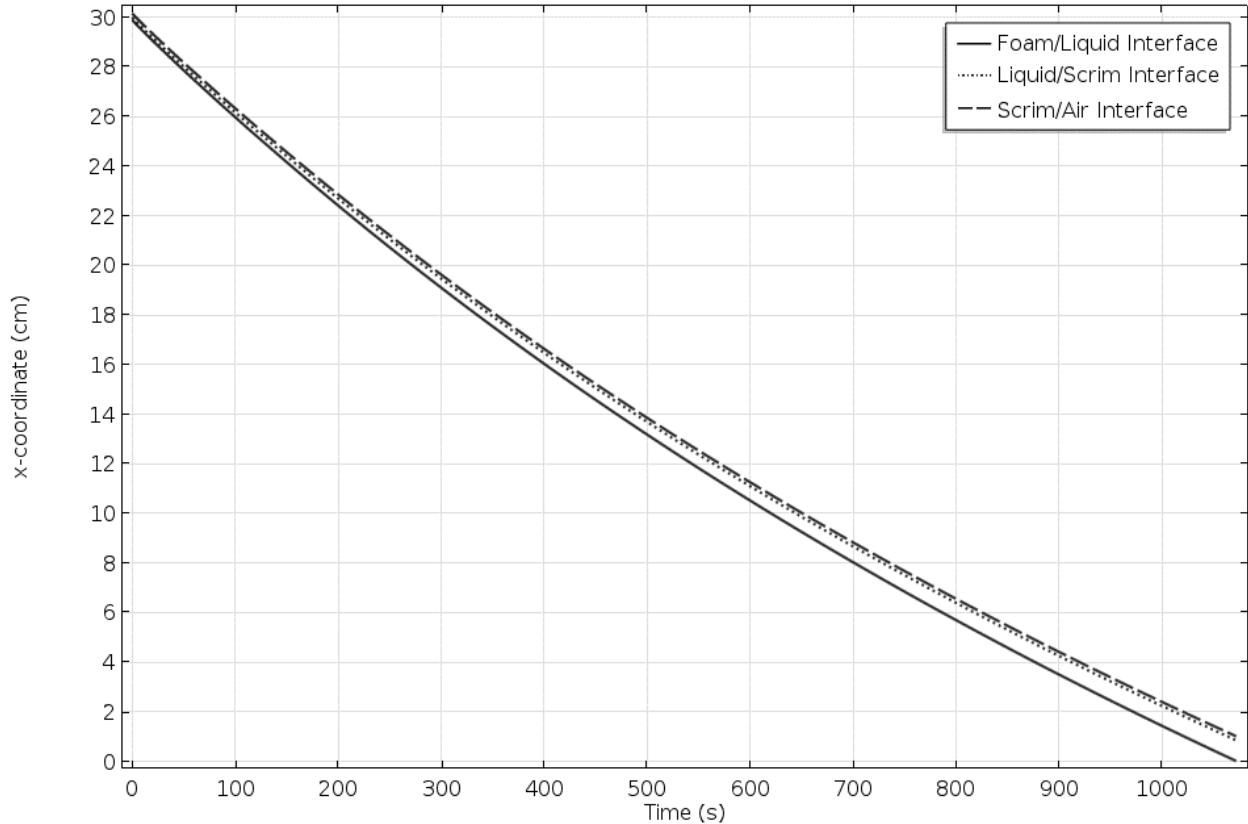


Figure 38: Sandia Model Boundary Movement

Figure 38 illustrates the typical boundary movement during step three. The bottom curve is the foam/ liquid interface boundary, the middle curve is the liquid/ aluminum scrim interface boundary, and the top curve is the aluminum scrim/ air interface boundary. The distance between the bottom and middle curves increases as the foam melts and the liquid layer grows. The distance between the middle and top curves remains the same as the aluminum scrim thickness remains constant.

Table 3 shows the complete results for emissivity investigation of the Sandia model. The model was run at three different aluminum scrim emissivities ranging from 0.02 to 0.2. The emissivities used reflect the lowest value commercially available, 0.02, to reasonable values for dirty working conditions on a LNG tanker, 0.1 and 0.2. At each emissivity, the model was run at two different foam thermal conductivities and two different maximum vaporization temperatures. Unlike in the other models where steady-state regression rate was the value of interest, the Sandia model result of interest is the total time for the foam to disappear. At all

three emissivities, the uncertainty in thermal conductivity and vaporization temperature causes only a few minutes of variance in total time required.

Table 3: Sandia Model Failure Time Results

emissivity	T_{vap}, K	k, W/m/K	t, min
0.1	640	0.034	22.75
0.1	640	0.021	23.43
0.1	670	0.034	22.37
0.1	670	0.021	22.78
0.2	640	0.034	19.62
0.2	640	0.021	20.11
0.2	670	0.034	19.14
0.2	670	0.021	19.38
0.02	640	0.034	52.42
0.02	640	0.021	51.96
0.02	670	0.034	52.77
0.02	670	0.021	51.83

The other value of interest in the Sandia model is the heat flux that leaves the system through the aluminum LN2 tank wall, left boundary of the system. This is a measure of how well the insulation is working during the simulated fire conditions. For an emissivity of 0.2 and 0.1 the heat flux into the LN2 is constant across steps two and three at 14.6 W/m² and 13.6 W/m² respectively. At an emissivity of 0.02, the heat flux is 8.6 W/m² through step two and the first part of step three. About half way through step three, the flux begins to slowly rise and reaches 8.8 W/m² by the end of the step.

As discussed in the model description, study step four was run with different sets of boundary conditions to explore several possible scenarios. A new aluminum scrim emissivity value of 0.8 was added to the range. This value simulates what would happen if the aluminum scrim fails or becomes soot covered when all the insulation is gone. The model was first run

with the ambient radiation boundary condition set to 298 K and with a tank wall condition set to 77 K. This simulates the heating lamps being turned off after the foam material has completely melted. Study step four was then run again with the ambient radiation boundary condition set to 1615.5 K. This simulates the heating lamps being left on after the foam material melts. The “lamp off” results are presented first with the “lamp on” results following.

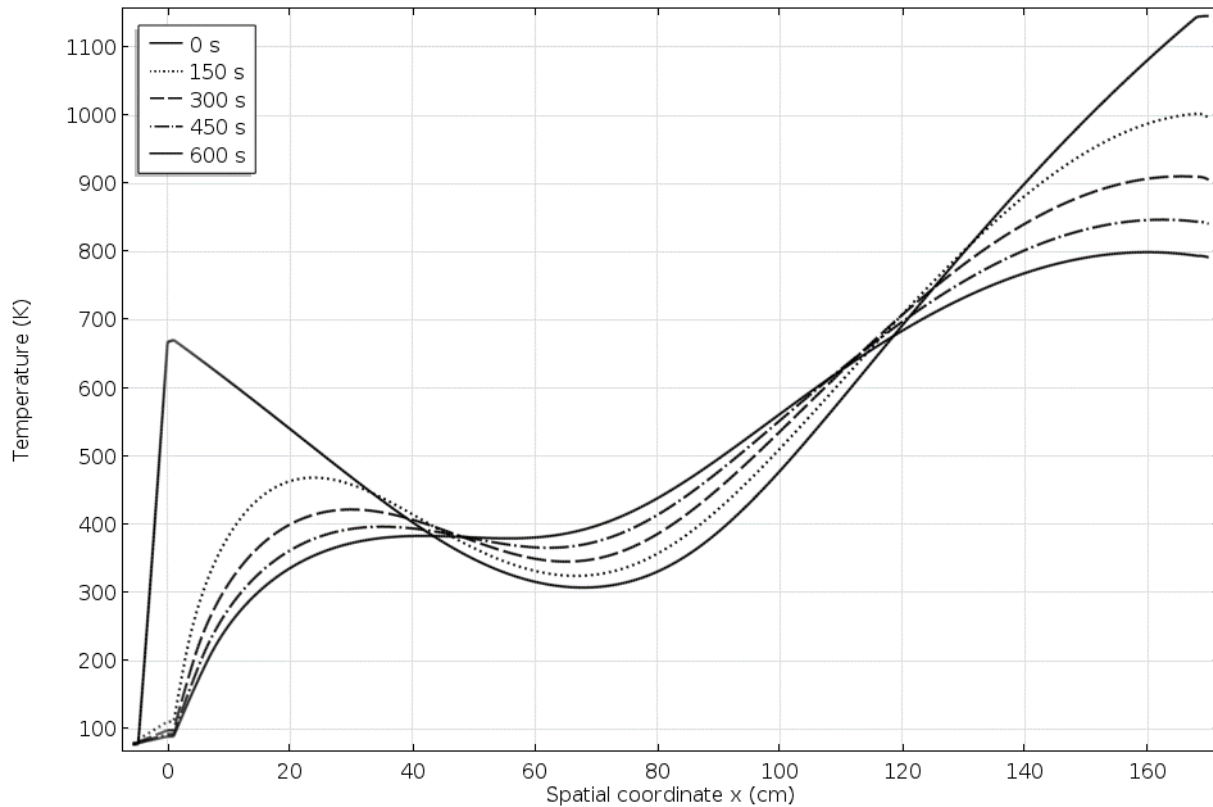


Figure 39: Sandia Model Step 4 Temperature Profiles with Heat Lamps Off

Figure 39 illustrates a typical temperature profile for study step four when the heat lamps are turned off. The solid line that forms the peak on left side is the temperature at the initial time. The dotted line is at a later time, the dashed line at an even later time, the dash-dot line later still, and the other solid line is at the final time of ten minutes. The profiles show the system approaching the initial steady-state profile of the model’s step one.

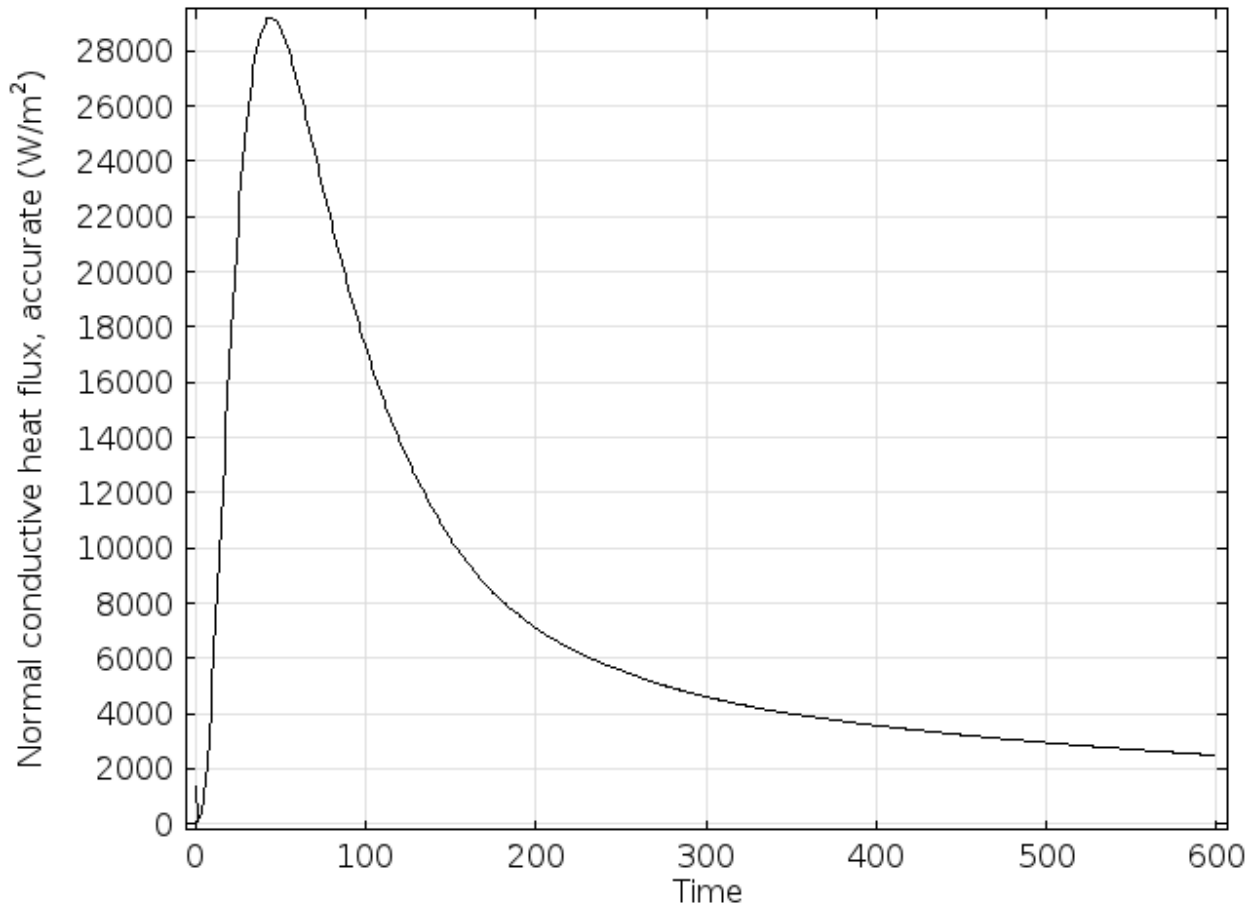


Figure 40: Sandia Model Step 4 LN2 Tank Heat Flux with Heat Lamps Off

Figure 40 illustrates the typical heat flux into the LN2 tank for step 4 when the heating lamps are turned off. The initial peak in flux corresponds to the polystyrene heat front reaching the LN2 tank. As the tank surface cools heat is transferred away from the tank decreasing the heat flux. The initial peak is similar for emissivity values of 0.02, 0.1, and 0.2 with a value around 30 kW/m². For an emissivity of 0.8, the initial peak in heat flux is about 46 kW/m². The final heat flux value varies with emissivity (Table 4). The initial heat flux peaks are well above the 7 kW/m² value reported by Sandia, but the 10 min values fall below that value except for with an emissivity of 0.8.

Table 4: Sandia Model LN2 Tank Flux Results

Emissivity	Tvap, K	k, W/m/K	Heat Lamp	Initial Flux Peak, W/m ²	Flux at 10 min, W/m ²
0.02	670	0.021	On	28000	7400
0.02	670	0.021	Off	27800	800
0.1	670	0.021	On	29600	31500
0.1	670	0.021	Off	28000	2500
0.2	670	0.021	On	30500	53800
0.2	670	0.021	Off	29500	3600
0.8	670	0.021	On	N/A	112000
0.8	670	0.021	Off	46000	9500

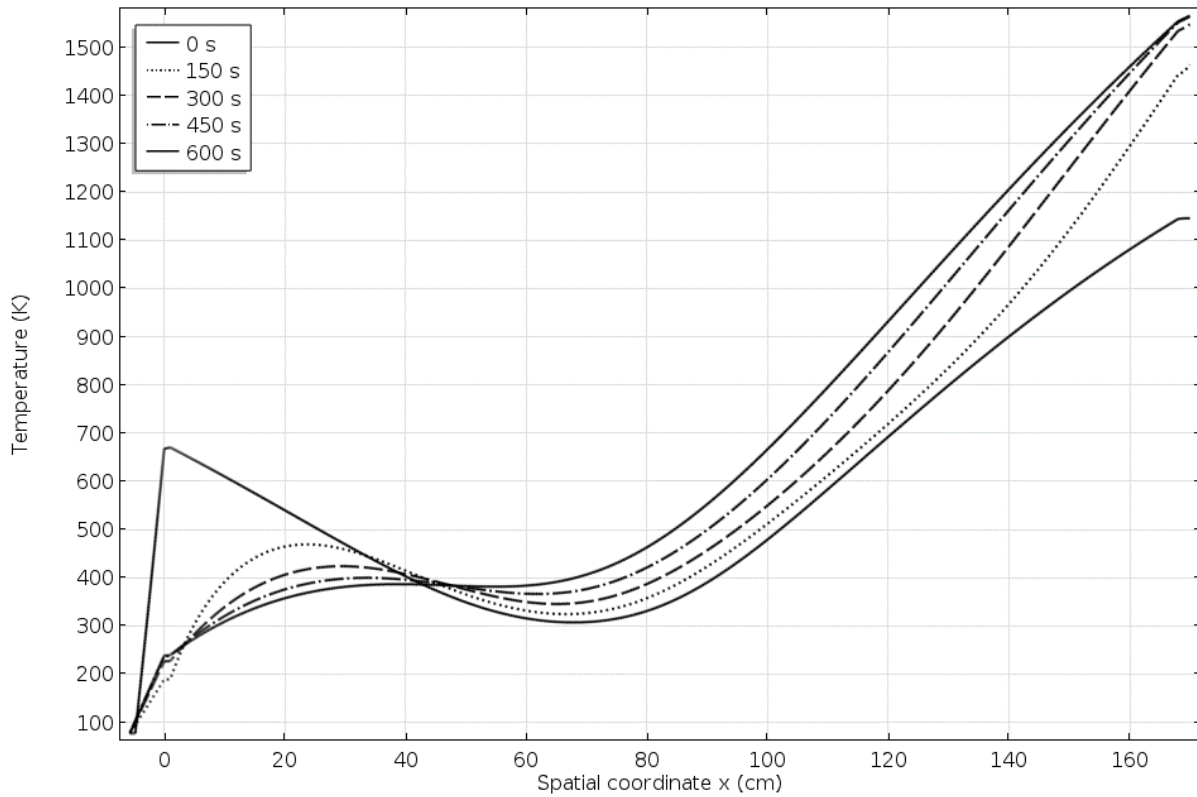


Figure 41: Sandia Model Step 4 Temperature Profiles with Heat Lamps On

Figure 41 illustrates typical temperature profiles for step four when the heat lamps remain on. The solid line that forms the peak on left side is the temperature at the initial time. The dotted line is at a later time, the dashed line at an even later time, the dash-dot line later still, and the other solid line is at the final time of ten minutes. Even with the heating lamps

turned on, the temperature of the LN2 tank surface decreases with time. The whole system approaches a new steady-state bounded by LN2 temperature on the left side and the heating lamp radiation on the right.

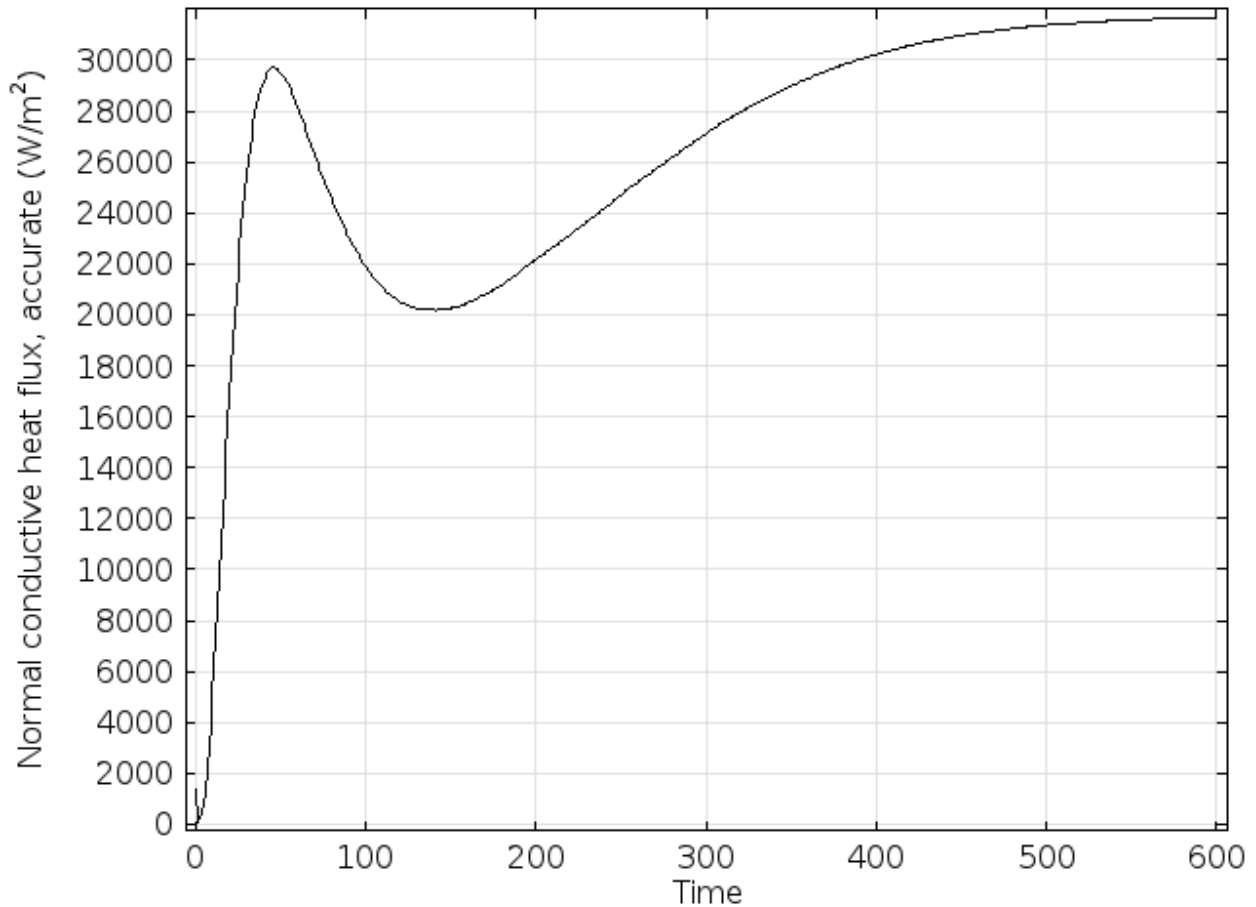


Figure 42: Sandia Model Step 4 LN2 Tank Heat Flux with Heat Lamps On

Figure 42 illustrates the typical heat flux into the LN2 tank for emissivity values of 0.2, 0.1, and 0.2 for study step 4 when the heating lamps are turned on. The initial peak in flux corresponds to the polystyrene heat front reaching the LN2 tank. As the tank surface cools heat is transferred away from the tank decreasing the heat flux. After the initial cooling slows down, the heat flux increases again and approaches a new steady-state. The initial peak is similar for emissivity values of 0.02, 0.1, and 0.2 around 30 kW/m². This initial peak matches with the initial flux peak from the “lamps off” runs.

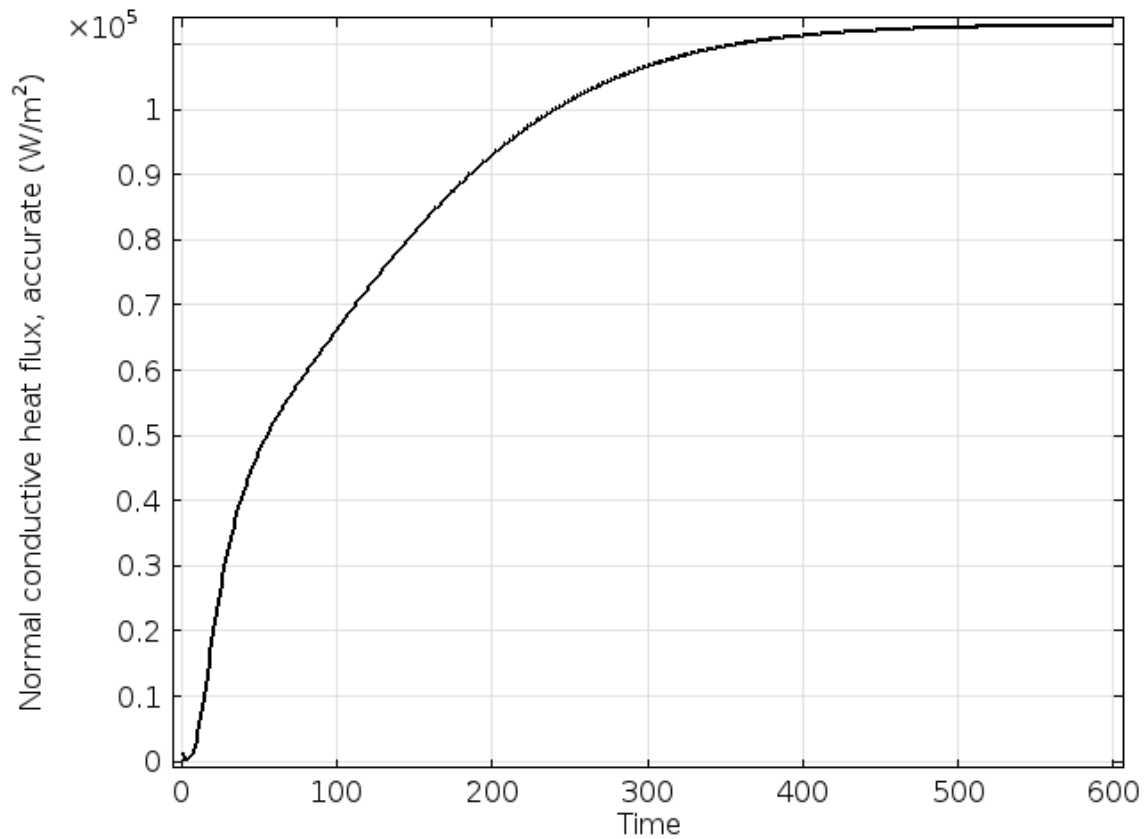


Figure 43: Sandia Model Step 4 LN2 Tank Heat Flux with Heat Lamps On and Foil Emissivity of 0.8

Figure 43 plots the study step 4 heat flux into the LN2 tank for an emissivity of 0.8. With this higher emissivity value there is no initial flux peak. Here, the radiation transfer heats the tank wall fast enough that there is no large cooling down period as observed with the other emissivities (Figure 44). The heat flux simply climbs up to its approach to steady-state value.

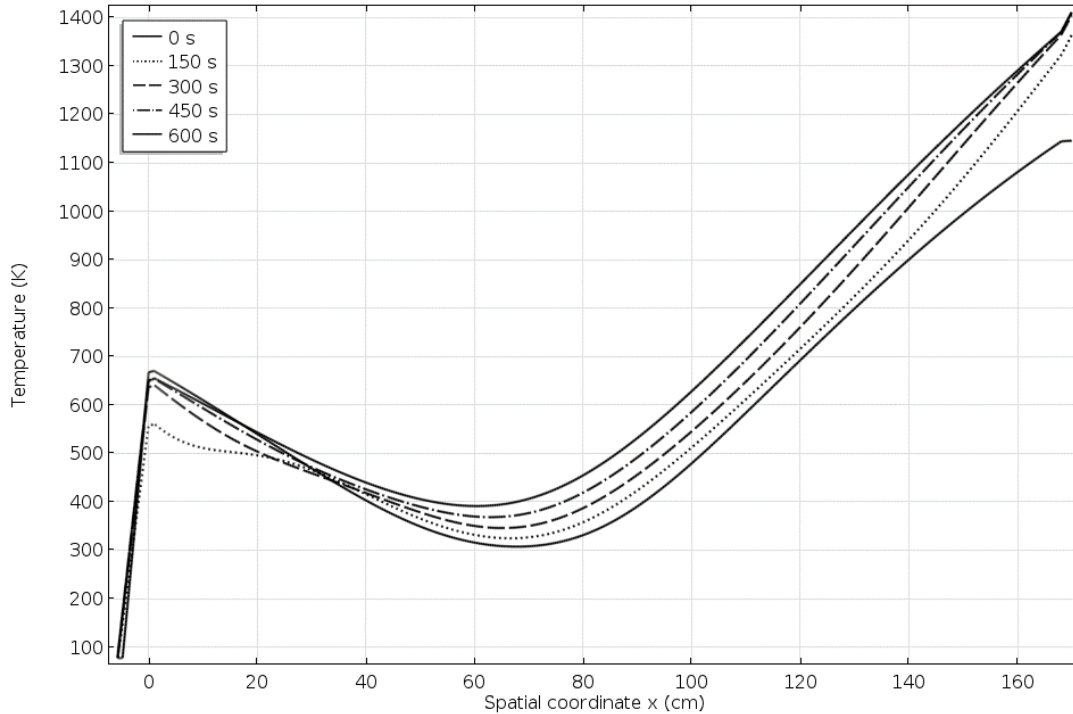


Figure 44: Sandia Model Step 4 Temperature Profiles with Heat Lamps On and Foil Emissivity of 0.8

In Figure 44, the solid line that forms the bottom of the right side is the temperature at the initial time. The dotted line is at a later time, the dashed line at an even later time, the dash-dot line later still, and the other solid line is at the final time of ten minutes. A small cool down is seen at the second time step (dotted line) before the LN2 tank wall heats back up.

The approach to steady-state heat flux value varies with emissivity (Table 4). The initial heat flux peaks for all emissivity values are well above the 7 kW/m^2 value reported by Sandia, as are the final values for emissivities of 0.1, 0.2, and 0.8. The final value for an emissivity of 0.02 falls about equal to Sandia's value.

Next, the film boiling boundary condition was tested instead of the fixed temperature value of 77 K at the tank wall. For this boundary condition, only emissivity values of 0.1 and 0.8 were evaluated.

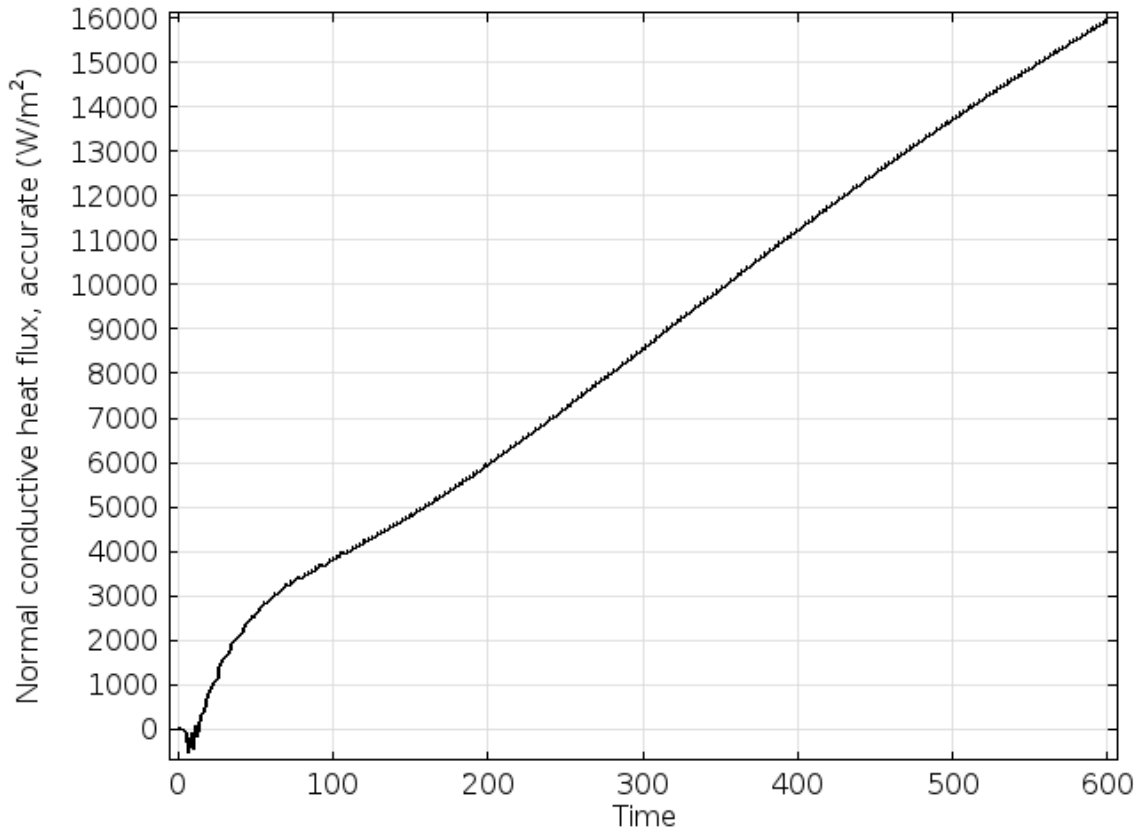


Figure 45: Sandia Model Step 4 LN2 Tank Heat Flux with Heat Lamps On and Film Boiling

Figure 45 illustrates the flux into the LN2 tank with the film boiling boundary condition and the heating lamps on. With the film boiling condition, there is no initial heat flux peak and the flux simply increases with time. The heat flux is also still steadily increasing after 10 min with no approach to a steady-state value. For an aluminum scrim emissivity of 0.1, the flux increases to about 16 kW/m² after ten minutes. At this emissivity, the flux remains below the Sandia value of 7 kW/m² for about 4 minutes. For an emissivity of 0.8, the flux increases to about 55 kW/m² (Table 5). At this emissivity, the flux remains below Sandia's value for only about 1.5 min.

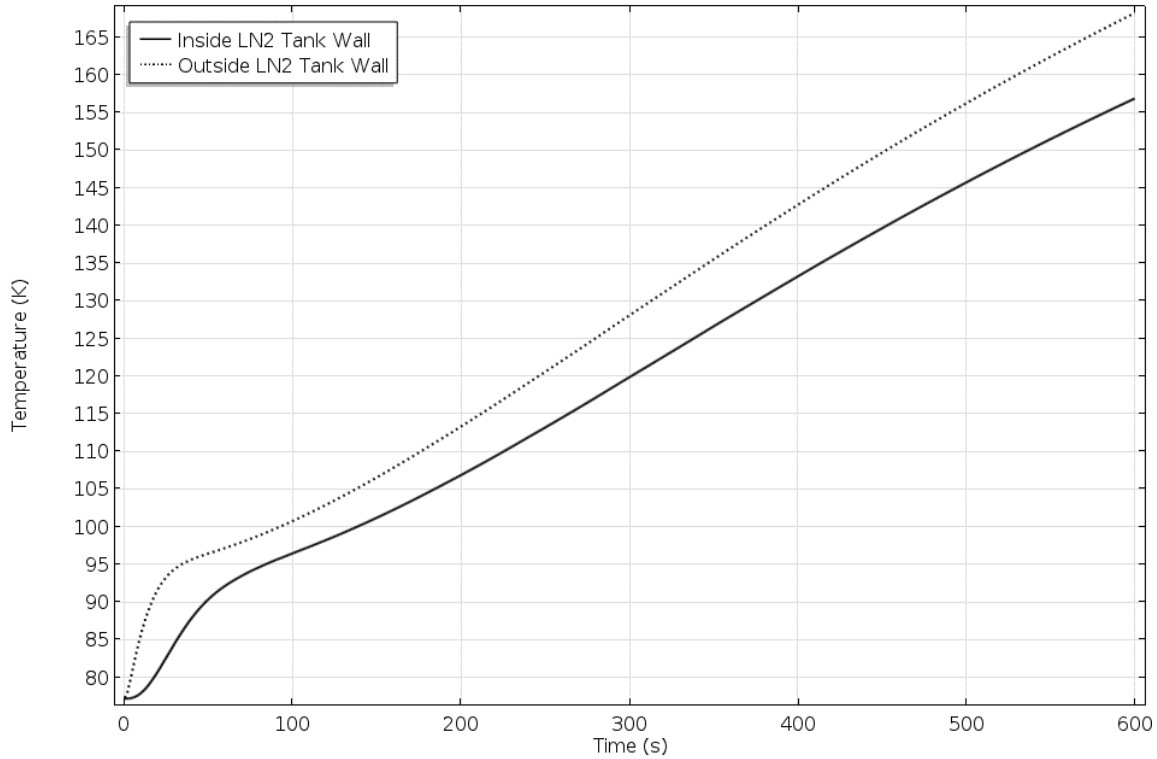


Figure 46: Sandia Model Step 4 LN2 Wall Temperature with Heat Lamps On and Film Boiling

Figure 46 illustrates the temperature of the tank wall through study step 4 with the film boiling condition and heat lamps on. Shown is the plot for an emissivity of 0.1. The dashed line is the temperature on the polystyrene or hot side of the tank. The solid line is the temperature on the LN2 or cold side of the tank. The plot for an emissivity of 0.8 looks very similar but with the temperatures rising to 390 K and 350 K at ten minutes. A problem often associated with film boiling is the overheating of heating elements or containment vessels. This model shows that overheating is not a potential issue for the Sandia experiments after ten minutes. The aluminum tank wall only heats to 390 K in the worst tested scenario, well below temperatures required to cause aluminum structural issues.

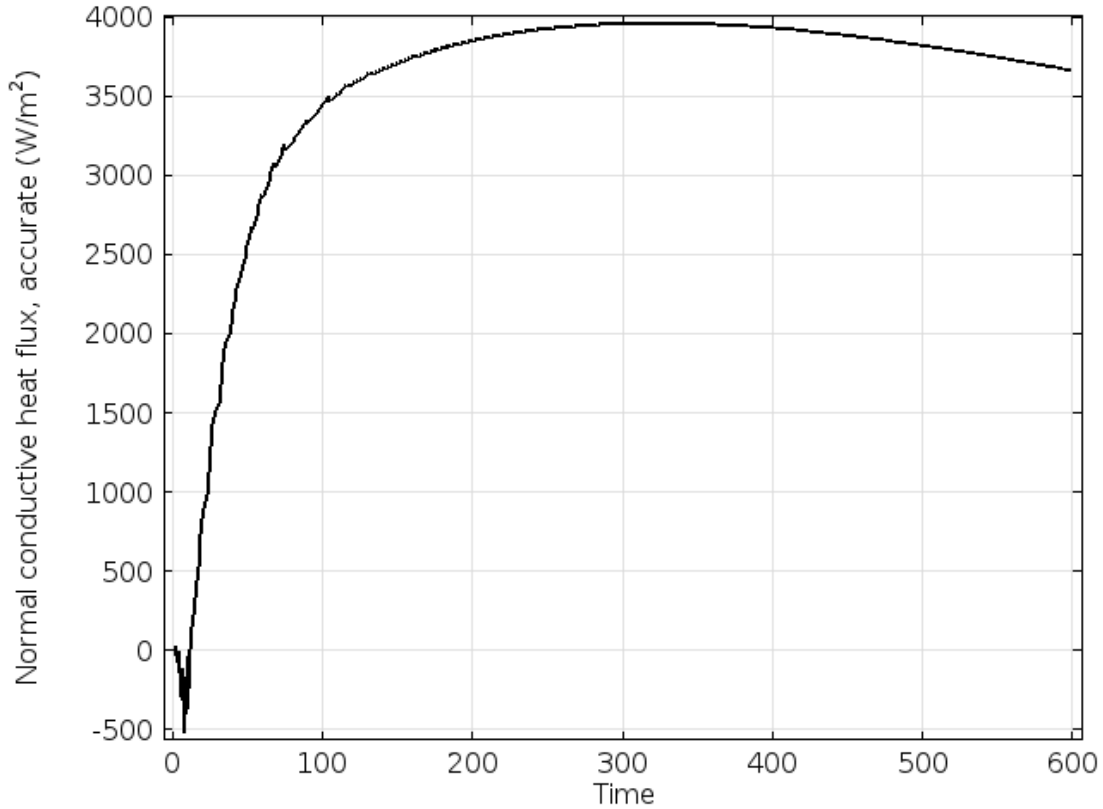


Figure 47: Sandia Model Step 4 LN2 Tank Heat Flux with Heat Lamps Off and Film Boiling

Figure 47 illustrates the typical study step 4 LN2 tank flux profile for film boiling when the heating lamps are turned off. Again, there is no initial peak in flux. Here the flux quickly rises to a broad peak that only decreases slightly within the ten minute run. Shown is the profile for an emissivity of 0.1. The profile for an emissivity of 0.8 looks very similar but rises to a peak of 11.6 kW/m² (Table 5).

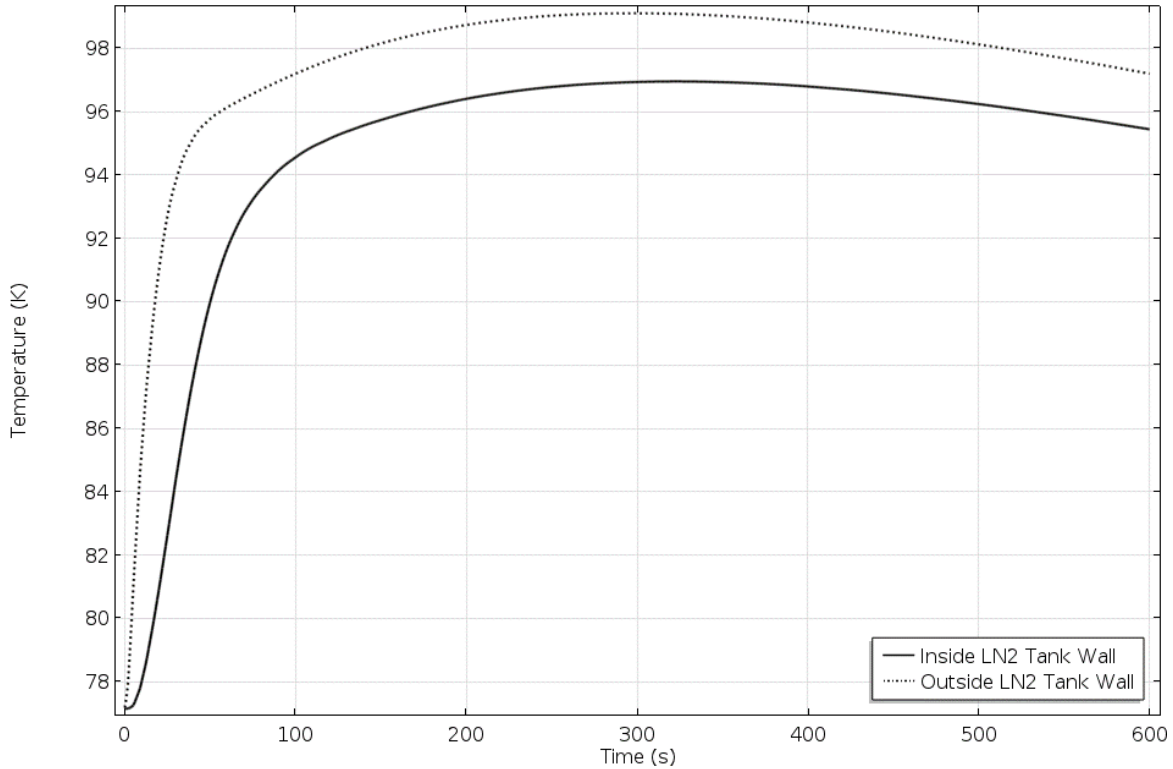


Figure 48: Sandia Model Step 4 LN2 Wall Temperature with Heat Lamps Off and Film Boiling

Figure 48 illustrates a typical LN2 wall temperature profile through study step 4 when the heating lamps are turned off. The dashed line is the temperature on the polystyrene or hot side of the tank. The solid line is the temperature on the LN2 or cold side of the tank. Similar to the flux profile, the temperature quickly rises to a maximum over a broad peak that only slightly decreases within the ten minute run time. Shown is the profile for an emissivity of 0.1. The profile for an emissivity of 0.8 is very similar but with maximum temperatures of 142 K and 135 K.

Table 5: Sandia Model LN2 Tank Flux Results with Film Boiling

Emissivity	Tvap, K	k, W/m/K	Heat Lamp	Initial Flux Peak, W/m ²	Flux at 10 min, W/m ²
0.1	670	0.021	On	N/A	16000
0.1	670	0.021	Off	4000	3600
0.8	670	0.021	On	N/A	55000
0.8	670	0.021	Off	11600	11400

Table 5 shows the complete flux results for the film boiling boundary condition model runs. Comparison to the results for emissivity values of 0.1 and 0.8 from Table 4 shows the effect of the film boiling boundary condition. The film boiling condition adds an extra resistance between the tank wall and the bunk fluid. The temperature boundary condition assumes an infinitely large thermal conductivity and potentially allows an infinite amount of heat flux. The film boiling condition limits the amount of heat flux with a convective heat transfer coefficient. For the transfer coefficient of $200 \text{ W/m}^2/\text{K}$ used, the film boiling condition roughly cuts the heat flux in half.

In the BCM and Butler models, care was taken to make sure that the ambient temperature condition applied at the bottom of the system did not affect the heat transfer at the top of the system. In the steady-state BCM model this was done by making the system an appropriate length. In the transient BCM model and the Butler model this was done by running the model for an appropriate amount of time. In the Sandia model this interaction between the vaporization temperature boundary condition and the downstream temperature boundary condition cannot be avoided. The model must run until all the foam material has melted, bringing the vaporization temperature into close proximity to the LN2 tank temperature boundary condition. It is possible that the LN2 tank temperature causes the vaporization temperature to fall as the two draw near. The degree to which this might occur is unknown, but if the liquid material is removed by vaporization it cannot fall below the minimum vaporization temperature of around 573 K. It is also possible that the vaporization temperature causes boiling on the inside of the tank wall increasing the tank wall temperature. There is no experimental data describing either effect. A decreasing vaporization temperature would affect the thermal front that reaches the LN2 tank wall after the foam has melted. It would decrease the initial tank heat flux spike. A film boiling boundary condition adds a layer of resistance, significantly reducing the amount of flux into the LN2. This is important as the heat flux is directly related to the amount of LN2 that would boil off. With no experimental data for guidance, the model assumes the vaporization temperature holds until all the material is melted. Without film boiling, this creates the largest possible thermal front and initial LN2 tank

heat flux. The film boiling boundary condition models the opposite side of possibilities, where the LN2 tank flux is near its minimum possible value.

Conclusions

The steady-state BCM model is a reasonable match with experimental data over the flux range of 56 to 63 kW/m². It appears to be unreasonable below this range and unknown applicability above this range. It should be somewhat reasonable above this range as the maximum vaporization temperature is achieved and the constant heat loss linear assumption from Tewarson should hold. The transient Butler model is a reasonable match over the range of 27 to 45 kW/m² incident flux. Its applicability is unknown outside these bounds. It should remain reasonable above and below this range as long as the constant heat loss linear assumption from Tewarson holds and the maximum vaporization temperature reached remains near the 640 to 670 K range explored.

The steps taken in creating the BCM and Butler models led to a model which reasonably approximates the Sandia National Labs large scale LNG insulation system testing. That model has shown the importance of the aluminum scrims surface emissivity on the insulation system failure times and the LN2 tank heat flux. Sandia reported an unusually long failure time for their experiment without providing any information on the scrim emissivity. Sandia also reported an unusually low value for heat flux into the LN2 after the insulation was completely ablated. The model created shows that the long failure time can only be explained by a very low emissivity, somewhere around the lowest possible commercially available. The low heat flux can be explained by a very low emissivity or by the added resistance of film boiling. This also implies that without film boiling the aluminum scrim must remain structurally intact and that nothing diminishes its emissivity during entire length of the experiment. With film boiling, the very lower emissivity must remain intact until at least the insulation fails. After insulation failure the emissivity can increase but not to unprotected levels of 0.8. Sandia offered that the generation of smoke inhibited heat transfer through the system, increasing failure time and decreasing tank flux. Modeling the effects of smoke were beyond the scope of this work and remains an area requiring more study.

Bibliography

- [1] Society of International Gas Tanker & Terminal Operators. *Report on the Effects of Fire on LNG Carrier Containment Systems*. Witherby Seamanship International Ltd, 2009
- [2] Havens, J.; Venart, J. **Fire performance of LNG carriers insulated with polystyrene foam**. *Journal of Hazardous Materials*, v 158, n 2-3, p 273-279, October 30, 2008
- [3] Reed, R.J. *North American Combustion Handbook: Combustion, Fuels, Stoichiometry, Heat Transfer, Fluid Flow*. North American Mfg. Co., 1986
- [4] Morgan, A.B.; Wilkie C.A. *Fire Retardancy of Polymeric Materials*, 2nd ed. CRC Press, Boca Raton, FL, USA, 2010
- [5] Bulter, J. **Degradation of Polystyrene Foam under Radiant Heat Flux**. M.S. thesis, University of Arkansas, Oct 2011
- [6] Mehta, S. (Worcester Polytechnic Inst, Worcester, United States); Biederman, S.; Shivkumar, S. **Thermal degradation of foamed polystyrene**. *Journal of Materials Science*, v 30, n 11, p 2944-2949, Jun 1 1995
- [7] Brauman, S.K.; Chen, I.J.; Matzinger, D.P. **POLYSTYRENE DEGRADATION DURING COMBUSTION**. *Journal of Polymer Science. Part A-1, Polymer chemistry*, v 21, n 6, p 1831-1845, Jun 1983
- [8] Tewarson, A. *Physico-chemical and Combustion/Pyrolysis Properties of Polymeric Materials*. Technical Report NBS-GCR-80-295, Factory Mutual Research, Nov 1980
- [9] Reddy, J.N.; Gartling, D.K. *The Finite Element Method in Heat Transfer and Fluid Dynamics*. 2nd edition, CRC Press, 2001, Ch 2, p 31-48
- [10] Donea, J.; Huerta, A.; Ponthot, J.; Rodriguez-Ferran, A. **Arbitrary Lagrangian-Eulerian Methods**. *Encyclopedia of Computational Mechanics*, Vol 1, Ch 14. John Wiley & Sons, 2004
- [11] Marti, E.; Kaisersberger, E.; Moukhina, E. **Heat Capacity Functions of Polystyrene in Glassy and Liquid Amorphous State and Glass Transition DSC and TMDSC Study**. *Journal of Thermal Analysis and Calorimetry*. v 85, n 2, p 505-525, 2006

- [12] Zang, X.; Hendro, W.; Fujii, M.; Tomimura, T.; Imaishi, N. **Measurements of the Thermal Conductivity and Thermal Diffusivity of Polymer Melts with the Short-Hot-Wire Method.** *International Journal of Thermophysics*. v 23, n 4, p 1077-1090, 2002
- [13] Shoulberg, R.H. **Thermal Diffusivity of Polymer Melts.** *Journal of Applied Polymer Science*. v 7, n 5, p 1597-1611, 1963
- [14] Vo, C.V.; Paquet, A.N. **An Evaluation of the Thermal Conductivity of Extruded Polystyrene Foam Blown with HFC-134a or HCFC-142b.** *Journal of Cellular Plastics*. v 40, n 3, p 205-228, 2004
- [15] Carin, M. **Numerical Simulation of Moving Boundary Problems with an ALE method. Validation in the Case of a Free or a Moving Solidification Front.** COMSOL Users Conference, Paris, 2006
- [16] Carslaw, H.S.; Jaeger, J.C. *Conduction of Heat in Solids*. Second Edition, Oxford University Press, 1959. Ch 11, p285-291
- [17] Tewarson, A. *Quantification of Fire Properties of Fuels and Interaction with Fire Environment*. Technical Report FMRC J. I. OEON6.RC, Factory Mutual Research, Apr 1982
- [18] Blanchat, T.; Morrow, C.; Hightower, M. *LNG Ship Insulation Experiments Using Large LNG Pool Fire Boundary Conditions*. Sandia National Laboratories Report, 2014
- [19] Flynn, T. M., Draper, J. W., and Roos, J. J., "Nucleate and Film Boiling Curve of Liquid Nitrogen at One Atmosphere" *Advan. Cryog. Eng.*, 7, p539-545